

**Optical Waves**  
**in Inhomogeneous Kerr Media**  
**Beyond Paraxial Approximation**

The research presented in this thesis was carried out at the group of Applied Analysis and Mathematical Physics, MESA+ Research Institute, University of Twente, PO Box 217, 7500 AE Enschede, The Netherlands.

This research was supported by the Technology Foundation STW (TWI. 4813), applied science division of NWO and technology programme of the Ministry of Economic Affairs, The Netherlands



**Twente University Press**

Publisher:  
Twente University Press,  
P.O. Box 217, 7500 AE Enschede, the Netherlands,  
[www.tup.utwente.nl](http://www.tup.utwente.nl)

Print: Océ Facility Services, Enschede

© A. Suryanto, Enschede, 2003  
No part of this work may be reproduced by print,  
photocopy or any other means without the permission  
in writing from the publisher.

ISBN 9036519535

OPTICAL WAVES  
IN INHOMOGENEOUS KERR MEDIA  
BEYOND PARAXIAL APPROXIMATION

PROEFSCHRIFT

ter verkrijging van  
de graad van doctor aan de Universiteit Twente,  
op gezag van de rector magnificus,  
prof. dr. F.A. van Vught,  
volgens besluit van het College voor Promoties  
in het openbaar te verdedigen  
op vrijdag 19 september 2003 te 15.00 uur

door

Agus Suryanto  
geboren op 7 augustus 1969  
te Malang, Indonesië

Dit proefschrift is goedgekeurd door de promotor  
prof. dr. E. van Groesen

en de assistent-promotor  
dr. H.J.W.M. Hoekstra

this thesis is dedicated  
to *my mother and the memory of my father*  
to *my wife and daughter*



# Abstract

This thesis deals with the propagation of optical waves in Kerr nonlinear media, with emphasis on optical beam propagation beyond the slowly varying envelope approximation (SVEA).

The first topic in this thesis is the propagation of a continuous-wave in one-dimensional (1D) nonlinear grating structures. For this purpose we develop a numerical scheme based on a variational method. It directly implements the nonlinear Helmholtz (NLH) equation and transparent-influx boundary conditions (TIBC) without introducing any approximation except the finite element discretization. This is different from nonlinear transfer matrix formalisms that are based on the SVEA and other approximations. Therefore our method can also be used to study the validity of the nonlinear transfer matrix methods. To illustrate our method, we study the optical response of linear and nonlinear quarter-wavelength reflectors and show that the method performs well, even for large nonlinear effects. The method is also found to be able to deal with the optical bistable behavior of ideal periodic structures or gratings with defect as a function of either the frequency or the intensity of the input light. We predict that a relatively low threshold of bistability can be achieved in a defect structure which has good optical features (in our case are large field enhancement and narrow resonance) by selecting the frequency of the incident light in vicinity of the defect mode frequency.

A numerical and analytical investigation of the deformation of bichromatic waves (or equivalently bi-plane waves in a spatial domain) is also presented. Within the paraxial approximation, it is shown that an optical pulse that is initially linearly bichromatic may deform substantially, resulting in large variations in amplitude and phase. Such deformations may lead to a train of soliton-like waves. The strong deformation of a bichromatic pulse is found to depend on exceeding a critical value of the quotient of amplitude and frequency difference. This behavior holds equally well for the spatial analog.

Using the SVEA, we derive a beam propagation model that includes a transverse linear refractive index variation. Based on this model we show that a stationary spatial soliton placed in a triangular waveguide will always oscillate inside the waveguide, and that the period of the oscillation depends on the soliton amplitude. Therefore, if a

bound- $N$ -soliton, which consists of  $N$  solitons of different amplitudes but with the same velocity, is excited in a triangular waveguide, it will break up into  $N$  individual solitons. After break up, solitons produced by the break up may exit from the waveguide or at least may have a perturbed oscillation path.

The abovementioned study on the bi-plane wave distortion and the propagation of spatial solitons is based on the SVEA. To study nonparaxial effects related to these phenomena, we derive a nonparaxial beam propagation model which is called the nonparaxial nonlinear Schrödinger equation. The accuracy of this model exceeds the standard SVEA. From several numerical experiments, we find that in cases where the degree of nonparaxiality is small, the paraxial equation is in good agreement with the nonparaxial model, as expected. However, in cases where rapid changes of the envelope occur, e.g. in the break up of a bound- $N$ -soliton or in the propagation of bi-plane waves where the product of the amplitude and the modulation period is relatively big, the paraxial model may not describe the correct physical phenomena for sufficiently large degrees of nonparaxiality.



# Acknowledgment

This thesis is the result of a four-years research project which is a part of Mathematical Optics research activities within the group of Applied Analysis and Mathematical Physics, University of Twente. Part of this project has also been done in the group of Integrated Optical MicroSystems. Here I would like to express my sincere thanks to those who have contributed in accomplishing this thesis.

First of all, I would like to thank my promotor *Brenny van Groesen* and assistant promotor *Hugo Hoekstra* who are also my supervisors, for the opportunity to work on this project as well as for their stimulating discussions, constructive comments, critical reviews and patience during the execution of this work. I would also like to acknowledge *Manfred Hammer*. He is formally not my supervisor, but he is always willing to discuss my problems and to give useful suggestions.

The fruitful discussion during the weekly "optics meeting" is appreciated. From this meeting, I have learned a lot about optics. In this regard, I would like to thank *Remco* (who also did the "Samenvatting" translation of this thesis), *Theo*, *Stefan*, *Frits*, *Sena*, *Henri*, *Kiran*, *Jaqueline* and *Debby*. I would also like to thank *Helena* to whom I went to discuss about general mathematical methods.

I wish to express my thanks to my office-mate *Monika* for the comfortable situation in TWRC B320; for sharing coffee, cookies and discussing about life in Holland. Unfortunately, we had to move from that building because of "fire 201102". I also enjoyed to be a member of AAMP group. The "morning coffee group" (it's a pity, it does not exist anymore) and lunch together with the member of MPCM group: *Marielle*, *Edi*, *Timco*, *Natanael*, *Vita*, *Mike*, *Hadi*, were really "gezellig".

I am very grateful to all member of Indonesian Student Association in Enschede; they have made my stay in Holland enjoyable.

Many thanks are due to my mother, sisters and brothers for everything. Finally, my special gratitude is directed to my lovely wife *Iis* for her patience, understanding and support; and also to my wonderful daughter *Alifia* for her cheerful smile. Furthermore, both of you have made my life to be more life.



# List of abbreviation

CB	Conduction Band
FDTD	Finite Difference Time Domain
FEM	Finite Element Method
F-P	Fabry-Perot
FWHM	Full Width at Half Maximum
IDRI	Intensity Dependet Refractive Index
MI	Modulational Instability
NDR	Nonlinear Dispersion Relation
NLH	Nonlinear Helmholtz
NLS	Nonlinear Schrödinger
NNLS	Nonparaxial Nonlinear Schrödinger
PBG	Photonic Band Gap
TBC	Transparent Boundary Condition
TE	Transverse Electric
THG	Third Harmonic Generation
TIBC	Transparent-Influx Boundary Condition
TM	Transverse Magnetic
SHG	Second Harmonic Generation
VB	Valence Band



# Contents

<b>Abstract</b>	<b>vii</b>
<b>Acknowledgment</b>	<b>ix</b>
<b>List of abbreviation</b>	<b>xi</b>
<b>1 Introduction</b>	<b>1</b>
1.1 Nonlinear optical phenomena . . . . .	2
1.1.1 Maxwell's equations and nonlinear polarization . . . . .	2
1.1.2 Optical bistability . . . . .	5
1.1.3 Modulation instability . . . . .	6
1.1.4 Optical solitons . . . . .	7
1.1.5 Remarks on Kerr nonlinear materials . . . . .	8
1.2 Thesis outline . . . . .	9
<b>2 Optical bistability in one-dimensional nonlinear photonic band gap structures</b>	<b>15</b>
2.1 Introduction . . . . .	15
2.2 Wave equation and its boundary conditions . . . . .	17
2.3 Numerical Method . . . . .	19
2.3.1 Linear scheme . . . . .	19
2.3.2 Nonlinear scheme . . . . .	22
2.3.3 Nonlinear solver . . . . .	23

2.4	Optical bistability in 1D PBG structure . . . . .	26
2.4.1	Transmission properties of perfect linear PBG structure . . . . .	27
2.4.2	Transmission properties of linear PBG structure with a defect . . . . .	28
2.4.3	Bistable switching by frequency tuning . . . . .	34
2.4.4	Bistability controlled by input intensity . . . . .	36
2.5	Concluding remarks . . . . .	39
<b>3</b>	<b>Deformation of modulated wave groups in Kerr media</b>	<b>43</b>
3.1	Introduction . . . . .	43
3.2	Governing equation . . . . .	44
3.2.1	Temporal-NLS equation for pulse propagation . . . . .	44
3.2.2	Spatial-NLS equation for beam propagation . . . . .	45
3.2.3	Phase-amplitude equation for NLS equation . . . . .	46
3.3	Numerical results . . . . .	47
3.4	Analytical description of the deformation . . . . .	51
3.4.1	Instability condition based on NDR . . . . .	51
3.4.2	Instability condition based on energy argument . . . . .	53
3.4.3	Deformation of the initial shape . . . . .	54
3.5	Low dimensional model . . . . .	55
3.5.1	Model formulation . . . . .	55
3.5.2	Dynamics of the model . . . . .	57
3.5.3	Envelope deformation . . . . .	58
3.6	Concluding remarks . . . . .	60
<b>4</b>	<b>Propagation of spatial solitons in inhomogeneous media with Kerr nonlinearity: Paraxial approximation</b>	<b>63</b>
4.1	Introduction . . . . .	63
4.2	Beam propagation in Kerr media . . . . .	64
4.2.1	NLS equation for uniform media . . . . .	64
4.2.2	Modified-NLS equation for non-uniform media . . . . .	66

	xv
4.3 Propagation of a soliton beam in inhomogeneous media . . . . .	67
4.3.1 Equivalent-particle approach . . . . .	67
4.3.2 A soliton beam in a triangular refractive index profile . . . . .	68
4.4 Break up of bound N-soliton into multiple independent solitons . . . . .	73
4.5 Concluding remarks . . . . .	77
<b>5 Weakly nonparaxial beam propagation in Kerr nonlinear media</b>	<b>81</b>
5.1 Introduction . . . . .	81
5.2 Nonparaxial correction to the NLS equation . . . . .	82
5.3 Power conservation law . . . . .	85
5.4 Soliton propagation in uniform media . . . . .	86
5.5 Soliton propagation in non-uniform media . . . . .	89
5.6 Propagation of bound-N-soliton . . . . .	91
5.7 Deformation of bi-plane wave . . . . .	95
5.8 Concluding remarks . . . . .	98
<b>6 Conclusions and recommendations</b>	<b>101</b>
<b>Samenvatting</b>	<b>105</b>
<b>Ringkasan</b>	<b>107</b>
<b>List of publications</b>	<b>109</b>
<b>Curriculum vitae</b>	<b>111</b>





# Chapter 1

## Introduction

The inventions of lasers in 1960s as a coherent light source [25] and of low loss optical fibers in 1970s [21] have driven the rapid development of optical telecommunication and information systems, see e.g [1] and references therein. The operation of devices occurring in these systems is based on both electronics and photonics. A communication network consists of nodes which are connected by a series of links. The links are used to transmit the information while the nodes are for routing the information, i.e. at nodes it is decided which path the information should follow from source to destination. Currently, many of the (long distance) links are mostly realized by optical fibers to carry information via light. While the links are optical, the nodes are still mostly electrical. In the past, this combination of optical and electronic technology has served the data-communication networks adequately. At present, this technology is predicted to breakdown as the demand for telecommunication services is increasing almost exponentially. Since very high capacity dispersion-free transmission communication over long distances can be realized, e.g. by implementing solitons and other types of nonlinear pulse transmission in optical fiber, it seems that the bottlenecks are the data processing and switching components in the nodes. Therefore, one aims to replace the nodes based on electrical technology by optical ones. As a follow up of the success of soliton pulse transmission, the study of optical phenomena in nonlinear waveguides (soliton-like beams, optical bistability, etc.) has been intensified, in the hope that these can be used for all-optical switching purposes. In order to design such devices, it is extremely important to understand the physical phenomena appearing in the structures. To predict the behavior of light in the structures analytical descriptions or at least numerical simulations are essential. In this thesis we develop a new numerical tool to study the light propagation in one-dimensional nonlinear grating structures. A model for the beam propagation in third-order nonlinear media will also be derived. This model will be used to study the behavior of light in the structures analytically and numerically.

In the following section, we will present a brief description of nonlinear optical phenomena in third-order media. The outline of this thesis will be presented in the last section of this chapter.

## 1.1 Nonlinear optical phenomena

In this section we give a short introduction to nonlinear optics. We will concentrate on the third-order nonlinearity, especially the refractive-index change induced by the light intensity. Some nonlinear optical phenomena resulting from the light-induced refractive index change that are relevant for this thesis will also be presented.

### 1.1.1 Maxwell's equations and nonlinear polarization

A theory of light propagation in dielectric media, involving a unified treatment of the electric field and the magnetic field, was developed for the first time by Maxwell in the 1860s. His equations in vector form are

$$\nabla \times \mathbf{E} = -\frac{\partial \mathbf{B}}{\partial t}; \quad (1.1)$$

$$\nabla \times \mathbf{H} = \mathbf{J} + \frac{\partial \mathbf{D}}{\partial t}; \quad (1.2)$$

$$\nabla \cdot \mathbf{D} = \rho; \quad (1.3)$$

$$\nabla \cdot \mathbf{B} = 0, \quad (1.4)$$

where the symbols  $\mathbf{E}$ ,  $\mathbf{D}$ ,  $\mathbf{H}$ ,  $\mathbf{B}$ ,  $\mathbf{J}$  and  $\rho$  denote the electric field, the dielectric displacement, the magnetic field, the magnetic induction, the free currents and the free charges in the material, respectively. In the following we only deal with non-magnetic materials without free charges and currents, i.e.

$$\rho = 0; \quad \mathbf{J} = 0; \quad (1.5)$$

$$\mathbf{D} = \varepsilon_0 \mathbf{E} + \mathbf{P}; \quad (1.6)$$

$$\mathbf{B} = \mu_0 \mathbf{H}, \quad (1.7)$$

where  $\mathbf{P}$  is the induced polarization vector in the medium,  $\varepsilon_0$  and  $\mu_0$  are the free-space permittivity and permeability, respectively. The origin of the polarization lies on the microscopic level. The positive and negative charges of molecules in a material shift under the influence of an external electric field  $\mathbf{E}$  and this creates a dipole moment in the molecule. This gives rise to an electric field in the opposite direction of  $\mathbf{E}$  inside the material which is characterized by the macroscopic quantity  $\mathbf{P}$ . The relation between  $\mathbf{P}$  and  $\mathbf{E}$  is written in the following expression

$$\mathbf{P} = \varepsilon_0 \left\{ \chi^{(1)} \cdot \mathbf{E} + \chi^{(2)} : \mathbf{E}^2 + \chi^{(3)} \vdots \mathbf{E}^3 + \dots \right\}. \quad (1.8)$$

Here  $\chi^{(i)}$  is the  $i^{\text{th}}$  order of the optical susceptibility (we have indicated that terms of higher-order than three will be neglected in this thesis). They are material coefficients and are tensors with rank  $(i + 1)$ . Here we assume that the nonlinear optical response is local and instantaneous to the applied electric field. A detailed discussion of the relation between  $\mathbf{P}$  and  $\mathbf{E}$  is beyond the scope of this thesis. A complete treatment of this subject including the description of the tensorlike nature of  $\chi^{(i)}$  can be found in standard textbooks of nonlinear optics, see e.g. [7], [8], [17], [20] and [28].

The second term in (1.8), i.e. the second order or quadratic nonlinear polarization, is responsible for the second harmonic generation (SHG) and other nonlinear wave mixing processes such as the sum- and difference-frequency generation, etc. The quadratic nonlinear polarization only appears in non-centrosymmetrical materials, see e.g. [20]. In this thesis we assume that the material is isotropic (which is also centrosymmetric) and therefore this quadratic polarization is not present.

The third term, i.e. the third-order or cubic nonlinear polarization, can lead to phenomena such as four-wave mixing, third-order harmonic generation (THG) and the intensity dependent refractive index (IDRI), etc. The third-order polarization in the frequency domain is written as

$$P_i^{(3)}(\omega) = \mathcal{D} \sum_{jkl} \chi_{ijkl}^{(3)}(-\omega; \omega_1, \omega_2, \omega_3) E_j(\omega_1) E_k(\omega_2) E_l(\omega_3), \quad (1.9)$$

where  $P_\alpha^{(3)}(\omega)$  and  $E_\alpha(\omega)$  are the components in  $\alpha$ -direction of the vectors  $\mathbf{P}^{(3)}(\omega)$  and  $\mathbf{E}(\omega)$ , respectively. The factor  $\mathcal{D}$  is the degeneration factor which identifies how many unique field combinations can be made for a given set of electric fields [7]. The indices  $'ijkl'$  refer to the Cartesian components of the fields and the tensor components of  $\chi^{(3)}$ . The polarization argument contains four frequencies which are related by

$$\omega = \omega_1 + \omega_2 + \omega_3 \quad (1.10)$$

where positive and negative frequencies denote the generating ( $\omega$ ) and generated ( $-\omega$ ) electrical or polarization fields. For example,  $\chi^{(3)}(-3\omega; \omega, \omega, \omega)$  describes the process of THG, i.e. three generating photons at energy  $\omega$  are absorbed and one photon at  $3\omega$  is generated. In this thesis, we mainly discuss the intensity dependent effects caused by the third-order nonlinear polarization at the frequency of the incident field, i.e. self-modulation. As we will see below, this process leads to a refractive index change which is proportional to the intensity of the input light. In this process, all frequencies are equal except their signs. The three unique combinations of these frequencies are  $\chi^{(3)}(-\omega; \omega, \omega, -\omega)$ ,  $\chi^{(3)}(-\omega; \omega, -\omega, \omega)$  and  $\chi^{(3)}(-\omega; -\omega, \omega, \omega)$  and therefore  $\mathcal{D} = 3$ . In this case, the dielectric displacement vector (1.6) for isotropic materials reduces to

$$\mathbf{D} = \varepsilon_0 \left( 1 + \chi^{(1)} + \chi^{(3)} |\mathbf{E}|^2 \right) \mathbf{E}, \quad (1.11)$$

where the constant  $\mathcal{D}$  has been scaled to unity, i.e.  $\mathcal{D}\chi^{(3)} \rightarrow \chi^{(3)}$ . Here, we can regard  $\chi^{(3)}$  as a scalar constant. The type of nonlinearity that appears in Equation

(1.11) is called a Kerr -nonlinearity and materials exhibiting such a nonlinearity are called Kerr or third-order nonlinear media. By using Equation (1.11) and Equations (1.5)-(1.6), and switching to the frequency domain (monochromatic light with frequency  $\omega$ ), the first two Maxwell's equations (1.1) and (1.2) reduce to

$$\nabla^2 \mathbf{E} + \frac{\omega^2}{c^2} \left( 1 + \chi^{(1)} + \chi^{(3)} |\mathbf{E}|^2 \right) \mathbf{E} = \nabla (\nabla \cdot \mathbf{E}), \quad (1.12)$$

where  $c = 1/\sqrt{\mu_0 \epsilon_0}$  is the speed of light in vacuum. In the derivation of Equation (1.12) we have assumed the possibility of interchanging the derivative with respect to time with the spatial derivatives for the magnetic field. Equation (1.12) is still very complicated to solve. In particular,  $\mathbf{E}$  is a complex vector and therefore we are faced with a set of three coupled equations of three complex variables. In this thesis we reduce the dimensionality of the problem to one- or two-dimensions by assuming that the dependency of the electric and the magnetic field on the neglected spatial coordinates can be ignored. In this case, the propagation of the electromagnetic field in a layered system can be simplified by considering two distinct types of solutions. The first type is the case where the magnetic field has a vanishing component in the propagation direction of the waveguide, i.e.  $H_z = 0$  (the magnetic field vector is perpendicular to the longitudinal axis  $z$ ). This is called a transverse magnetic polarized wave (TM). The second type is the case where the electric field vector is perpendicular to the propagation direction  $z$ . This second type is called a transverse electric polarized wave (TE). In this thesis we restrict ourselves to the discussion of the TE case. In one and two dimensions, the electric and the magnetic field vectors of TE waves respectively have the following forms

$$\mathbf{E} = [0, E(z), 0]; \quad \mathbf{H} = [H_x(z), 0, 0], \quad (1.13)$$

and

$$\mathbf{E} = [0, E(x, z), 0]; \quad \mathbf{H} = [H_x(x, z), 0, H_z(x, z)]. \quad (1.14)$$

Within this restriction, the right hand side of Equation (1.12) vanishes,  $\nabla \cdot \mathbf{E} = 0$  and therefore Equation (1.12) becomes

$$\nabla^2 E + \left( \frac{\omega}{c} \right)^2 \left( 1 + \chi^{(1)} + \chi^{(3)} |E|^2 \right) E = 0, \quad (1.15)$$

which is the nonlinear Helmholtz (NLH) equation. In the absence of  $\chi^{(3)}$ , the (linear) refractive index of the medium is given by  $n_0 = \sqrt{1 + \chi^{(1)}}$ . If Kerr nonlinearity is considered, the refractive index becomes intensity dependent. By assuming that the nonlinear contribution is small, the change of the refractive index is

$$\Delta n = n_2 |E|^2 \quad (1.16)$$

where  $n_2 = \chi^{(3)}/(2n_0)$  is called the nonlinear refractive index coefficient. Therefore, the generalized expression for the refractive index should be

$$n = n_0 + n_2 |E|^2. \quad (1.17)$$

A similar expression can be derived using the intensity  $I = \frac{1}{2}n_0\varepsilon_0c|E|^2$  :

$$n = n_0 + n_{2,I}I \quad (1.18)$$

where  $n_{2,I} = \chi^{(3)}/(n_0^2\varepsilon_0c)$ . The unit of  $\chi^{(3)}$  and  $n_{2,I}$  in **SI**-units are  $[\text{m}^2\text{V}^{-2}]$  and  $[\text{m}^2\text{W}^{-1}]$ , respectively. Notice that we have assumed that  $\chi^{(1)}$  and  $\chi^{(3)}$  are real constants; meaning that the considered materials are lossless. From now on, we also assume that  $\chi^{(3)}$  is positive.

It is well known that the IDRI is the fundamental process involved in several other major nonlinear optical effects, including self-focusing, modulation instability, optical bistability, etc. From the application point of view, the effect of IDRI can be applied to many novel devices such as all-optical switching and steering, data storage and processing, etc, see e.g. [20]. In the following we will briefly review some nonlinear optical phenomena that are relevant for the contents of this thesis.

### 1.1.2 Optical bistability

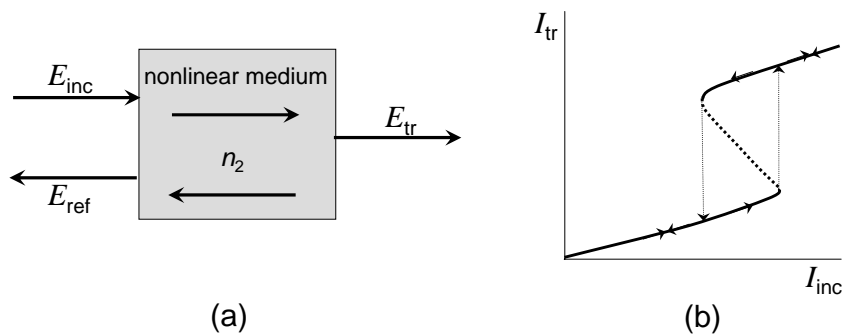


Figure 1.1: (a) Schematic illustration of a Fabry-Perot (F-P) interferometer containing a nonlinear medium. (b) Bistable response of a nonlinear F-P interferometer.

The study of optical bistability and bistable devices is a special branch of nonlinear optics. Optical bistability can be realized in many types of structures. However, in this thesis we will consider the phenomenon only in a type of Fabry-Perot (F-P) interferometers containing Kerr nonlinear media. The F-P like structure may be made from a single nonlinear medium or composed of nonlinear multi-layer structures. The typical structure of such a device is shown in Figure 1.1.(a). An optical field incident from the left ( $E_{inc}$ ) is splitted into a reflected and transmitted field by the front mirror. The partly transmitted field will be partly reflected and partly transmitted by the back mirror. The reflected field by the back mirror is redirected to the front mirror where a fraction is reflected again, and so on. The reflected electric field is denoted by  $E_{ref}$  while the transmitted electric field from the F-P is written as  $E_{tr}$ . If the F-P is linear, then the transmitted intensity ( $I_{tr}$ ) is uniquely determined by the input

intensity ( $I_{inc}$ ). However, in the F-P containing a Kerr medium, under the action of intense light, this device may exhibit a nonlinear response to the incident light in the sense that  $I_{tr}$  is a nonlinear function of  $I_{inc}$ . This includes the 'hysteresis loop', see Figure 1.1.(b), which corresponds to the optical bistability; as for a single input power corresponds to two stable states of the device. The appearance of such a state depends on the history of the system. Based on such a nonlinear response, this type of device can be used as an optical switch, optical limiter or an optical memory [16]. Since the bistability phenomenon is caused by the mechanism of the light-induced refractive index change in the medium, this phenomenon is called dispersive optical bistability. If the mechanism is caused by a light-intensity dependent absorption change then it is called absorptive optical bistability.

Experimental observations of (dispersive) optical bistability date back to the 1970s, see e.g. [6] and [15]. Since then, many theoretical studies have been directed to this phenomenon. The mathematical models used in those studies can be classified into two categories: the NLH equation and approximation models. The second type of model is used for example in a nonlinear transfer matrix formalism, see e.g. [13], [14], [27] and [31]. In these widely used formalisms, the electric field inside each layer is decomposed into two parts, the left- and the right propagating fields, by assuming that the envelope of the field varies slowly and the spatial third harmonics generated in the structure is negligible. In 1987, Chen and Mills studied the optical bistability in a single nonlinear medium [10] and nonlinear multi-layers [11] using the NLH equation. In their study, however, the NLH equation is transformed into coupled phase-amplitude equations where a general exact solution can be obtained. This solution cannot be expressed in terms of elementary functions but may be written in terms of Jacobi elliptic functions. Therefore it has to be evaluated numerically.

### 1.1.3 Modulation instability

The phenomenon of modulational instability (MI) is a process that may appear in most nonlinear wave systems. It appears when a monochromatic wave is perturbed with a low-intensity signal, and it causes the generation of sidebands around the spectral frequency of the wave. As a result, a quasi-continuous wave tends to disintegrate during propagation, see e.g. [1] and [19]; also Figure 1.2. The exponential growth of temporal frequency sidebands may lead to the spontaneous break up of the input field along the transverse coordinate into periodic arrays of solitonlike waves [18]. Therefore, in a rather loose context, MI can be considered to be a precursor of soliton formation. In nonlinear optics, MI may appear not only in time domain but also in spatial domain.

MI is modeled by the nonlinear Schrödinger (NLS) equation (see e.g. [1] and [19]):

$$i\frac{\partial A}{\partial \zeta} + \frac{1}{2}\frac{\partial^2 A}{\partial \xi^2} + |A|^2 A = 0, \quad (1.19)$$

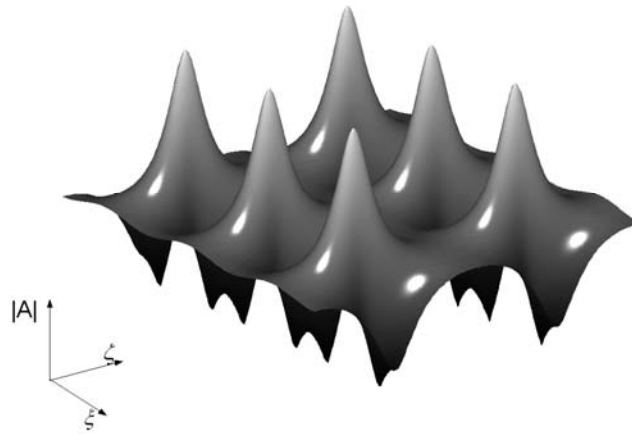


Figure 1.2: Simulation of modulation instability in a uniform Kerr medium using the NLS equation with initial condition  $A(\xi, \zeta = 0) = \frac{1}{2} + \frac{1}{50} \cos(\pi\xi/4)$ . During the propagation, the amplitude of a slightly perturbed monochromatic wave can increase significantly.

where  $A$  is the amplitude of the wave envelope,  $\zeta$  is the propagation direction and  $\xi$  is the transversal coordinate. The NLS equation which governs the pulse propagation through optical fibers and two-dimensional spatial beam propagation in Kerr media is based on the slowly varying envelope approximation (SVEA). Experimental verifications of MI of light waves in optical fibers have been performed e.g. by Tai et. al. [29] and [30]. MI is observed experimentally not only in pulse propagation but also in the spatial domain, see e.g. [9], [26] and [23].

#### 1.1.4 Optical solitons

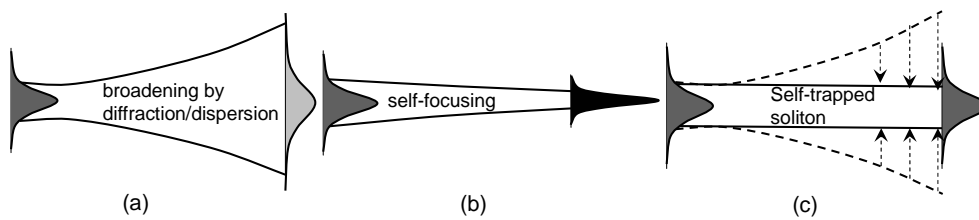


Figure 1.3: Schematic plots showing three cases of propagation of spatial beam (pulse) profile: (a) normal beam diffraction or pulse dispersion, (b) self-focusing beam (pulse) and (c) soliton.

Optical beams (pulses) propagating in a linear medium have a natural tendency to broaden in space (diffraction) and time (dispersion), see Figure 1.3.(a). In general, the narrower the initial beam (pulse) is, the faster it diverges (diffracts or disperse). In a Kerr nonlinear medium, the presence of light modifies its refractive index. The refractive index change resembles the intensity profile of the beams (pulses), forming an optical lens that increases the index in the center of beam (pulse) while leaving it unchanged in its tails. The induced lens focuses the beam (pulse) and therefore this phenomenon is called self-focusing (Figure 1.3.(b)). When the self-focusing exactly balances the diffraction (dispersion), the beam (pulse) propagates without changing its shape (Figure 1.3.(c)). The phenomenon of such self-trapping waves have been predicted and demonstrated not only in optics but also in other physical systems; e.g. surface waves in shallow water and plasmas. Such self-trapped waves are called solitary waves, but if they also have particle-like behavior then they are called solitons. Scientists and engineers are pragmatic, however, and they are happy to use the word 'soliton' to describe what appears to be an excitation that is humped, multi-humped, or localized long enough. In optics, if the light wave (soliton) is localized in time, e.g. an optical pulse in a fiber, then it is called a temporal soliton. On the other hand, if it is confined spatially, e.g. a self-trapped beam in a waveguide, then it is called a spatial soliton. In the following we will only consider spatial solitons.

Just as for MI, the first prediction of spatial solitons were also based on the NLS equation. The first spatial solitons in Kerr media were suggested in 1960s [12]. However, it became quickly clear that solitons in Kerr media are stable only in (1+1)D systems while in (2+1)D beams undergo catastrophic collapse [22]. The symbol (m+1)D means that the beams can diffract in m dimensions as they propagate in one dimension. The catastrophic collapse in (2+1)D shows the validity limit of the NLS equation. Later, it was shown that this unrealistic physical behavior does not appear when the nonparaxiality is included in the model: instead of collapse, the beam breaks up leading to beam filamentation. Thus, observation of spatial solitons in Kerr media requires a reduction of dimensionality, which can be achieved among other slab waveguides, and it was not until the mid-1980s that such solitons were observed for the first time [4]. In the positive Kerr medium, a (1+1)D NLS soliton is demonstrated theoretically and experimentally to be robust against perturbations in width and amplitude. So far, they have been observed in CS<sub>2</sub> [4], glass [2], semiconductor [3] and polymer waveguides [5].

### 1.1.5 Remarks on Kerr nonlinear materials

In the previous subsections we gave a brief description of some nonlinear optical phenomena caused by intensity induced refractive index changes. In order to realize those phenomena, a relatively high nonlinear response is required. Since the refractive index change is proportional to the product of  $\chi^{(3)}$  and the intensity, this can be done by using very high intensity light or a material that has a bigger coefficient



of nonlinearity. The existing materials today, however, generally have a very small nonlinearity ( $\chi^{(3)}$  is in the range of  $10^{-16}$  -  $10^{-20}$   $\text{m}^2\text{V}^{-2}$ ) requiring high intensity light in order to obtain considerable effects that can be applied. However, when the intensity is too high, it will severely damage the material. Hence, the fact that the available nonlinear materials have small values of  $\chi^{(3)}$  is seriously hampering the application of nonlinear optical concepts in practice. Recently, however, a large number of investigations have been directed to develop materials with larger coefficients, e.g. see [24]. At the current state of research, it is not known which order of magnitude will be attainable but one is optimistic that finally highly nonlinear materials will become available.

## 1.2 Thesis outline

This thesis deals with the topic of optical wave propagation in uniform or inhomogeneous Kerr media. The inhomogeneity will be introduced either only in the transversal coordinate or only in the propagation direction. In the latter case, we will only consider one-dimensional problem.

It is clear from the previous section that the propagation of light in Kerr media is modeled by the nonlinear wave equation (1.15). This equation governs the omnidirectional propagation. In most theoretical studies, this equation is approximated by introducing the SVEA (also known as the paraxial approximation). In this case, one writes the electric field as  $E(x, z) = A(x, z)\exp(ik_0z)$ . By assuming that the light mainly propagates with wave number  $k_0$  which also means that  $|2k_0\partial A/\partial z| \gg |\partial^2 A/\partial z^2| \ll |k_0^2 A|$ , one obtains a uni-directional wave equation. In this thesis we mainly study the effect of the nonparaxiality on the optical beam propagation in Kerr media. In chapter 2 we develop a direct numerical scheme to solve the one-dimensional NLH equation that will be used to study the optical bistability in one-dimensional nonlinear grating structures. In chapter 3 we perform analytical and numerical studies on the instability of modulated wave groups (bichromatic waves) based on the standard simplified model, i.e. the NLS equation. In chapter 4 we derive a mathematical model to describe analytically and numerically the swing effect of a spatial soliton and the break up of a bound-N-soliton in a nonlinear waveguide using the paraxial approximation. A model that includes the nonparaxial effect is derived in chapter 5. Below we give a more detailed summary of each chapter.

In chapter 2 we focus on the optical bistability in one-dimensional (1D) nonlinear multi-layer (periodic) structures. As mentioned previously, the widely used method to study this phenomenon, i.e. the nonlinear transfer matrix method (see e.g. Refs. [13] and [14]), is just an approximation of the NLH equation. Even though Chen and Mills ([10], [11]) derived the exact solution of the NLH equation, this solution in each nonlinear layer has to be written in Jacobi elliptic functions. Different from those methods, we will develop a finite element scheme to solve directly the exact 1D NLH

equation. As a requirement, we derive transparent-influx boundary conditions (TIBC) that properly incorporate the incident wave that are simultaneously transparent for all outgoing waves. Using our numerical scheme, we found that a defect layer in a linear periodic structure leads to a resonance frequency isolated inside the band gap of an ideal structure, known as a defect mode. This is in agreement with Ref. [32]. Then we further investigate the dependence of such defect modes on the thickness, the position and the refractive index of the defect layer as well as the number of layer periods in order to characterize structures with good optical features (large intensity enhancement and narrow resonance). We confirm that nonlinear multi-layer structures can exhibit bistable behavior as a function of either the frequency or the intensity of the input light. We find that a relatively low threshold of bistability can be obtained in an 'optimized' defect structure by selecting the frequency of the incident light in vicinity of a defect mode.

To deal with two-dimensional problems, we start in chapter 3 by studying the instability of modulated wave groups in a uniform nonlinear medium. This study is concerned with the bichromatic wave propagation. Our numerical simulations of the NLS equation show that the envelope of an optical pulse (or beam in spatial domain) that is initially linearly bichromatic can deform substantially, leading to large variations in both amplitude and phase. Furthermore, similar to the case of MI, the deformation may also lead to a train of soliton-like waves. To provide analytical explanations, we first transform the NLS equation into a set of coupled phase-amplitude equations. Using these equations or based on an energy argument, we find that the bichromatic wave deformation occurs when a characteristic parameter exceeds a lower bound. The characteristic parameter is the quotient of the wave amplitude and the frequency difference which is also proportional to the product of the wave amplitude and the modulation period. In the last part of chapter 3 we derive a low dimensional model to describe the distortion of bichromatic waves. We notice that the appearance of large amplitude variations may conflict with the SVEA used in this study.

In chapter 4 we concentrate on the propagation of (1+1)D spatial solitons under the influence of a transverse refractive index variation. First we derive a propagation model by introducing a small perturbation in the constant linear refractive index. By implementing a consistent multiple-scaled analysis and the SVEA, we obtain an inhomogeneous NLS equation. Based on this model we show analytically, using an equivalent-particle approach, and numerically, using the implicit Crank-Nicolson scheme, that a stationary soliton beam which is initially a little bit shifted from the center of a triangular waveguide will oscillate in the waveguide. The oscillation period is found to depend on the amplitude of the soliton. Based on these propagation properties, we find that if a bound- $N$ -soliton is placed in a triangular waveguide then it will break up into  $N$  independent solitons of different amplitudes. After the splitting process, a soliton either exits from the waveguide or remains trapped and oscillates in the waveguide. When at least two solitons oscillate inside the waveguide, they will collide with each other due to different oscillation periods. The effect of the collision

may be that a soliton exits from the waveguide or that at least the oscillation path is perturbed.

The study of the bichromatic wave deformation in a uniform medium (chapter 3) and the propagation of spatial solitons in an inhomogeneous medium (chapter 4) are based on the NLS equation. In fact, the NLS equation used in these studies is the leading order approximation to the NLH equation. In chapter 5, we extend the NLS equation by including higher-order terms to describe the effect of nonparaxiality. The result is still a one-way wave equation which means that all back-reflections are neglected. For brevity, we call that model the NNLS (nonparaxial NLS) equation. The accuracy of this approximation is beyond the standard SVEA. By investigating the conservation laws and the fundamental soliton solutions of the NLH equation, of the NLS equation and of the NNLS equation we confirm that the NLS and the NNLS equations are approximations of the NLH equation but that the NNLS model has a better accuracy. By performing several numerical simulations of the NNLS equation and comparing the results with the NLS calculations, we show that the NLS equation produces reasonably good predictions for relatively small degrees of nonparaxiality, as expected. However, in the regions where the envelope beam is changing rapidly, e.g. in the propagation of a bound-N-soliton in a nonlinear waveguide as well as in the propagation of two plane waves where the product of the amplitude and the modulation period is sufficiently large, the nonparaxiality plays an important role.

## References

- [1] Agrawal, G.P., *Nonlinear fiber optics*, (Academic Press, Inc., San Diego, CA, 3<sup>rd</sup> ed., 2001).
- [2] J.S. Aitchison, A.M. Weiner, Y. Silberberg, M.K. Oliver, J.L. Jackel, D.E. Leaird E.M. Vogel and P.W. Smith, Observation of spatial optical solitons in a nonlinear glass waveguide, *Opt. Lett.* **15**, p. 471, 1990.
- [3] J.S. Aitchison, K. Al-Hemyari, C.N. Ironside, R.S. Grant and W. Sibbett, Observation of spatial solitons in AlGaAs waveguides, *Electron. Lett.* **28**, p. 1879, 1992.
- [4] A. Barthelemy, S. Maneuf and C. Froehly, Propagation soliton et auto-confinement de faisceaux laser par non linearit optique de kerr, *Opt. Commun.* **55**, p. 201, 1985.
- [5] U. Bartuch, U. Peschel, Th. Gabler, R. Waldhaus and H.-H. Horhold, Experimental investigations and numerical simulations of spatial solitons in planar polymer waveguides, *Opt. Commun.* **134**, p. 49, 1997.
- [6] T. Bischofberger and Y. R. Shen, Theoretical and experimental study of the dynamic behavior of a nonlinear Fabry-Perot interferometer, *Phys. Rev.* **A19**, p.1169, 1979.

- [7] R.W. Boyd, *Nonlinear optics*, (Academic Press, Boston, 1992).
- [8] P.N. Butcher and D. Cotter, *The elements of nonlinear optics*, (Cambridge University Press, Cambridge, 1990)
- [9] C. Cambournac, H. Maillotte, E. Lantz, J.M. Dudley and M. Chauvet, Spatiotemporal behavior of periodic arrays of spatial solitons in a planar waveguide with relaxing Kerr nonlinearity, *J. Opt. Soc. Am.* **B19**, p. 574, 2002.
- [10] W. Chen and D.L. Mills, Optical response of a nonlinear dielectric film, *Phys. Rev.* **B35**, p. 524, 1987.
- [11] W. Chen and D.L. Mills, Optical response of nonlinear multilayer structures: Bilayers and superlattices, *Phys. Rev.* **B36**, p. 6269, 1987.
- [12] R.Y. Chiao, E. Garmire, and C.H. Townes, Self-trapping of optical beams, *Phys. Rev. Lett.* **13**, p. 479, 1964.
- [13] J. Danckaert, H. Thienpont, I. Veretennicoff, M. Haelterman, and P. Mandel, Self-consistent stationary description of a nonlinear Fabry-Perot, *Opt. Commun.* **71**, p. 317, 1989.
- [14] J. Danckaert, K. Fobelets, I. Veretennicoff, G. Vitrant and R. Reinisch, Dispersive optical bistability in stratified structures, *Phys. Rev.* **B44**, p. 8214, 1991.
- [15] H.M. Gibbs, S.L. McCall and T.N.C. Venkatesan, Differential Gain and Bistability Using a Sodium-Filled Fabry-Perot Interferometer, *Phys. Rev. Lett.* **36**, p.1135, 1976.
- [16] H.M. Gibbs, Optical bistability: *Controlling light with light*, (Academic Press, New York, 1985).
- [17] Y. Guo, C.K. Kao, E.H. Li and K.S. Chiang, *Nonlinear photonics: Nonlinearities in optics, optoelectronics and fiber communications*, (The Chinese University Press-Hongkong and Springer-Verlag Berlin, 2002).
- [18] A. Hasegawa, Generation of a train of soliton pulses by induced modulational instability in optical fibers, *Opt. Lett.* **9**, p.288, 1984.
- [19] A. Hasegawa and Y. Kodama, *Solitons in optical communications*, (Clarendon Press, Oxford, 1995).
- [20] G.S. He and S.H. Liu, *Physics of nonlinear optics*, (World Scientific, Singapore, 1999).
- [21] , F.P. Kapron, D.B. Keck and R.D. Maurer, Radiation losses in glass optical waveguide, *Appl. Phys. Lett.* **17**, p. 423, 1970.
- [22] P. L. Kelley, Self-focusing of optical beams, *Phys. Rev. Lett.* **15**, p. 1005, 1965.

- [23] D. Kip, M. Soljacic, M. Segev, E. Eugenieva and D.N. Christodoulides, Modulation instability and pattern formation in spatially incoherent light beams, *Science* **290**, p. 495, 2000.
- [24] H. Kishida, H. Matsuzaki, H. Okamoto, T. Manabe, M. Yamashita, Y. Taguchi and Y. Tokura, Gigantic optical nonlinearity in one-dimensional Mott-Hubbard insulators, *Nature* **405**, p. 929, 2000.
- [25] T.H. Maiman, Stimulated Optical Radiation in Ruby, *Nature* **187**, p. 493, 1960.
- [26] R. Malendevich, L. Jankovic, G.I. Stegeman and Aitchison JS, Spatial modulation instability in a Kerr slab waveguide, *Opt. Lett.* **26**, p. 1879, 2001.
- [27] J.H. Marburger and F.S. Felber, Theory of a lossless nonlinear Fabry-Perot interferometer, *Phys. Rev.* **A17**, p. 335, 1978.
- [28] A.C. Newell and J.V. Moloney, *Nonlinear optics*, (Addison-Wesley Publishing Company, California, 1992)
- [29] K. Tai, A. Hasegawa, and A. Tomita, Observation of modulational instability in optical fibers, *Phys. Rev. Lett.* **56**, p. 1358, 1986.
- [30] K. Tai, A. Tomita, J. L. Jewell, and A. Hasegawa, Generation of subpicosecond solitonlike optical pulses at 0.3 THz repetition rate by induced modulational instability, *Appl. Phys. Lett.* **49**, p. 236, 1986.
- [31] H.G. Winful, J.H. Marburger and E. Garmire, Theory of bistability in nonlinear distributed feedback structures, *Appl. Phys. Lett.* **35**, p. 379, 1979.
- [32] E. Yablonovitch, T.J. Gmitter, R.D. Meade, A.M. Rappe, K.D. Brommer and J.D. Joannopoulos, Donor and acceptor modes in photonic band-structure, *Phys. Rev. Lett.* **67**, p. 3380, 1991.



## Chapter 2

# Optical bistability in one-dimensional nonlinear photonic band gap structures

### 2.1 Introduction

The propagation of waves through periodic dielectric structures, called photonic band gap structures (PBG), has been extensively studied in recent years (see e.g. Ref. [11], [17] and [18]). An essential property of these structures is the existence of a frequency band gap in which light propagation is forbidden. This is analogous to the electronic band gaps in semiconductor crystals. In such a crystal, a moving electron experiences a periodic potential produced by the atomic lattice, which produces a gap in the electronic energy band. This gap splits the energy band into two parts: the lower energy band is called the valence band and the high energy band is the conduction band. The optical analogy is the photonic crystal where the periodic potential is due to a lattice of different macroscopic dielectric media. However, when a defect layer is introduced into an otherwise strictly periodic PBG structure, it can create donor or acceptor modes in the band gap [26]. Similar to the case of an electron being localized around a defect crystal, there is a large field enhancement in the optical defect structure.

When Kerr nonlinearity is introduced in the PBG structures (the effective refractive index now depends on the field intensity) it will alter the transmission spectrum including the position of the band-edges. This dynamic shifting of the band-edges can produce optical bistability phenomena; see e.g. Ref. [16], [20] and [23]. In Ref. [20] the author introduced an optical switch in a nonlinear finite grating using two light

pulses at different frequencies, a probe beam near the band-edge and a strong pump beam in the middle of the band gap to alter the index of refraction of the structure. The pump beam is used to control the position of the band-edge of the structure so as to transmit or reflect the probe beam. A drawback of this procedure was that the pump beam did not penetrate far into the structure and therefore did not change the effective index of refraction significantly. To increase the field penetration but prevent the transmission, Tran has introduced a defect layer in the grating structure and has shown that the defect structure can indeed improve the performance of these switching devices, see Ref. [21]. Since the switching mechanism consists of two pulses at difference frequencies, Tran [20] and [21] used the nonlinear finite difference time domain (NFDTD) method to go beyond the slowly varying envelope approximation and to avoid the complexity of the problem due to the interaction between two frequencies.

A different approach for an all-optical switch is based on the self-switching arrangement where the output depends nonlinearly on some characteristics of the input light, e.g. power. An example is optical bistability which can be realized among others in a nonlinear periodic structure. In this case the input light may be monochromatic. While the threshold value of bistability needed by a periodic structure is relatively high, He and Cada [9] proposed a combined structure which is composed of a distributed feedback structure and a phase-matching layer placed in a Fabry-Perot cavity in order to reduce the threshold significantly. Recently, Lidorikis *et al.* [12]) and Wang *et al.* [23] found that when a single nonlinear defect layer is introduced into a linear periodic structure, the threshold value of the bistability is compatible with that of the structure proposed by He and Cada [9]. Throughout this chapter we study a bistability that uses a monochromatic light input in finite periodic structures without and with a defect. For the defect structure, the nonlinearity will not only be introduced in the defect layer but also in the higher and/or lower index layers. Because we deal with a single frequency, the Maxwell's equations are reduced to a nonlinear Helmholtz (NLH) equation. Furthermore, the numerical calculations in the frequency domain are generally more efficient than those in time domain.

Since 30 years ago, a lot of efforts have been devoted to study the phenomenon of bistability in a periodic structure. A number of authors, e.g. Marburger and Felber [15], Winful *et al.* [25], Danckaert *et al.* [6] and [7] proposed an analytical formalism for this problem. All these formalisms are derived within three basic approximations, i.e. the slowly varying envelope approximation (SVEA), the approximation of nonlinear terms that appear in the interface conditions, and the omission of spatial third harmonics generated in the structure. Treatments that make use of the full nonlinear interface conditions in the nonlinear transfer matrix were given by Agarwal and Dutta Gupta [1] and Dutta Gupta and Agarwal [8].

Another approach to solve the nonlinear wave equation was proposed by Chen and Mills [4] and [5]. In this approach the NLH equation is transformed into a phase-amplitude equation. By combining with energy conservation the phase-amplitude



equation is written in integral form. The integral equation together with the continuity conditions at the interfaces are solved numerically. Recently this method has been implemented by Lidorikis *et al.* [12] to investigate the localized mode solution for a single nonlinear layer sandwiched between two linear periodic structures.

A semi-analytic method has been proposed by Wang *et al.* [23] to study the optical bistability in a linear structure with a single nonlinear defect layer in the center. The transfer matrix method is used for the linear part and a finite difference method is implemented for the nonlinear layer. The left and right linear parts and the nonlinear layer are linked using appropriate interface conditions.

In this chapter we discuss a finite element method (FEM) to study the nonlinear optical response of one-dimensional (1D) finite grating structures. We will directly implement the exact NLH equation and transparent-influx boundary conditions (TIBC) which will be derived in section 2.2. In section 2.3 the NLH equation together with TIBC is transformed into a variational numerical scheme. For the linear scheme we improve the standard FEM to get a fourth order accurate scheme that maintains the symmetric-tridiagonal structure of the finite element matrix. For the full nonlinear equation, we implement the improved FE scheme for the linear part and a standard FEM for the nonlinear part. The resulting nonlinear system of equations will be solved using two different input parameters, i.e. either the amplitude of the incident wave or that of the transmitted wave. In the subsequent sections we apply our numerical scheme to study the optical response of both linear and nonlinear grating structures. Finally we end this chapter with conclusions and remarks.

## 2.2 Wave equation and its boundary conditions

We consider the propagation of optical electromagnetic field through one-dimensional, periodic, dispersionless and lossless stratified dielectric media with a Kerr nonlinearity. The electric and the magnetic fields have the form,

$$\mathbf{E}(z, t) = [0, E_y(z, t), 0], \quad (2.1)$$

$$\mathbf{H}(z, t) = [H_x(z, t), 0, 0]. \quad (2.2)$$

Assuming that the media are isotropic, the polarization  $\mathbf{P}$  is parallel to  $\mathbf{E}$ :

$$\mathbf{P}(z, t) = [0, P_y(z, t), 0]. \quad (2.3)$$

Maxwell's equations then reduce to the wave equation

$$\frac{\partial^2 E_y(z, t)}{\partial z^2} - \frac{1}{c^2} \frac{\partial^2 E_y(z, t)}{\partial t^2} = \mu_0 \frac{\partial^2 P_y(z, t)}{\partial t^2}. \quad (2.4)$$

For a material with a Kerr nonlinearity, the polarization  $P_y$  is given by (see He and Liu [10])

$$P_y(z, t) = \varepsilon_0 \left\{ \chi^{(1)}(z) E_y(z, t) + \chi^{(3)}(z) |E_y(z, t)|^2 E_y(z, t) \right\}, \quad (2.5)$$

where  $1 + \chi^{(1)}(z) \equiv \epsilon_r(z) \equiv n^2(z)$  describes the linear dielectric constant,  $n$  is the refractive index and  $\chi^{(3)}$  is the third-order nonlinear susceptibility. If excited by an input beam with a single frequency  $\omega$ , the polarization (2.5) does not lead to the generation of high order harmonics in the Kerr medium. Hence we can look for stationary solutions of the form

$$E_y(z, t) = \exp(i\omega t) E(z). \quad (2.6)$$

The harmonic time dependence leads to the scalar NLH equation

$$\frac{d^2 E(z)}{dz^2} + k^2 \left( n^2(z) + \chi^{(3)}(z) |E(z)|^2 \right) E(z) = 0, \quad (2.7)$$

where  $k^2 = \omega^2/c^2$  with  $c = 1/\sqrt{\epsilon_0\mu_0}$  is the speed of light. Notice that equation (2.7) holds for arbitrary  $n(z)$  and  $\chi^{(3)}(z)$ . In many applications, we deal with the NLH (2.7) in the presence of an incident wave from either a linear or nonlinear homogeneous medium to a scattering structure (e.g. the linear or nonlinear periodic structure) that is followed by a linear or nonlinear homogeneous region. Here we assume that the medium outside the scattering structure is linear and homogeneous with refractive index  $n_0$ . In order to solve this problem numerically, we have to limit the original unbounded domain to a finite computational domain. In doing so, we have to provide boundary conditions that can transmit completely the incident wave and simultaneously be transparent for all outgoing waves. These boundary conditions are called transparent-influx boundary conditions (TIBC). Such boundary conditions will be derived as follows. Outside the scattering structure, the Helmholtz equation is linear and has a constant refractive index  $n_0$ . Therefore this equation can be factorized as

$$\left( \frac{d}{dz} - ikn_0 \right) \left( \frac{d}{dz} + ikn_0 \right) E = 0, \quad (2.8)$$

yielding the following boundary conditions:

$$\frac{dE}{dz} - ikn_0 E = -2ikn_0 A_{inc}, \quad z = z_{\min} \quad (2.9)$$

$$\frac{dE}{dz} + ikn_0 E = 0, \quad z = z_{\max}. \quad (2.10)$$

The first boundary condition (2.9) is an influx condition for an incident wave with wavenumber  $k$  and constant amplitude  $A_{inc}$  and is simultaneously transparent for the back scattered field. The second condition (2.10) is a transparent boundary condition for the right-traveling wave.

Throughout this chapter we deal with a one-dimensional finite quarter-wavelength stack which is composed of alternating layers which have a high refractive index  $n_H$  (denoted as  $H$  layer) and a low refractive index  $n_L$  (denoted as  $L$  layer). Figure 2.1 illustrates the geometry. The thicknesses for the two kinds of layers are such that

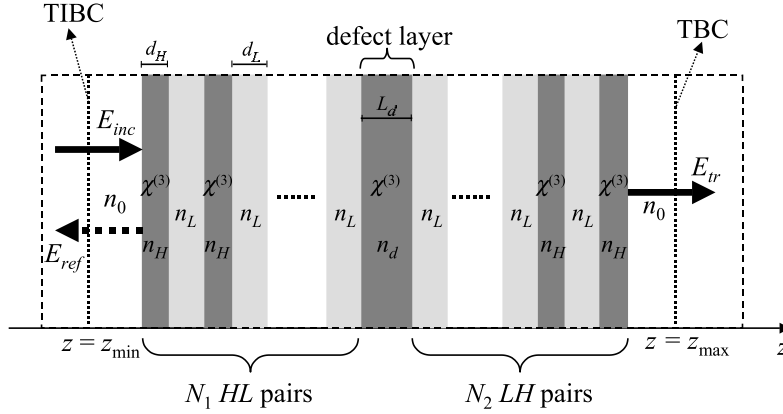


Figure 2.1: Schematic view of the 1D PBG structures considered in this paper which are composed of  $N_1$   $HL$  layers and  $N_2$   $LH$  layers separated by a defect layer with thickness  $L_d = M \times (\lambda_0/4n_d)$ . The thicknesses of layers  $H$  and  $L$  are respectively  $d_H = \lambda_0/4n_H$  and  $d_L = \lambda_0/4n_L$ . The medium outside the structure is linear homogeneous with refractive index  $n_0$ . For the numerical calculations we introduce a transparent-influx boundary condition (TIBC) and transparent boundary condition (TBC) in the left and right hand side of the structure.

$d_L = \lambda_0/4n_L$  and  $d_H = \lambda_0/4n_H$ , where  $\lambda_0$  is the free-space design wavelength. We assume that the front and back media have refractive index  $n_0$ . It is also assumed that the high-index layer shows a positive Kerr nonlinearity. The defect structure can be obtained by simply perturbing the thickness of any layer (which is then called a defect layer, denoted by  $D$ ) or by changing the refractive index of the defect layer. For simplicity we denote this structure  $(HL)^{N_1}(D)^M(LH)^{N_2}$ , where  $N_1$  and  $N_2$  are respectively the number of layer periods in the left and right of the defect layer. Here  $M$  determines the thickness of the defect layer  $L_d$  such that  $L_d = M \times (\lambda_0/4n_d)$  where  $n_d$  is the refractive index of the defect layer.

## 2.3 Numerical Method

### 2.3.1 Linear scheme

In this section we discuss a numerical method to solve Equation (2.7) based on a variational method. We first concentrate to only the linear part, i.e. where  $\chi^{(3)} = 0$  and consider the functional

$$\mathcal{F}_{Lin}(E) = -\frac{1}{2} \int_l^L \left( \left| \frac{dE}{dz} \right|^2 - k^2 n^2 |E|^2 \right) dz \quad (2.11)$$

where  $l < z_{min}$  and  $L > z_{max}$ . This functional can also be written as

$$\mathcal{F}_{Lin}(E) = \mathcal{F}_1(E) + \mathcal{F}_2(E) + \mathcal{F}_3(E) \quad (2.12)$$

where

$$\begin{aligned} \mathcal{F}_1(E) &= -\frac{1}{2} \int_l^{z_{min}} \left( \left| \frac{dE}{dz} \right|^2 - k^2 n_0^2 |E|^2 \right) dz, \\ \mathcal{F}_2(E) &= -\frac{1}{2} \int_{z_{min}}^{z_{max}} \left( \left| \frac{dE}{dz} \right|^2 - k^2 n^2 |E|^2 \right) dz, \\ \mathcal{F}_3(E) &= -\frac{1}{2} \int_{z_{max}}^L \left( \left| \frac{dE}{dz} \right|^2 - k^2 n_0^2 |E|^2 \right) dz. \end{aligned}$$

As it is assumed that the medium outside the grating structure is linear homogeneous with refractive index  $n_0$ , without loss of generality, the solution of equation (2.7) can be written as

$$E(z) = \begin{cases} A_{inc} \exp(-ikn_0(z - z_{min})) + A_{ref} \exp(ikn_0(z - z_{min})) & , z \in [l, z_{min}]; \\ E(z) & , z \in [z_{min}, z_{max}]; \\ A_{tr} \exp(-ikn_0(z - z_{max})) & , z \in [z_{max}, L]; \end{cases} \quad (2.13)$$

where  $A_{inc}$  and  $A_{ref}$  are respectively the amplitudes of the incident and the reflected waves and  $A_{tr}$  is the transmitted wave amplitude. By substituting Equation (2.13) into the functional (2.12), one can check that

$$\begin{aligned} \mathcal{F}_1 &= -\frac{kn_0}{\sin(kn_0\tilde{l})} \left[ \cos(kn_0\tilde{l}) (|E_0|^2 + |E_l|^2) - (E_0 E_l^* + E_0^* E_l) \right] \\ \mathcal{F}_3 &= -\frac{kn_0}{\sin(kn_0\tilde{L})} \left[ \cos(kn_0\tilde{L}) (|E_{M_0}|^2 + |E_L|^2) - (E_{M_0} E_L^* + E_{M_0}^* E_L) \right] \end{aligned}$$

where  $\tilde{l} = l - z_{min}$ ,  $\tilde{L} = z_{max} - L$ ,  $E_0 = E(z_{min})$ ,  $E_l = E(l)$ ,  $E_{M_0} = E(z_{max}) = A_{tr}$  and  $E_L = E(L)$ ; and  $E^*$  states for the complex conjugate of  $E$ . Then one can show that if the variational derivative of functional (2.12) vanishes,  $\delta_E \mathcal{F}_{Lin} = 0$ , then the field  $E(z)$  satisfies the linear part of the NLH equation (2.7) and its boundary conditions (2.9) and (2.10). To derive the numerical scheme, we approximate the functional  $\mathcal{F}_2(E)$  by writing the function  $E(z)$  as a linear combination of a linear "hat" basis function  $\{\varphi_m(z)\}_0^{M_0}$ :

$$E(z) \cong \sum_{j=0}^{M_0} \hat{E}_j \varphi_j(z) \quad (2.14)$$

such that

$$\mathcal{F}_2(E) \cong \tilde{\mathcal{F}}_2(\hat{E}) \quad (2.15)$$

where  $\widehat{E} = \left( \widehat{E}_0, \widehat{E}_1, \dots, \widehat{E}_{M_0} \right)^T$ . Here we assume that the interval  $[z_{\min}, z_{\max}]$  is divided into  $M_0$  subintervals of equal length  $h = (z_{\max} - z_{\min})/M_0$  by choosing the nodal points  $z_j = z_{\min} + jh$  for  $j = 0, 1, \dots, M_0$ .  $\widehat{E}_j$  is the approximation of  $E(z)$  at  $z = z_j$ . The condition  $\delta_E \mathcal{F}_{Lin} = 0$  therefore corresponds to  $\nabla \widetilde{\mathcal{F}_{Lin}}(\widehat{E}) = 0$  which leads to the finite element scheme (by assuming that each discontinuity of the structure coincides with a grid point)

$$\left( \frac{1}{h}P + \frac{1}{6}hk^2Q \right) \widehat{E} = v, \quad (2.16)$$

where

$$P = \begin{pmatrix} -1 - ikn_0 & 1 & 0 & \cdot & \cdot & 0 \\ 1 & -2 & 1 & 0 & \cdot & \cdot \\ 0 & \cdot & \cdot & \cdot & \cdot & 0 \\ \cdot & \cdot & 0 & 1 & -2 & 1 \\ 0 & \cdot & \cdot & 0 & 1 & -1 - ikn_0 \end{pmatrix},$$

$$Q = \begin{pmatrix} 2\widehat{n}_0^2 & \widehat{n}_0^2 & 0 & \cdot & \cdot & 0 \\ \widehat{n}_0^2 & 2(\widehat{n}_0^2 + \widehat{n}_1^2) & \widehat{n}_1^2 & 0 & \cdot & \cdot \\ 0 & \cdot & \cdot & \cdot & \cdot & 0 \\ \cdot & \cdot & 0 & \widehat{n}_{M_0-2}^2 & 2(\widehat{n}_{M_0-2}^2 + \widehat{n}_{M_0-1}^2) & \widehat{n}_{M_0-1}^2 \\ 0 & \cdot & \cdot & 0 & \widehat{n}_{M_0-1}^2 & 2\widehat{n}_{M_0-1}^2 \end{pmatrix},$$

and  $v = \left( -2ikn_0A_{inc} \ 0 \ \dots \ 0 \right)^T$  and  $\widehat{n}_j$  is the linear refractive index in the interval  $(z_j, z_{j+1})$ . In the following this scheme is called the standard FEM.

We will examine the order of accuracy of the standard FEM. For uniform medium with index  $n$ , the  $j$ th equation of (2.16) can be written as

$$\delta_z^2 \widehat{E}_j + \frac{1}{6}k^2\widehat{n}^2 \left( \widehat{E}_{j-1} + 4\widehat{E}_j + \widehat{E}_{j+1} \right) = 0, \quad (2.17)$$

where

$$\delta_z^2 \widehat{E}_j = \frac{1}{h^2} \left( \widehat{E}_{j+1} - 2\widehat{E}_j + \widehat{E}_{j-1} \right).$$

Using a Taylor expansion, it can be shown that

$$\frac{d^2 E(z_j)}{dz^2} = \delta_z^2 \widehat{E}_j - \frac{h^2}{12} \frac{d^4 E(z_j)}{dz^4} + \mathcal{O}(h^4), \quad (2.18)$$

$$\frac{d^2 E(z_j)}{dz^2} + k^2\widehat{n}^2 E(z_j) = \delta_z^2 \widehat{E}_j + \frac{1}{6}k^2\widehat{n}^2 \left( \widehat{E}_{j-1} + 4\widehat{E}_j + \widehat{E}_{j+1} \right) + \text{Res}, \quad (2.19)$$

where  $\text{Res} = -\frac{1}{12}k^2\widehat{n}^2 h^2 \frac{d^2 E(z_j)}{dz^2} + \mathcal{O}(h^4)$ . This shows that the standard scheme (2.17) for the interior point is only second order accurate. The accuracy of the standard discrete boundary conditions can be checked as follows. First we discretized the TIBC at  $z = z_{\min}$ , see Equation (2.9), using a central difference

$$\frac{1}{2h} \left( \widehat{E}_1 - \widehat{E}_{-1} \right) - ikn_0 E_0 = -2ikn_0 A_{inc}, \quad (2.20)$$

which is an  $\mathcal{O}(h^2)$  approximation. Then this approximation is used to eliminate the term  $\widehat{E}_{-1}$  in Equation (2.19) for  $j = 0$  to recover the standard FEM at the left boundary (and similarly for the right boundary). Because both Equation (2.19) and (2.20) are of  $\mathcal{O}(h^2)$ , the standard FEM at the boundaries is also  $\mathcal{O}(h^2)$ .

Now we wish to improve the order of accuracy of the standard scheme (2.16). By applying the central difference to the first term of Res and adding it to (2.19) we obtain a fourth-order scheme

$$\frac{d^2 E(z_j)}{dz^2} + k^2 \widehat{n}^2 E(z_j) = \left(1 - \frac{1}{12} k^2 \widehat{n}^2 h^2\right) \delta_z^2 \widehat{E}_j + \frac{1}{6} k^2 \widehat{n}^2 \left(\widehat{E}_{j-1} + 4\widehat{E}_j + \widehat{E}_{j+1}\right) + \mathcal{O}(h^4) \quad (2.21)$$

which leads to a linear system of equations (after modifying the boundary condition in a similar way)

$$\left(\frac{1}{h} P_1 + \frac{1}{6} h k^2 Q\right) \widehat{E} = v_1, \quad (2.22)$$

where

$$P_1 = \begin{pmatrix} -\alpha_0(1 + i h k n_0) & \alpha_0 & 0 & \cdot & \cdot & \cdot & 0 \\ \alpha_0 & -(\alpha_0 + \alpha_1) & \alpha_1 & 0 & \cdot & \cdot & 0 \\ 0 & \cdot & \cdot & \cdot & \cdot & \cdot & 0 \\ \cdot & \cdot & 0 & \alpha_{M_0-2} & -(\alpha_{M_0-2} + \alpha_{M_0-1}) & \alpha_{M_0-1} & \cdot \\ 0 & \cdot & \cdot & 0 & \alpha_{M_0-1} & -\alpha_{M_0-1}(1 + i h k n_0) & \cdot \end{pmatrix},$$

with  $\alpha_j = 1 - \frac{1}{12} k^2 \widehat{n}_j^2 h^2$  and  $v_1 = \left(-2ikn_0 A_{inc} (1 + k^2 n_0^2 h^2 / 12) \quad 0 \quad \dots \quad 0\right)^T$ . Notice that the resulting matrix is still a tridiagonal and symmetric. This fourth-order scheme is called improved FEM.

Based on our numerical experiments we found that the numerical amplitude and phase error of the standard FEM is of  $\mathcal{O}(h^2)$ . When we apply the improved FEM to both a uniform structure and structure  $(HL)^N(L)(LH)^N$  with respectively  $N = 2$  and  $N = 10$ , the numerical results show that the numerical error is indeed  $\mathcal{O}(h^4)$ , as expected.

### 2.3.2 Nonlinear scheme

In the previous section we have discussed a numerical method to solve the linear Helmholtz equation. Here we consider the complete NLH (2.7). The numerical method is basically the same as for the linear case but with an additional nonlinear term  $k^2 \chi^{(3)}(z) |E(z)|^2 E(z)$ . The functional (2.11) has to be extended with

$$\mathcal{F}_{NL}(E) = \frac{1}{4} \int_{z_{\min}}^{z_{\max}} k^2 \chi^{(3)}(z) |E|^4 dz. \quad (2.23)$$

As in the previous section, we approximate the additional contribution  $\mathcal{F}_{NL}$  as follows

$$\begin{aligned}\mathcal{F}_{NL}(E) &\cong \widetilde{\mathcal{F}_{NL}}(\widehat{E}) \\ &= \frac{\hbar}{20}k^2 \sum_{j=0}^{M_0-1} \chi_j^{(3)} \widetilde{\mathcal{F}_{NLj}}\end{aligned}\quad (2.24)$$

where  $\chi_j^{(3)}$  is the nonlinear coefficient in the interval  $(z_j, z_{j+1})$  and

$$\begin{aligned}\widetilde{\mathcal{F}_{NLj}} &= \left|\widehat{E}_j\right|^4 + \frac{1}{2}\left|\widehat{E}_j\right|^2 \left(\widehat{E}_j\widehat{E}_{j+1}^* + \widehat{E}_j^*\widehat{E}_{j+1}\right) + \frac{1}{3}\left|\widehat{E}_j\right|^2 \left|\widehat{E}_{j+1}\right|^2 \\ &\quad + \frac{1}{6}\left(\widehat{E}_j^2\widehat{E}_{j+1}^{*2} + 2\left|\widehat{E}_j\right|^2 \left|\widehat{E}_{j+1}\right|^2 + \widehat{E}_j^{*2}\widehat{E}_{j+1}^2\right) \\ &\quad + \frac{1}{2}\left|\widehat{E}_{j+1}\right|^2 \left(\widehat{E}_j\widehat{E}_{j+1}^* + \widehat{E}_j^*\widehat{E}_{j+1}\right) + \left|\widehat{E}_{j+1}\right|^4.\end{aligned}\quad (2.25)$$

The partial derivatives of  $\widetilde{\mathcal{F}_{NL}}(\widehat{E})$  are

$$\begin{aligned}\frac{\partial \widetilde{\mathcal{F}_{NL}}}{\partial \widehat{E}_j} &= \mu_{j-1} \left( \frac{2}{3}\widehat{E}_{j-1}\widehat{E}_j^* + \left|\widehat{E}_{j-1}\right|^2 + 2\left|\widehat{E}_j\right|^2 \right) \widehat{E}_{j-1} \\ &\quad + \mu_{j-1} \left( \widehat{E}_j\widehat{E}_{j-1}^* + \frac{4}{3}\left|\widehat{E}_{j-1}\right|^2 + 4\left|\widehat{E}_j\right|^2 \right) \widehat{E}_j \\ &\quad + \mu_j \left( \widehat{E}_j\widehat{E}_{j+1}^* + \frac{4}{3}\left|\widehat{E}_{j+1}\right|^2 + 4\left|\widehat{E}_j\right|^2 \right) \widehat{E}_j \\ &\quad + \mu_j \left( \frac{2}{3}\widehat{E}_{j+1}\widehat{E}_j^* + \left|\widehat{E}_{j+1}\right|^2 + 2\left|\widehat{E}_j\right|^2 \right) \widehat{E}_{j+1},\end{aligned}\quad (2.26)$$

where  $\mu_j = \hbar k^2 \chi_j^{(3)} / 20$ . Adding the nonlinear term (2.26) to the linear scheme (2.22), we obtain:

$$\left( \frac{1}{\hbar}P_1 + \frac{1}{6}\hbar k^2 Q + R(\widehat{E}) \right) \widehat{E} = v, \quad (2.27)$$

where  $\nabla \widetilde{\mathcal{F}_{NL}}(\widehat{E}) = R(\widehat{E}) \cdot \widehat{E}$ .

### 2.3.3 Nonlinear solver

We notice that our numerical scheme (2.27) is a system of nonlinear equations. The standard approach to solve a nonlinear system is a fixed-point iterative method which in our case is given by

$$\left( \frac{1}{\hbar}P_1 + \frac{1}{6}\hbar k^2 Q + R(\widehat{E}^{(m)}) \right) \widehat{E}^{(m+1)} = v, \quad (2.28)$$

where  $m = 1, 2, 3, \dots$  is the iteration step with  $\widehat{E}^{(1)}$  is taken from the solution of the linear problem. The iteration process is stopped when

$$\left\| \widehat{E}^{(m+1)} - \widehat{E}^{(m)} \right\| < \varepsilon \quad (2.29)$$

for small  $\varepsilon$ . For the calculation in this chapter we set the tolerance  $\varepsilon = 10^{-6}$ .

In general the fixed-point iterative algorithm leads to a convergent solution when there exist a unique solution. However, in the case of bistability where the solution is not unique, this iterative method may not converge. As an example, we implement the fixed-point iterative method (2.28) to calculate the transmissivity  $|T|^2 = \left| \widehat{E}_M / A_{inc} \right|^2$  of a nonlinear structure  $(HL)^6(D)^2(LH)^6$  with input intensity  $1.004558 \text{ kW/m}^2$  (see Figure 2.16.(b) for other parameters). Remark that this example represents a situation around the jumping area from the low-output state into the high-output state. We plot the calculated transmissivity using iterative scheme (2.28) for each iteration step in Figure 2.2 (dotted-line). It is seen that the fixed-point iterative method has a non-convergent solution. In order to take care of the divergence problem in the fixed-point iterative method, we replace the argument of  $R$  in (2.28) with the weighted averaged of  $\widehat{E}^{(m-1)}$  and  $\widehat{E}^{(m)}$  such that

$$\left( \frac{1}{h} P_1 + \frac{1}{6} h \omega^2 Q + R \left( \widehat{E}^{(m-1/2)} \right) \right) \widehat{E}^{(m+1)} = v, \quad (2.30)$$

where  $\widehat{E}^{(m-1/2)} = \sigma \widehat{E}^{(m)} + (1 - \sigma) \widehat{E}^{(m-1)}$  with  $\sigma$ , satisfying  $0 < \sigma \leq 1$ , is a parameter used to control the weight of  $\widehat{E}^{(m)}$ . Note that if we take  $\sigma = 1$  then it leads to the standard fixed-point iterative method. Since  $\widehat{E}^{(m-1/2)}$  is between  $\widehat{E}^{(m)}$  and  $\widehat{E}^{(m-1)}$ , if the series  $\widehat{E}^{(m)}$  is convergent then the series  $\widehat{E}^{(m-1/2)}$  is also convergent; and furthermore both of those series have the same limit. Based on our numerical experiments, the iterative method (2.30) produces convergent solutions for sufficiently small values of  $\sigma$ . However the smaller  $\sigma$  needs a larger number of iterations. As an example, we plot in Figure 2.2 the calculated transmissivity of a defect structure using the weighted-averaged fixed-point iterative method (2.30) as a function of the iteration number for  $\sigma = 1/3$  and  $1/10$ , respectively. We see here that scheme (2.30) has a convergent solution with  $|T|^2 = 0.6254$  after approximately 90 iterations for  $\sigma = 1/3$  (dashed-line) and 200 iterations for  $\sigma = 1/10$  (dashed-dotted-line). For  $\sigma = 1/2$  the iterative scheme (2.30) does not leads to a convergent solution and the result is not shown.

We notice that the iterative method (2.30) is only converging to one solution, whereas in the case of bistability there are two stable solutions. Therefore we still need to find another solution besides the one obtained from (2.30). Considering the nature of bistability, i.e. the transmissivity depends not only on the input intensity alone but also on the history of it, Lu *et al.* [14] suggest to include the history of the input intensity in the calculation. Following this suggestion, we start by solving (2.30) for a very low incident amplitude  $A_{inc}^{(0)}$  that is relatively far from the bistability using the linear solution as an initial guess  $\widehat{E}^{(1)}$ . Then we use the solution of this calculation as a starting point for  $A_{inc}^{(1)} > A_{inc}^{(0)}$  and so on. In this algorithm, when the incident amplitude increases from  $A_{inc}^{(0)}$ , the solutions only correspond to the low-transmission level until the transmission jumps to the high-transmission level. On the contrary, if



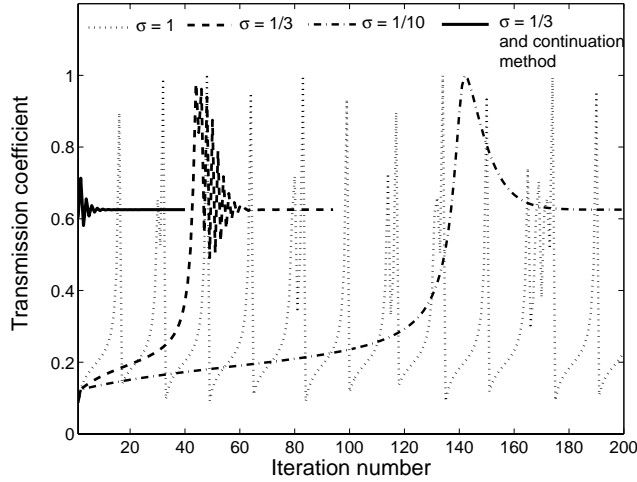


Figure 2.2: Transmissivity of a nonlinear defect structure  $(HL)^6(D)^2(LH)^6$  with input intensity  $1.004558 \text{ kW/m}^2$  (for other parameters see Figure 2.16.(b)) as a function of the iteration number calculated by the standard fixed-point iterative method ( $\sigma = 1$ , dotted-line); by the weighted-averaged fixed-point iterative method with  $\sigma = 1/3$  (dashed-line) and  $\sigma = 1/10$  (dashed-dotted-line), respectively; and by combination of the weighted-averaged fixed-point iterative method ( $\sigma = 1/3$ ) and the continuation method (full-line).

we decrease the amplitude of the input wave from the high-transmission state then we can find another stable solution. Thus this algorithm, called the continuation method, can be used to assess the optical bistability. Another advantage of the continuation method is that the number of iterations is much smaller if we compare with the weighted-averaged iterative method alone (2.30), see Figure 2.2 (full-line).

As we will see in the following section, optical bistability in a finite grating can be tuned either by the frequency or the intensity of the input light. In the latter case, for a fixed frequency light propagation through the multilayer structures, optical bistability manifests itself by a non-unique dependence of the transmission on the intensity of the incident wave. Contrarily, when viewing the input intensity as a function of the transmission, the dependence was observed to be unique. Therefore, in order to improve the performance of finite element scheme (2.27), we use the transmitted wave as the input parameter instead of the incident wave. This approach is called a fixed output problem. As stated in (2.13), the transmitted wave in the homogeneous medium beyond the defect structure is of the form

$$E(z) = A_{tr} \exp(-ikn_0(z - z_{\max})), \quad z \geq z_{\max}. \quad (2.31)$$

Without loss of generality, we assume that the transmitted wave amplitude  $A_{tr}$  is a

real constant. Consequently the value of the incident wave amplitude  $A_{inc}$  now can be a complex number. In this approach the nonlinear system (2.22) is reformulated such that  $A_{inc}$  is included as an unknown variable and  $A_{tr}$  is the input parameter:

$$\left( \begin{array}{c} \left( \begin{array}{c} 2ik(1 + k^2 n_0^2 h^2 / 12) \\ 0 \\ \vdots \\ 0 \\ (0) \end{array} \right) \\ \left( \frac{1}{h} P_1 + \frac{1}{6} h k^2 Q + R(\hat{E}) \right) \\ \left( \begin{array}{cccc} 0 & \cdots & 0 & 1 \end{array} \right) \end{array} \right) \begin{pmatrix} A_{inc} \\ \hat{E}_0 \\ \hat{E}_1 \\ \vdots \\ \hat{E}_{M_0-1} \\ \hat{E}_{M_0} \end{pmatrix} = \begin{pmatrix} 0 \\ \vdots \\ 0 \\ A_{tr} \end{pmatrix}. \quad (2.32)$$

We solve the nonlinear system (2.32) using a standard fixed-point iterative method. Since the scheme (2.32) produces a unique relation between the transmitted wave and the incident wave, we can expect that the convergence of this approach is much faster than that of the fixed input problem. As an example, the scheme (2.32) only needs four iterations to solve a problem related to Figure 2.2, while scheme (2.30) using  $\sigma = 1/3$  combined with a continuation method requires 40 iterations! Furthermore, as shown in next section, the fixed output approach can find all stable and unstable solutions related to a specific incident, whereas the fixed input method does not give access to unstable solutions. Hence, for the calculation of the optical bistability controlled by the the input intensity, we will only implement the fixed output scheme (2.32).

## 2.4 Optical bistability in 1D PBG structure

In this section we apply the numerical scheme that was derived in the previous section to study the transmission properties of quarter-wavelength stacks as shown in Figure 2.1. For both linear and nonlinear numerical calculations we take  $n_L = 1.25$  and  $n_H = 2.5$ . Unless it is mentioned otherwise, the refractive index of the input and output regions  $z < z_{\min}$  and  $z > z_{\max}$  is assumed to be  $n_0 = 1$  and that of the defect layer is  $n_d = n_H$ . The computational window is divided into  $M_0$  equidistant elements with grid size  $h = \lambda_0/400$ . All results given have been found to have converged with respect to a refinement of the discretization and with respect to the iteration number. Before proceeding with the nonlinear case, we first discuss the linear structure by setting  $\chi^{(3)} = 0$ . For a linear structure  $(HL)^4(D)(LH)^4$  with total computational window  $3.5\lambda_0$  (the length of each uniform layer in the left and the right parts of the grating structure is  $\lambda_0/2$ ), applying the improved FE scheme in place of the original one allows us to reduce the number of elements from about 5600 that are necessary to compute equally accurate results with scheme (2.16) to a number of 1400 for scheme (2.22). Within this accuracy, if we compare the results of the analytical transfer matrix method, the improved FEM gave no observable differences on the scale of figures presented in this section. For the nonlinear structure, however, we do

not have an exact analytical solution. Therefore we compared our numerical results of bistability controlled by the input intensity with those of the nonlinear transfer matrix method [7], using the full nonlinear interface conditions [1]. We remark that the nonlinear transfer matrix method is valid only for the case of weak nonlinearity. We observed a very good agreement between those two methods for the case of a defect structure but not for a perfect structure. This can be understood from the fact that the maximum change of refractive index due to nonlinearity in an ideal structure is much bigger than that of a defect structure. Another remark is that the FEM scheme can be used to assess the bistability tuned by input frequency. However, this calculation is very difficult to be done by the nonlinear transfer matrix method.

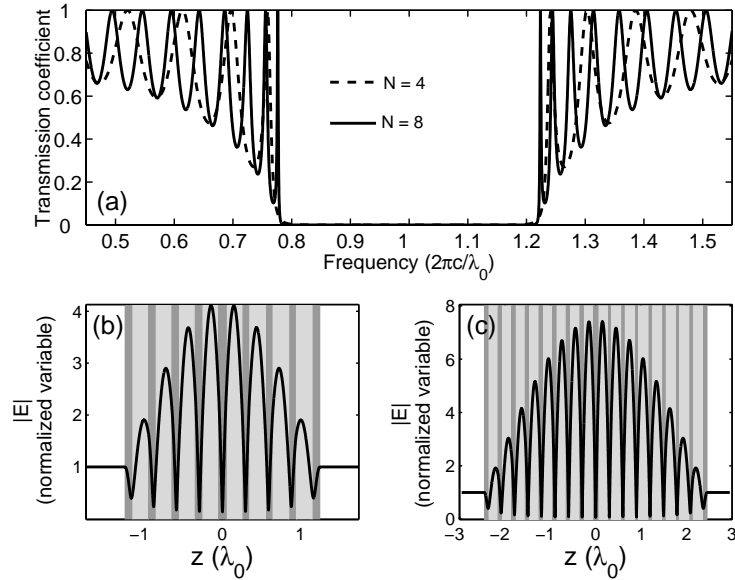


Figure 2.3: (a) Transmission spectra of structure  $(HL)^N(D)(LH)^N$  with  $N = 4$  and  $N = 8$ , respectively. The first band gaps of structure with  $N = 4$  and  $N = 8$  are respectively  $\omega \in (0.75915, 1.24085) \times 2\pi c/\lambda_0$  and  $\omega \in (0.77633, 1.22367) \times 2\pi c/\lambda_0$ . (b) The normalized amplitude of the electric field inside a perfect structure with  $N = 4$  at  $\omega = 1.24085 \times 2\pi c/\lambda_0$ . (c) Same as for (b) but with  $N = 8$  at  $\omega = 1.22367 \times 2\pi c/\lambda_0$ .

#### 2.4.1 Transmission properties of perfect linear PBG structure

As mentioned in section 2.1, a perfect (infinite) PBG structure has an essential property, i.e. the existence of forbidden bands prohibiting a certain range of frequencies of light waves to propagate through them. In other words, the light waves with frequencies inside the band gap are completely reflected by the structure. However, in a finite

periodic structure, the reflection will not be complete in general. Therefore we practically use the term band gap (of a finite structure) for the smallest frequency interval containing the band gap of the infinite structure that is bordered by two resonance frequencies (which are called band-edge modes/resonances). To get a feeling of this definition, we show in Figure 2.3.(a) the transmission spectra around the first band gap of structure  $(HL)^N(D)(LH)^N$  with  $N = 4$  and  $N = 8$ , respectively. As shown in this picture, the increasing number of periods reduces the width of the band gap. If  $N$  is further increased, the band gap interval is closer to the actual band gap, i.e. the interval for an infinite structure, which in this case is between  $\omega = 0.78365 \times 2\pi c/\lambda_0$  and  $\omega = 1.21635 \times 2\pi c/\lambda_0$ . By analogy to the solid state electronics case, the frequency which lies below the band gap is called the valence band (VB) and the upper one is the conduction band (CB). We notice that by adding more layers, the number of resonance frequencies where the transmission equals one is also increased and specifically the resonance at the band-edge becomes sharper. Furthermore, in Figure 2.3.(b) and 2.3.(c) we plot the amplitude inside the structure at a band-edge frequency, respectively, for  $N = 4$  and  $N = 8$ ; showing that the larger  $N$  has a larger amplitude enhancement.

## 2.4.2 Transmission properties of linear PBG structure with a defect

When a defect layer is introduced in a linear PBG structure, a very narrow resonance that is isolated in the band gap occurs. The frequency of such resonance is called a defect mode frequency (see eg. [3] and [22]). This is in contrast with the case of strictly periodic structure where all resonances are concentrated at the border or outside the band gap. In the following paragraphs we discuss the dependence of the defect modes on the thickness, the position and the refractive index of the defect layer and the number of layer periods.

To study the defect mode, we first consider an ideal PBG structure with 17 alternating layers  $(HL)^4(D)^M(LH)^4$ . Then by disturbing the width of the center layer, which has a high refractive index  $n_H$ , we obtain a symmetric defect structure  $(HL)^4(D)^M(LH)^4$ . In Figure 2.4 we show the position of transmission maxima where the transmission coefficient is unity as a function of the defect layer width. The perfect structure, i.e. when the thickness of the center layer is  $\lambda_0/4n_H$  (see dashed line in Figure 2.4) has a band gap which is centered at the frequency  $2\pi c/\lambda_0$ . The shaded-region indicates the width of the first band gap. The band-edge resonances in this case are respectively at  $\omega = 0.75915 \times 2\pi c/\lambda_0$  and  $\omega = 1.24085 \times 2\pi c/\lambda_0$ . When reducing the defect width, the valence band edge moves into the band gap to become a defect mode. Since the defect mode evolves from the valence band with decreasing the defect size, it can be thought of as an acceptor mode (see e.g. Ref. [26]). We note that the acceptor mode frequency increases as the defect size is decreased. On the other hand, if the width of the center layer of our perfect structure is increased the conduction band

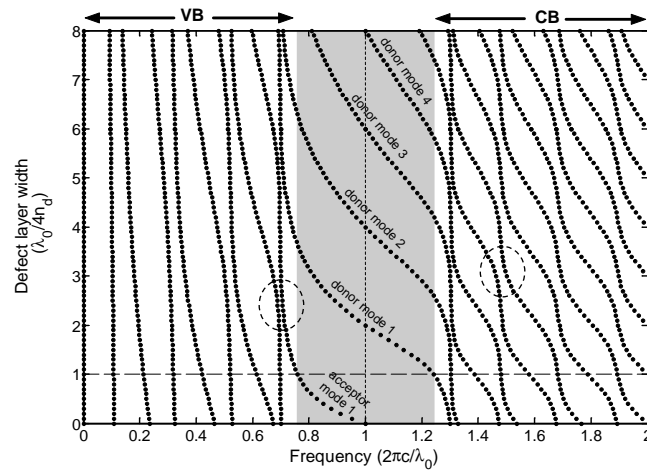


Figure 2.4: The (frequency) position of transmission maxima as a function of the defect layer width for structure  $(HL)^4(D)^M(LH)^4$  with  $n_d = n_H$ . The media in the input and output regions are assumed to be air ( $n_0 = 1$ ). The shaded-area indicates the first band gap of the perfect structure, i.e. when the defect layer is  $\lambda_0/4n_d$  (see the dashed-line). Observe the appearance of acceptor/donor modes caused by changing the defect size. It is noticed that when two transmission maxima outside the band gap meet, they show an anticrossing behavior (see e.g. the circled areas).

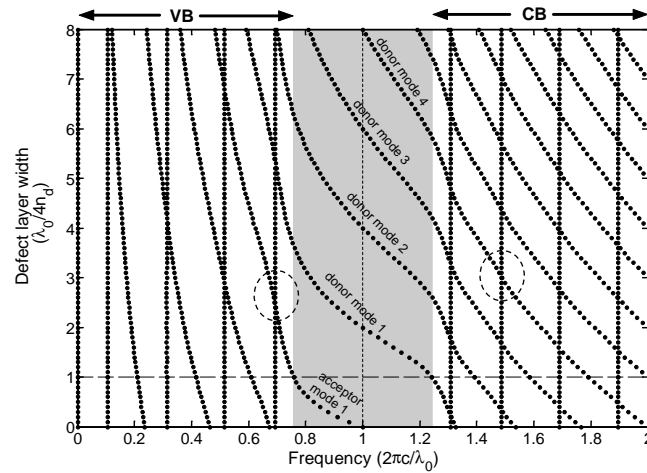


Figure 2.5: The same as Figure 2.4 except that the first and last semi-infinite layers are now assumed to have refractive index  $n_0 = n_L$  instead of  $n_0 = 1$ . Similar to that presented in Figure 2.4, acceptor/donor modes are created as we change the thickness of the defect layer. With disturbing the defect layer, two transmission maxima can merge and split but the frequency of one of these two maxima remain the same.

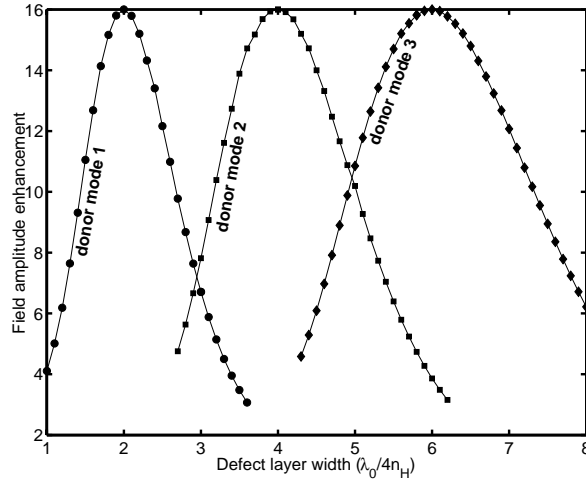


Figure 2.6: The maximum field enhancement inside the defect structure as a function of the defect layer width for donor mode 1, 2 and 3. The largest enhancement factors for these three donor modes are 16 which occur when the defect modes are at  $\omega = 2\pi c/\lambda_0$  and the thickness of the defect layer equals to  $\alpha (\lambda_0/2n_H)$  for integer  $\alpha$ .

edge moves into the band gap region. This type of defect mode is called a donor mode. When the width of the defect layer is further increased more than one defect mode can be obtained. Stanley *et al.* [19] have noticed that the moving behavior of the transmission maxima of the defect structure is identical to the case of solid-states electronic, except for the anticrossing behavior outside the band gap. However, when we assume that the front and the back media have a refractive index  $n_L$  instead of air, the anticrossing behavior cannot be observed anymore (see the circled areas in Figure 2.5). In this case, as we change the defect layer, two transmission maxima outside the band gap merge and then split again with the frequency of one of these maxima remaining constant.

It is well known that the defect mode can enhance the field intensity inside the structure. By assuming that the incident wave amplitude equals to one, we show in Figure 2.6 the enhancement of the field amplitude as a function of the size of the defect layer for donor mode 1, donor mode 2 and donor mode 3, respectively. The field amplitude enhancement here is defined as the maximum field amplitude ( $\max|E|$ ) inside the structure. It is shown in Figure 2.6 that for each donor mode the largest enhancement occurs when the width of the defect layer equals to  $\alpha (\lambda_0/2n_H)$  for integer  $\alpha$ . It can be checked in Figure 2.4 that those donor modes have the same frequency  $\omega = 2\pi c/\lambda_0$ . The maximum enhancement of the field amplitude in this case is sixteen times of the incident wave. Although the enhancement factors of structures with defect thicknesses  $\alpha (\lambda_0/2n_H)$  are the same, the field amplitudes

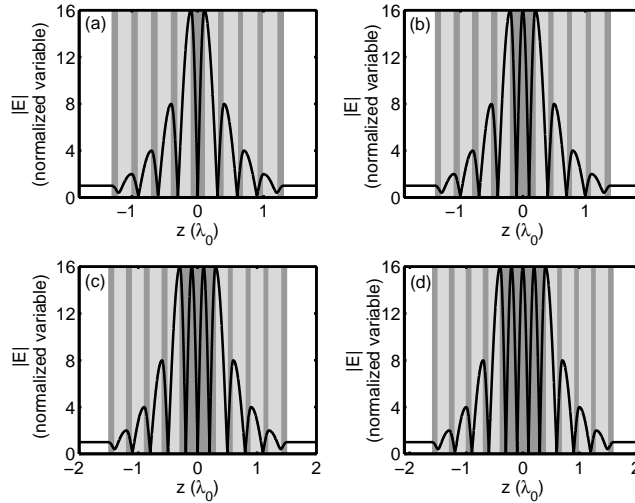


Figure 2.7: The field amplitude  $|E|$  inside the defect structure  $(HL)^4 (D)^M (LH)^4$  with  $n_d = n_H$  for (a)  $L_d = \lambda_0/2n_H$ ; (b)  $L_d = \lambda_0/n_H$ ; (c)  $L_d = 3\lambda_0/2n_H$  and (d)  $L_d = 2\lambda_0/n_H$  at frequency  $\omega = 2\pi c/\lambda_0$ . Observe that the maximum of the amplitude is 16 for all cases. The longer the defect layer is the more amplitude maxima can be observed inside the defect region.

inside the structures are different for different  $\alpha$ . By increasing the value of  $\alpha$  by one an additional field amplitude peak is observed in the structure, see Figure 2.7. Moreover, the change of  $\alpha$  will also change the spectral width of the defect mode. It is clearly seen in Figure 2.8 that the full width at half maximum (FWHM) of the defect mode decreases with increasing  $\alpha$ .

Now we study the influence of the defect position in the structure on the defect mode. We are still considering a structure of 17 alternating layers including 9  $H$  layers and 8  $L$  layers. The defect layer is introduced by changing the size of one of the layer  $H$  to be  $\lambda_0/2n_H$ . The effect of defect position is investigated by moving the defect layer from the left to the right of the structure. It is found that the changing of the defect position disturbs the positions of the transmission maxima outside the band gap. However the position of the defect mode remains the same, i.e. at frequency  $2\pi c/\lambda_0$ . Furthermore, the transmission coefficients of those transmission maxima including the defect mode can be less than one when the defect layer is not located at the center of the structure. Because we are more interested in the defect mode, we plot in Figure 2.9 the transmission coefficient of the defect mode as a function of the position of the defect layer. The incident wave is fully transmitted by the defect structure only when the defect layer is placed in the center of the structure. Otherwise the incident light is partly reflected. Wang *et al.* [24] explained this phenomena by considering the whole defect structure as two smaller structures linked together, i.e. one is structure

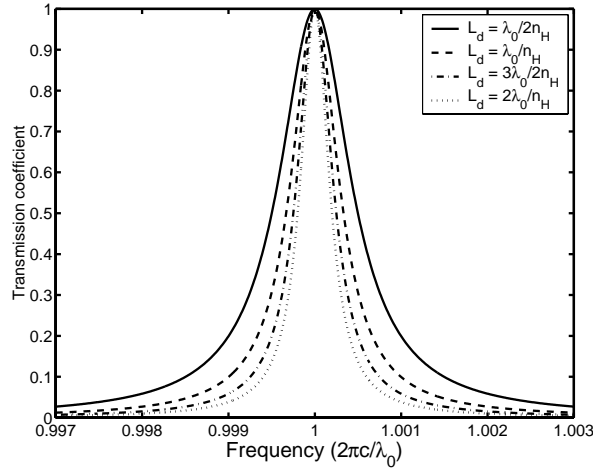


Figure 2.8: The transmission spectrum around the defect mode for different defect layer widths. The spectral width of the defect mode decreases with the increasing defect  $L_d$ .

with a defect in the middle and the other is a perfect structure. Incident light with frequency of the defect mode can pass through the defect part, but is partly reflected by the perfect part because its frequency is in its band gap. Therefore, the structure with a central defect layer has the highest transmission coefficient.

Next we investigate the dependence of the defect mode on the refractive index of the defect layer. The defect structure considered here has the form  $(HL)^4(D)^M(LH)^4$ . The index of the defect layer  $n_d$  is varied from 2 to 4. According to the results of our calculations, an acceptor mode appears in the band gap if the defect thickness is less than  $\lambda_0/4n_d$ . On the contrary, some donor modes can be obtained if the size of the defect layer is greater than  $\lambda_0/4n_d$ . Similar to the previous case the enhancement factor of the field amplitude is sixteen and is obtained when the width of the defect layer is a multiple of  $\lambda_0/2n_d$  (i.e. when  $M$  is an even number) at defect mode frequency  $2\pi c/\lambda_0$ . Furthermore the FWHM of the defect mode of a structure  $(HL)^4(D)^2(LH)^4$  becomes smaller as we increase the refractive index of the defect layer, see Figure 2.10.

Finally we investigate the effect of the number of layer periods by considering the symmetrical structure  $(HL)^N(D)^2(LH)^N$  for  $N = 4, 5, 6, 7$ . The index and the width of the defect layer are chosen to be  $n_H$  and  $2(\lambda_0/4n_H)$ , respectively. Using this structure, a defect mode in the center of the band gap of the corresponding perfect structure can be found. Figure 2.11 shows the field amplitude inside the structure for different  $N$ . The maximum field intensity is changed as the number of periods changes. A larger  $N$  produces a larger field amplitude enhancement. More precisely



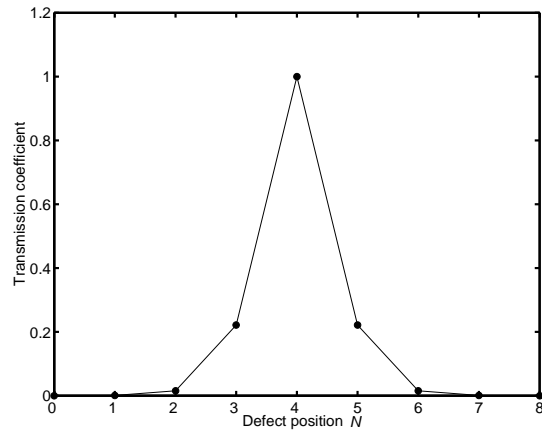


Figure 2.9: The transmission coefficient at  $\omega = 2\pi c/\lambda_0$  of structure  $(HL)^N (D)^2 (LH)^{8-N}$  for  $N = 0, 1, \dots, 8$ . The maximum transmission occurs when the defect layer is placed in the middle of the structure.

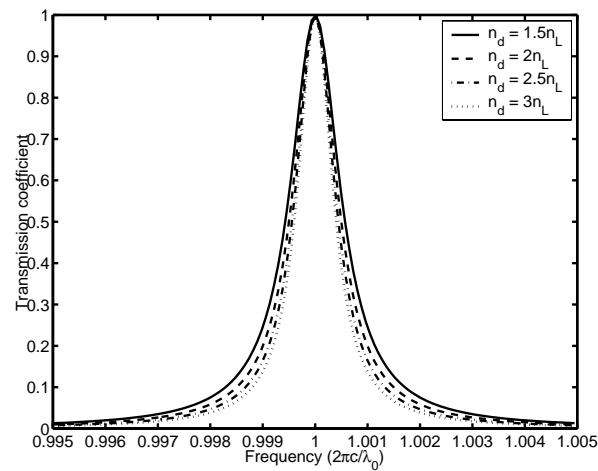


Figure 2.10: The transmission spectrum around the defect mode of a structure  $(HL)^4 (D)^2 (LH)^4$  for different refractive indices of the defect layer. The spectral width of the defect mode decreases when the refractive index of the defect layer is increased.

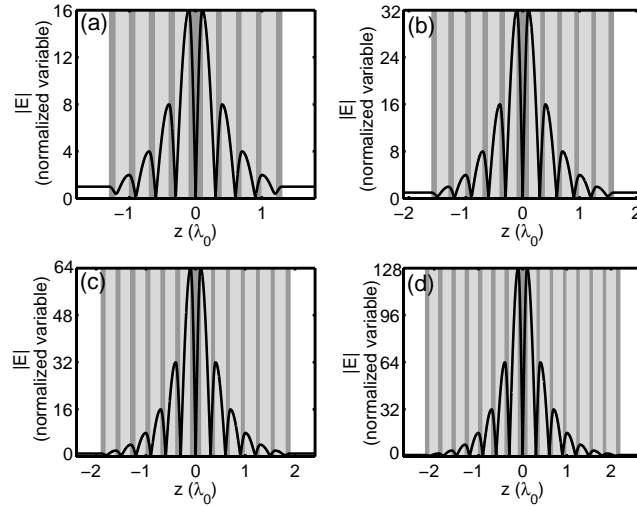


Figure 2.11: The field amplitude  $|E|$  inside the defect structure  $(HL)^N (D)^2 (LH)^N$  with  $n_d = n_H$  and  $L_d = 2(\lambda_0/4n_H)$  for (a)  $N = 4$ ; (b)  $N = 5$ ; (c)  $N = 6$  and (d)  $N = 7$  at frequency  $\omega = 2\pi c/\lambda_0$ . The maximum amplitudes for those cases are  $2^N$ .

the enhancement factors of structures with  $N = 4, 5, 6, 7$  are respectively 16, 32, 64 and 128 which are exactly  $2^N$ . In addition to the increasing field enhancement of the defect mode with respect to the increasing  $N$ , its spectral width also decreases, see Figure 2.12.

It is well known that the enhancement factor and the decrease of the spectral width are important properties for optical bistability. Based on the previous discussion we conclude that to get a high field enhancement a defect structure  $(HL)^{N_1} (D)^M (LH)^{N_2}$  is to be designed such that the defect layer is positioned in the middle of the structure, i.e.  $N_1 = N_2$  with  $M$  being an even integer number. Then the defect mode is located in the center of the band gap. A higher value of  $M$  leads to a smaller FWHM. Increasing the number of grating periods  $N$  yields simultaneously a narrower resonance and a field enhancement that grows exponentially with  $N$ .

### 2.4.3 Bistable switching by frequency tuning

If a Kerr nonlinearity is introduced in the structure, it causes a change of local refractive index. According to Ref. [10] the induced refractive index change is proportional to the intensity of the optical field and can be written as

$$\Delta n = \bar{n}_2 |E|^2 \quad (2.33)$$

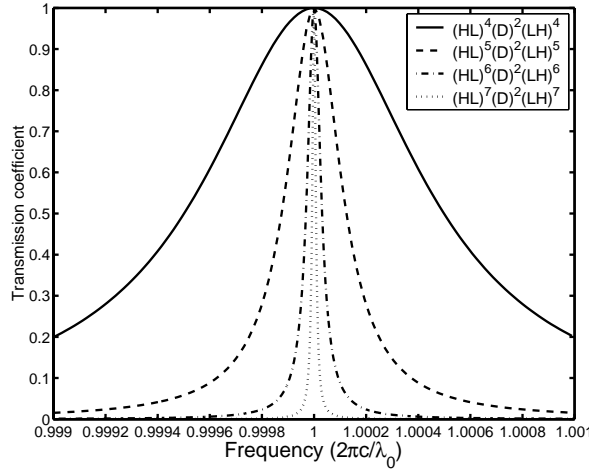


Figure 2.12: The transmission spectrum around the defect mode of the structures  $(HL)^N (D)^2 (LH)^N$  for  $N = 4, 5, 6, 7$ . The spectral width of the defect mode decreases with growing number of periods  $N$ .

where the nonlinear refractive index coefficient  $\bar{n}_2$  of the medium is defined by

$$\bar{n}_2 = \frac{1}{2n} \chi^{(3)}. \quad (2.34)$$

For the numerical calculations of bistability in this chapter, we assume a Kerr nonlinearity with  $\chi^{(3)} = 2 \times 10^{-12} \text{ m}^2\text{V}^{-2}$  is present in all high index layers  $H$  as well as in the defect layer (when considering a defect structure). Due to a change of the effective refractive index, the transmission spectrum will also change accordingly. In general, a positive (negative) nonlinearity has a tendency to shift nonlinearly the entire transmission spectrum to the left (right). Specifically when the resonance is sharp enough, bistability or multistability can be achieved (see. e.g. Agranovich *et al.* [2]). For a strictly periodic structure, bistability usually occurs around the resonance peak at the border of the linear band gap: a positive (negative) nonlinearity effects bistability in the left (right) flanks of the resonance frequencies. For example we show in Figure 2.13 the transmission spectra of the nonlinear structures  $(HL)^N (D) (LH)^N$  for  $N = 4$  and  $N = 8$  respectively in the vicinity of the resonance peak at the top of the first linear band gap. Each spectrum is calculated using a fixed input intensity  $I_{inc}$ . For a certain threshold of  $I_{inc}$ , the spectrum exhibits a bistability phenomenon: by increasing the frequency of a tunable source, the transmission jumps into high-transmission state  $1'$  after it passes point 1. Similarly, the low-transmission state  $2'$  can be reached after passing state 2 when moving in the opposite direction, see Figure 2.13.(a). For  $N = 4$  bistability can be obtained when we set  $I_{inc} = 7.5 \times 10^4 \text{ kW/m}^2$  but not when  $I_{inc} = 4 \times 10^4 \text{ kW/m}^2$ . When the number of layers is increased such that  $N = 8$ , the transmission spectrum already exhibits bistability for  $I_{inc} = 5 \times 10^3$

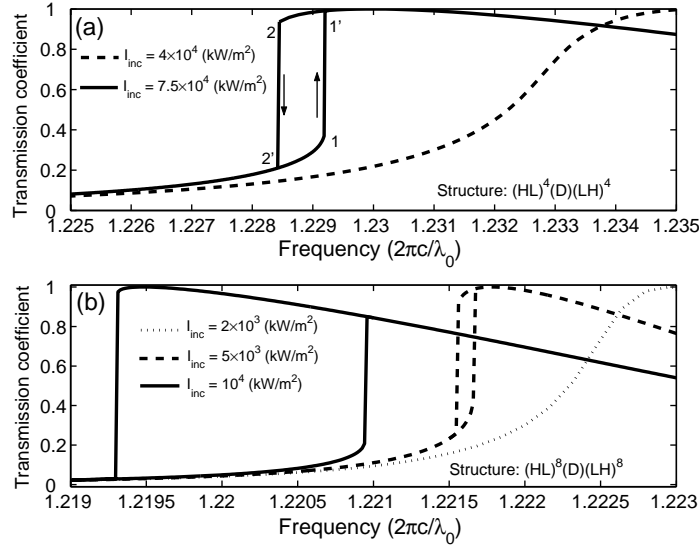


Figure 2.13: Transmission spectra of nonlinear structure  $(HL)^N (D) (LH)^N$  for (a)  $N = 4$  and (b)  $N = 8$ . Observe that for a certain threshold  $I_{inc}$ , a periodic structure can exhibit a bistable switching.

$\text{kW/m}^2$ .

For a nonlinear defect structure the bistability can occur in the vicinity of the resonance peak at the border of the linear band gap or around the defect mode frequency where the resonance is relatively sharp. As we notice before the electric field intensity inside a symmetric defect structure at the defect mode frequency is very high so that we can use it to enhance the nonlinear effect. Therefore bistable behavior can be expected around this frequency with a lower threshold compared with a periodic structure of the same length. And indeed this is confirmed by our numerical calculations. Figure 2.14 shows the transmission spectra of the nonlinear defect structure  $(HL)^4 (D)^2 (LH)^4$  for different  $I_{inc}$ 's. The bistability can already be observed for  $I_{inc} = 100 \text{ kW/m}^2$ .

#### 2.4.4 Bistability controlled by input intensity

The discussion in the previous subsection suggests the possibility for the use of a finite periodic structure as a device in which bistable switching is controlled by frequency tuning while input electric field is maintained at fixed intensity. Furthermore, we also observe that for a certain frequency, e.g.  $\omega = 0.9988 \times 2\pi c/\lambda_0$  in Figure 2.14, the transmissivity is found uniquely for relatively low  $I_{inc}$ , then it is multi-valued

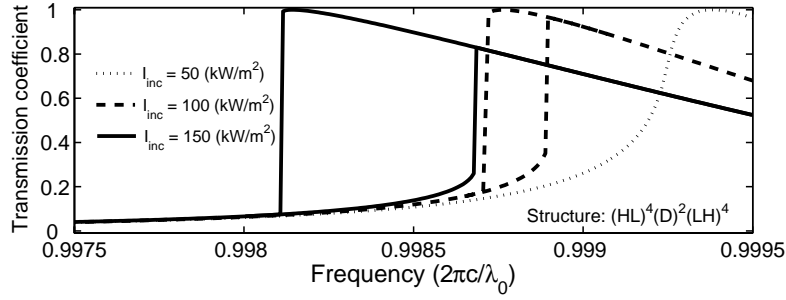


Figure 2.14: Transmission spectra of nonlinear structure  $(HL)^4 (D)^2 (LH)^4$  for different input intensity. The threshold for bistability of a defect structure is much lower than that of a perfect structure with comparable length.

for larger  $I_{inc}$ . However, by increasing the input intensity, the transmissivity can be unique again. This fact also shows the possibility of optical bistability controlled by input light intensity at fixed frequency.

A basic issue of the optical bistability is to realize it with threshold as low as possible. According to the previous discussion, a symmetric defect structure has a much lower threshold of bistability compared to the perfect structure of the same length. Therefore, we restrict our study of bistability controlled by the intensity of the input light only in a symmetric defect structure.

In Figure 2.15 we show the input-output characteristics of structure  $(HL)^4 (D)^2 (LH)^4$  for some frequencies below the defect mode  $\omega = 2\pi c/\lambda_0$ . It is found that for  $\omega = 0.995 \times 2\pi c/\lambda_0$  the structure shows an S-shape response. When the incident intensity ( $I_{inc}$ ) increases slowly from zero, the transmitted intensity ( $I_{tr}$ ) first increases slowly. If the input reaches the upswitching threshold value (about 6228.3 kW/m<sup>2</sup>),  $I_{tr}$  jumps into a higher value (from state 1 to 1', see Figure 2.15.(a)). Then  $I_{tr}$  increases slowly again as we increase the value of  $I_{inc}$ . On the other hand, when  $I_{inc}$  is decreased from the value that is greater than the threshold value,  $I_{tr}$  decreases slowly from the high value. When  $I_{inc}$  reaches the threshold value (state 1'),  $I_{tr}$  does not jump back to lower value (state 1), but it remains to decrease slowly until it reaches state 2, at which it jumps to state 2'. Then  $I_{tr}$  continues to decrease with decreasing  $I_{inc}$ . Thus, the nonlinear defect structure can implement an optical bistability. It should be noticed that the line between the low-output state and high-output state, i.e. the line which connects the state 1 and state 2, corresponds to the unstable solutions.

While the upswitching threshold value for  $\omega = 0.995 \times 2\pi c/\lambda_0$  is very large, this value can be reduced by tuning the frequency of the input light closer to the defect mode. For example, the thresholds for  $\omega = 0.997 \times 2\pi c/\lambda_0$  and  $\omega = 0.999 \times 2\pi c/\lambda_0$  are 1392.8 kW/m<sup>2</sup> and 81.2 kW/m<sup>2</sup> respectively. However, the bistable behavior can

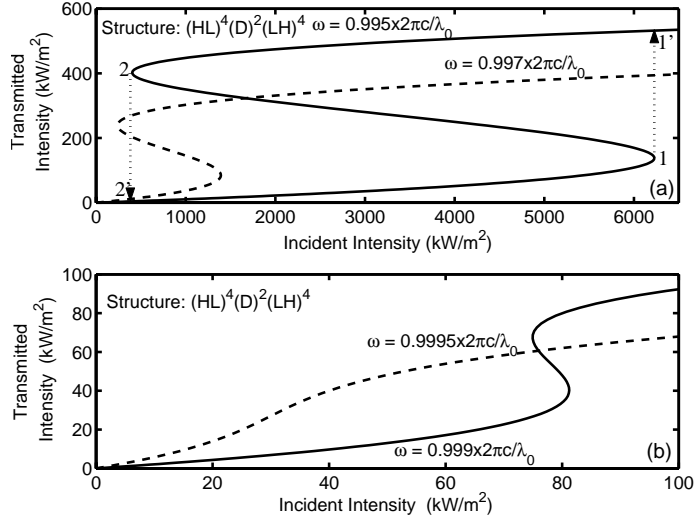


Figure 2.15: The input-output characteristics of a structure  $(HL)^4(D)^2(LH)^4$  with  $n_d = n_H$  for different frequencies where the Kerr nonlinearity is introduced in all high index layers. The bistability threshold decreases when the input light frequency is closer to the defect mode. However, when the frequency is too close to the defect mode (the case of  $\omega = 0.9995 \times 2\pi c/\lambda_0$ ) the bistability cannot be obtained anymore.

not be obtained anymore when the input field has frequency that is very close to the resonance frequency, e.g. in the case of  $\omega = 0.9995 \times 2\pi c/\lambda_0$ , see Figure 2.15.(b). We remark that the change of refractive index due to the Kerr nonlinearity that corresponds to the incident intensity 6228.3 kW/m<sup>2</sup> is  $\sim 0.0412$ , which is relatively large. When the intensity threshold is reduced to 81.2 kW/m<sup>2</sup>, the corresponding refractive index change is  $\sim 0.0063$ .

Now we investigate the effect of the defect thickness to the threshold of the bistability. We show in Figure 2.16.(a) the bistability curve of structure  $(HL)^4(D)^M(LH)^4$  for  $M = 2, 4, 6$ . The optical bistability thresholds are  $\sim 62.28$  kW/m<sup>2</sup> for  $M = 4$  and  $\sim 28.29$  kW/m<sup>2</sup> for  $M = 6$ . It was noticed in the previous section that increasing the defect size does not influence the field enhancement factor but it reduces the FWHM of the defect mode. Therefore, when we increase the value of  $M$ , we should select  $\omega$  to be closer to the defect frequency, see Figure 2.16.(a). We conclude that the narrower the width of the defect mode, the lower the threshold of the bistability will be achieved. This qualitative behavior agrees with the result of the FDTD analysis done by Lixue *et al.* [13].

Based on the previous analysis, it can be stated that for a fixed Kerr constant, the bistability threshold is reduced when the width of the defect mode is smaller or when the enhancement factor is larger. Since an increasing number of grating periods

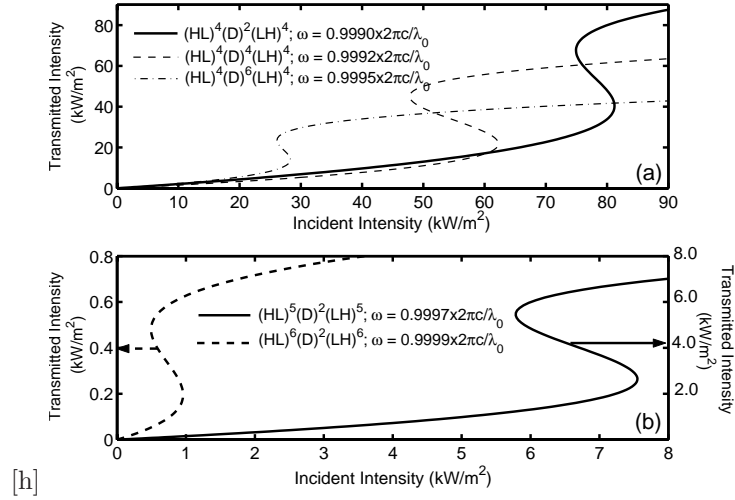


Figure 2.16: The input-output characteristics of structures  $(HL)^N (D)^M (LH)^N$  with  $n_d = n_H$  for different  $M$  and  $N$  where the Kerr nonlinearity is introduced in all high index layers: (a)  $N = 4$  and  $M = 2, 4, 6$ ; (b)  $M = 2$  and  $N = 5, 6$ . In (b) the axis on the left hand side is meant for the structure  $N = 5$  and  $M = 2$ , the transmission for structure  $N = 6$  and  $M = 2$  is to be found on the right hand axis.

produces a smaller FWHM and simultaneously enlarges the enhancement factor, we can expect that a higher number of periods will produce optical bistability with a lower threshold. And indeed, a very low threshold is already obtained when we use a defect structure  $(HL)^N (D)^2 (LH)^N$  for  $N = 5$  or  $N = 6$ . The bistability thresholds in these cases are about  $7.55 \text{ kW/m}^2$  for  $N = 5$  and about  $0.96 \text{ kW/m}^2$  for  $N = 6$  (see Figure 2.16.(b)). The change of refractive index which corresponds to the latter case is only  $\sim 7.6 \times 10^{-4}$ .

## 2.5 Concluding remarks

We have presented a simple numerical scheme based on the variational method to study the optical response of a finite one-dimensional nonlinear grating. Restricting first to the linear case, we improve the standard FEM to get a fourth order accurate scheme maintaining a symmetric-tridiagonal structure of the finite element matrix. For the full nonlinear equation, we implement the improved FEM for the linear part and a standard FEM for the nonlinear part. When using the amplitude of the incident wave as the input parameter, we solve the resulting nonlinear system of equations by implementing a weighted-averaged fixed-point iterative method combined with a continuation method. This approach can capture the bistability phenomenon in nonlinear grating structure as a function of both the frequency or the intensity of the

input light. However, this method can only find the two stable solutions but not the unstable solutions. In case of multistability, it will be very difficult to find more than two stable solutions. In addition, the convergence of the iteration procedure can be very slow in the region of upswitching from low-output level to high-output level. For the case of bistability controlled by the intensity of the input light, the performance of our scheme is improved by using the transmitted wave as the numerical input parameter instead of the incident wave. This approach leads to a unique solution and only needs a standard fixed-point iterative method. Therefore the convergence of the fixed-output approach is much faster than that of the fixed-input method.

When considering a linear PBG structure, we also find that a defect layer can create defect modes. It is found that the shape of a defect mode depends on the thickness, the position and the refractive index of the defect layer as well as on the number of the grating periods. When the defect thickness is less (greater) than  $\lambda_0/4n_d$  then acceptor (donor) modes can be observed in the band gap of the perfect structure. It is found that an optimal field enhancement is obtained when the defect layer is placed in the middle of the structure with the defect thickness being a multiple of  $\lambda_0/2n_d$ . Increasing the defect layer thickness yields a smaller spectral width of the defect mode. A larger enhancement factor and simultaneously a narrower FWHM can be achieved by increasing the number of layer periods.

If a Kerr medium is present either in a perfect structure or in a defect structure, it can cause a bistability phenomenon. The bistability of an ideal grating structure can be obtained by tuning the frequency to a value close to the bottom or top linear band-edge while that of a defect structure can be produced using a frequency near the defect mode or near the linear band-edge. We found that the threshold needed for a defect structure which has good optical features (large field enhancement and narrow resonance) is much lower than that for a strictly periodic structure of the same length. The threshold value can be reduced by increasing the number of layer periods.

We remark that the presented FE scheme implements the 1D NLH equation and exact TIBC without introducing any approximation except the finite element discretization. This is different from the nonlinear transfer matrix formalisms mentioned in section 2.1 that are based on the SVEA and other approximations. Therefore, our method can be used to study the validity of those approximative methods.

While our analysis focuses on layer stacks with step-like refractive indices, the presented method can be applied easily to more general structures, i.e. not necessarily periodic nonlinear gradient or piecewise constant permittivity profiles.



## References

- [1] G.S. Agarwal and S. Dutta Gupta, Effect of nonlinear boundary conditions on nonlinear phenomena in optical resonators, *Opt. Lett.* **12**, p. 829, 1987.
- [2] V.M. Agranovich, S.A. Kiselev, and D.L. Mills, Optical multistability in nonlinear superlattices with very thin-layers, *Phys. Rev.* **B44**, p. 10917, 1991.
- [3] K. Busch, C.T. Chan, and C.M. Soukoulis, Techniques for band structures and defect states in photonic crystals, in Ref. [18], p. 465, 1996.
- [4] W. Chen and D.L. Mills, Optical response of a nonlinear dielectric film, *Phys. Rev.* **B35**, p. 524, 1987.
- [5] W. Chen and D.L. Mills, Optical response of nonlinear multilayer structures: Bilayers and superlattices, *Phys. Rev.* **B36**, p. 6269, 1987.
- [6] J. Danckaert, H. Thienpont, I. Veretennicoff, M. Haelterman, and P. Mandel, Self-consistent stationary description of a nonlinear Fabry-Perot, *Opt. Commun.* **71**, p. 317, 1989.
- [7] J. Danckaert, K. Fobelets, I. Veretennicoff, G. Vitrant and R. Reinisch, Dispersive optical bistability in stratified structures, *Phys. Rev.* **B44**, p. 8214, 1991.
- [8] S. Dutta Gupta and G.S. Agarwal, Dispersive bistability in coupled nonlinear Fabry-Perot resonators, *J. Opt. Soc. Am.* **B4**, p. 691, 1987.
- [9] J. He and M. Cada, Combined distributed feedback and Fabry-Perot structures with a phase-matching layer for optical bistable devices, *Appl. Phys. Lett.* **61**, p. 2150, 1992.
- [10] G.S. He and S.H. Liu, *Physics of Nonlinear Optics* (World Scientific, Singapore, 1999).
- [11] J.D. Joannopoulos, R.D. Meade and J.N. Winn, *Photonic Crystals* (Princeton University Press, Princeton, NJ, 1995).
- [12] E. Lidorikis, K. Busch, Q.M. Li, C.T. Chan, and C.M. Soukoulis, Optical nonlinear response of a single nonlinear dielectric layer sandwiched between two linear dielectric structures, *Phys. Rev.* **B56**, p. 15090, 1997.
- [13] C. Lixue, D. Xiaoxu, D. Weiqiang, C. Liangcai, and L. Shutian, Finite-difference time-domain analysis of optical bistability with low threshold in one-dimensional nonlinear photonic crystal with Kerr medium, *Opt. Commun.* **209**, p. 491, 2002.
- [14] X. Lu, Y. Bai, S. Li and T. Chen, Optical bistability and beam reshaping in nonlinear multilayered structures, *Opt. Commun.* **156**, p. 219, 1998.

- [15] J.H. Marburger and F.S. Felber, Theory of a lossless nonlinear Fabry-Perot interferometer, *Phys. Rev.* **A17**, p. 335, 1978.
- [16] M. Scalora, J.P. Dowling, C.M. Bowden and M.J. Bloemer, Optical limiting and switching of ultrashort pulses in nonlinear photonic band-gap materials, *Phys. Rev. Lett.* **73**, p. 1368, 1994.
- [17] C.M. Soukoulis (ed.), *Photonic Band Gaps and Localization* (Plenum, New York, 1993).
- [18] C.M. Soukoulis (ed.), *Photonic band gap materials* (Kluwer Academic, Dordrecht, 1996).
- [19] R.P. Stanley, R. Houdre, U. Oesterle, M. Illegems and Weisbuch, Impurity modes in one-dimensional periodic-systems - The transition from photonic band-gaps to microcavities, *Phys. Rev.* **A48**, p. 2246, 1993.
- [20] P. Tran, Optical switching with a nonlinear photonic crystal: A numerical study, *Opt. Lett.* **21**, p. 1138, 1996.
- [21] P. Tran, Optical limiting and switching of short pulses by use of a nonlinear photonic bandgap structure with a defect, *J. Opt. Soc. Am.* **B14**, p. 2589, 1997.
- [22] J.O. Vasseur, B. Djafari-Rouhani, L. Dobrzynski, A. Akjouj, and J. Zemmouri, Defect modes in one-dimensional comblike photonic waveguides, *Phys. Rev.* **B59**, p. 13446, 1999.
- [23] R. Wang, J. Dong and D.Y. Xing, Dispersive optical bistability in one-dimensional doped photonic band gap structures, *Phys. Rev.* **E55**, p. 6301, 1997.
- [24] R. Wang, J. Dong and D.Y. Xing, Defect studies in a one-dimensional photonic band gap structure, *Phys. Stat. Sol. (b)* **200**, p. 529, 1997.
- [25] H.G. Winful, J.H. Marburger and E. Garmire, Theory of bistability in nonlinear distributed feedback structures, *Appl. Phys. Lett.* **35**, p. 379, 1979.
- [26] E. Yablonovitch, T.J. Gmitter, R.D. Meade, A.M. Rappe, K.D. Brommer and J.D. Joannopoulos, Donor and acceptor modes in photonic band-structure, *Phys. Rev. Lett.* **67**, p. 3380, 1991.

## Chapter 3

# Deformation of modulated wave groups in Kerr media

### 3.1 Introduction

As is well known, nonlinear optical effects can present itself in large deformations of waves (pulses or beams). One of the widely studied wave deformations in nonlinear Kerr media is modulation instability (MI), i.e. a nonlinear process in which small amplitude and phase perturbations (from noise) of a monochromatic wave grow rapidly under the combined effects of nonlinearity and dispersion, see e.g. [1], [7], [11], [18] and [19]. The phenomenon of MI is also known as Benjamin-Feir instability after Benjamin and Feir found that they were experimentally unable to maintain a nonlinear constant-amplitude wave train of gravity waves in deep water [3]. It has been shown that MI in Kerr media depends on the frequencies of the initial modulations and the power (or amplitude) of the waves. When a small sinusoidal modulation is applied to an input signal in optical fiber, MI can be induced if the side band frequency falls within the MI gain spectrum [12]. This is called an induced MI. If we make use of this induced MI, it is possible to generate a train of soliton-like pulses with a repetition frequency determined by the inverse of the input modulation frequency, see e.g. [10], [17] and [19]. Both MI and induced MI are not only predicted and observed experimentally in temporal domain (pulses) but also in spatial domain (beams), see e.g. [4], [14] and [16]. In the spatial domain, the instability is due to the interplay between the nonlinearity and the diffraction.

In this chapter we discuss the propagation of an initially bichromatic wave in Kerr medium. We will see that when the nonlinearity is strong enough, the envelope of an optical pulse (or beam) that is initially linearly bichromatic (or two linear plane waves with different angle in a spatial domain) can deform substantially, leading

to large variations in both amplitude and phase. Similar properties appear during interaction of bi-soliton solutions; the study of this non-periodic case is simplified by the fact that exact expressions are available, see ([8]). In the periodic case to be considered here, we present numerical calculations and various analytical arguments to arrive at comparable results. In both cases, the characteristic parameter is the quotient of amplitude and the frequency-difference (which is inversely proportional to the modulation period).

In this chapter we focus the study on the deformation of bichromatic pulses. However, as we will see in the following section that the normalized equation for pulse propagation is exactly (mathematically) the same as that for beam propagation, the results of our discussion can be translated for a beam that is initially composed of two plane waves of different angle. The organization of this chapter is as follows. First, in section 3.2, the governing nonlinear Schrödinger (NLS) equation is derived briefly for pulses and beams in materials with Kerr nonlinearity; the derivation specifies the transformation from physical to normalized variables. A detailed derivation of the NLS equation for beams will be given in chapter 4. Besides the standard equation for the complex amplitude, also the phase-amplitude equations are given to explain the envelope deformations which are observed in the results of our numerical calculations (section 3.3). Furthermore, we also show that the envelope can deform to a good approximation in a periodic train of soliton-like waves. In section 3.4 we present three independent arguments to explain the observed deformations when the characteristic parameter exceeds a lower bound. This parameter, i.e. the quotient of wave amplitude and frequency difference of the carrier waves, indicates that smaller frequency differences have the same effect as larger amplitudes. In section 3.5, a low dimensional model will also be derived to describe the bichromatic waves distortion. Conclusions and remarks complete the chapter.

## 3.2 Governing equation

### 3.2.1 Temporal-NLS equation for pulse propagation

We consider the propagation of optical pulses in a single mode fiber and write the effective electric field in the form

$$\mathbf{E}(z, t) = \frac{1}{2} \left\{ F(x, y) A(z, t) e^{i(k_0 z - \omega_0 t)} + \text{c.c.} \right\} \cdot \mathbf{y}, \quad (3.1)$$

where  $F(x, y)$  is the modal field amplitude supported by the fiber,  $\mathbf{y}$  is the polarization unit vector,  $k_0 = K(\omega_0) = \omega_0 n_0 / c$  is the propagation constant (wave number) at the carrier wave frequency  $\omega_0$  and  $A(z, t)$  is the slowly varying complex envelope of the effective electric field. Here  $c$  is the speed of light in vacuum. The refractive index of the fiber medium is taken to be

$$n = n_0 + n_2 |\mathbf{E}|^2, \quad (3.2)$$

where  $n_0$  and  $n_2$  are respectively the linear and nonlinear refractive index. By substituting Equation (3.1) into the wave equation and assuming that the envelope is slowly varying, we obtain a NLS equation for the envelope  $A$  (see e.g. [1] and [15]):

$$i \left( \frac{\partial A}{\partial z} + K' \frac{\partial A}{\partial t} \right) - \frac{1}{2} K'' \frac{\partial^2 A}{\partial t^2} + \gamma |A|^2 A = 0, \quad (3.3)$$

where  $K'$  and  $K''$  are respectively the first and the second derivative of the wave number  $K$  with respect to the frequency  $\omega$  at  $\omega_0$  :

$$K' = \left. \frac{\partial K}{\partial \omega} \right|_{\omega=\omega_0}, \quad K'' = \left. \frac{\partial^2 K}{\partial \omega^2} \right|_{\omega=\omega_0}.$$

Furthermore,  $\gamma$  is a parameter characterizing the nonlinearity of the medium and is defined as

$$\gamma = \frac{n_2 \omega_0}{c A_{eff}}, \quad (3.4)$$

where

$$A_{eff} = \frac{(\int \int |F(x, y)|^2 dx dy)^2}{\int \int |F(x, y)|^4 dx dy}. \quad (3.5)$$

The parameter  $A_{eff}$  is known as the effective core area. Depending on the sign of ( $K''\gamma$ ) two different type of solutions of NLS-equation (3.3) will be obtained. We will only consider the case of anomalous Group Velocity Dispersion, i.e.,  $K'' < 0$ , and assume that  $\gamma$  is positive (self-focusing). A normalized form of this equation can be obtained by introducing a frame of reference moving at the group velocity  $v_g = 1/K'$ ,

$$\tau = t - z/v_g = t - K'z, \quad (3.6)$$

and applying the following transformation:

$$Z = \frac{|K''|}{w_0^2} z, \quad T = \frac{\tau}{w_0}, \quad B = \sqrt{\frac{\gamma w_0^2}{|K''|}} A, \quad (3.7)$$

where  $w_0$  is a parameter that can be a measure of the width of the incident pulse. Then one obtains the standard form of the self-focusing NLS-equation

$$i \frac{\partial B}{\partial Z} + \frac{1}{2} \frac{\partial^2 B}{\partial T^2} + |B|^2 B = 0. \quad (3.8)$$

### 3.2.2 Spatial-NLS equation for beam propagation

To consider two-dimensional (2D) beam propagation in a third order nonlinear medium, we approximate for simplicity the squared refractive index by (see e.g. [11])

$$n^2 = n_0^2 + 2n_0 n_2 |\mathbf{E}|^2. \quad (3.9)$$

We further assume a 2D setting (the first and higher order derivatives of the field with respect to  $y$  are zero) such that the wave is polarized in the  $y$  direction and propagates in the  $z$  direction with  $\mathbf{E}$  given by

$$\mathbf{E} = \frac{1}{2} \left\{ A(z, x) e^{i(k_0 z - \omega_0 t)} + cc. \right\} \cdot \mathbf{y}, \quad (3.10)$$

where the wave number  $k_0$  is given by the linear dispersion relation  $k_0 = \omega_0 n_0 / c$ . The situation above corresponds to a planar waveguide, with interfaces parallel to the  $x - z$  plane for which the dimensionality has been reduced. By applying these assumptions together with the slowly varying envelope approximation (SVEA), the wave equation reduces to

$$2ik_0 \frac{\partial A}{\partial z} + \frac{\partial^2 A}{\partial x^2} + 2k_0^2 \frac{n_2}{n_0} |A|^2 A = 0. \quad (3.11)$$

To normalize this equation (3.11), we introduce

$$X = \frac{x}{w_0}; \quad Z = \frac{z}{k_0 w_0^2}; \quad B = k_0 w_0 \sqrt{n_2/n_0} A, \quad (3.12)$$

where  $w_0$  is the width of the input beam. Then the resulting equation is the same as the normalized NLS equation for pulse propagation (3.8) with  $T \equiv X$ :

$$i \frac{\partial B}{\partial Z} + \frac{1}{2} \frac{\partial^2 B}{\partial X^2} + |B|^2 B = 0. \quad (3.13)$$

### 3.2.3 Phase-amplitude equation for NLS equation

To study the deformation of wave groups, it is useful to formulate the phase-amplitude equation for the NLS-equation. Taking the form of the equation in physical variables, we only derive the phase-amplitude equations for the temporal-NLS since the phase-amplitude equation for the spatial-NLS can be derived similarly. Introducing the real amplitude  $a(z, t)$  and phase  $\varphi(z, t)$  for  $A(z, t)$

$$A(z, t) = a(z, t) e^{i\varphi(z, t)}, \quad (3.14)$$

the phase-amplitude equations can be obtained from (3.14) and (3.3):

$$\frac{\partial I}{\partial z} + \frac{\partial [(K' - K'' \partial_t \varphi) I]}{\partial t} = 0 \quad (3.15)$$

$$\frac{\partial \varphi}{\partial z} + K' \frac{\partial \varphi}{\partial t} - \frac{1}{2} K'' \left( \frac{\partial \varphi}{\partial t} \right)^2 + \frac{1}{2} K'' \frac{\partial_t^2 a}{a} - \gamma a^2 = 0, \quad (3.16)$$

where  $I = a^2$ . Writing  $\theta(z, t) = k_0 z - \omega_0 t + \varphi(z, t)$ , the wave number  $k(z, t)$  and frequency  $\omega(z, t)$  are defined by

$$k(z, t) = \frac{\partial \theta(z, t)}{\partial z} = k_0 + \frac{\partial \varphi(z, t)}{\partial z} \quad (3.17)$$

$$\omega(z, t) = -\frac{\partial \theta(z, t)}{\partial t} = \omega_0 - \frac{\partial \varphi(z, t)}{\partial t}. \quad (3.18)$$

Observe that the conservation law for the wave number  $\partial_t k + \partial_z \omega = 0$  is a kinematic consequence of these definitions. Approximating  $K(\omega) = K(\omega_0 - \varphi_t) \approx k_0 - K' \varphi_t + \frac{1}{2} K'' (\varphi_t)^2$  and  $1/V = K'(\omega) = K'(\omega_0 - \varphi_t) \approx K' - K'' \varphi_t$ , the phase-amplitude equation can be written in a more appealing way as

$$\frac{\partial I}{\partial z} + \frac{\partial [I/V]}{\partial t} = 0 \quad (3.19)$$

$$k - K(\omega) = \gamma I - \frac{1}{2} K'' \frac{\partial_t^2 a}{a}. \quad (3.20)$$

Equation (3.19) is the energy equation expressing that the intensity is translated approximately with the group velocity  $V = 1/K'$ . Equation (3.20) is the *nonlinear dispersion relation* (NDR); the right hand side of the NDR is an extension of the linear dispersion relation which is given by  $k - K(\omega) = 0$ . The right hand side contains the effect of nonlinearity ( $\gamma I$ ) and an effect from GVD that is independent of the peak intensity of the pulse; this last term is known as the Whitham-Forenberg contribution, see [13]. The energy equation and the NDR form a closed system of nonlinear equations.

### 3.3 Numerical results

In this section we study the deformation of bichromatic wave groups numerically. The phase-amplitude equations (3.19)-(3.20) are not well-suited for numerical calculations, as will become clear from the following. Instead, we will solve the normalized NLS-equation (3.8) using an implicit Crank-Nicolson method [5].

The calculations are performed for pulses that are initially bichromatic, i.e. a wave group which is a superposition of two monochromatic waves, described in linear theory by

$$\begin{aligned} E(z, t) &= q_a \{ \exp [i (k_1 z - \omega_1 t + \pi/2)] + \exp [i (k_2 z - \omega_2 t - \pi/2)] \} \\ &= -2q_a \sin \left( \Delta k \left( z - \frac{\Delta \omega}{\Delta k} t \right) \right) \exp [i (\bar{k} z - \bar{\omega} t)] \end{aligned} \quad (3.21)$$

where  $\bar{k}$  and  $\bar{\omega}$  are respectively the averaged wave number and frequency:  $k_{1,2} = \bar{k} \pm \Delta k$ ,  $\omega_{1,2} = \bar{\omega} \pm \Delta \omega$ ; see Figure 3.1 for a typical pattern of the bichromatic wave group. Expression (3.21) shows the carrier wave, modulated with envelope of wave length  $2\pi/\Delta \omega$  that propagates with group velocity  $\Delta \omega/\Delta k$  at the averaged wave number.

Since we want to study the deformation of an initially bichromatic wave pulse via the NLS equation, we should consider a sinusoidal wave envelope as the initial condition:

$$A(z = 0, t) = \tilde{q} \sin (\Delta \omega t) \quad (3.22)$$

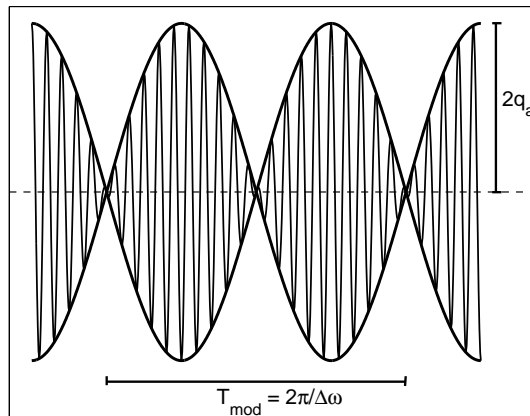


Figure 3.1: Typical linear interference of the bichromatic wave (beats).

where  $\tilde{q} = -2q_a$  (we assume that  $\tilde{q}$  is positive). By defining that the width of the initial wave equals to the half of the modulation period,  $w_0 = \pi/\Delta\omega$ , the initial condition (3.22) is normalized to

$$B(Z = 0, T) = q_b \sin(\pi T), \quad (3.23)$$

where  $q_b = (\tilde{q}/\Delta\omega) \sqrt{\gamma\pi^2/|K''|}$ ; showing that the normalized amplitude of the initial wave envelope is proportional to the quotient of the actual amplitude and the physical frequency difference. Using the initial condition (3.23), we perform numerical experiments based on the normalized NLS equation (3.8) with periodic boundary conditions in one modulation period  $T_{mod} = 2\pi/\Delta\omega$ . We show typical results of the numerical computation in Figures 3.2 - 3.6. Depending on the value of  $q_b$ , the envelope of the bichromatic wave group remains almost unchanged (for small value of  $q_b$ ) or deforms gradually (for larger value of  $q_b$ ). For large value of  $q_b$ , the envelope shows large deformations; the peak value may become more than twice the initial amplitude, and the peak may split into two or more peaks after longer propagation distances, as seen in Figure 3.6.

Besides the deformation of the envelope, we also present the changes of wave number and frequency from the numerical results in a so-called dispersion trajectory, parameterized by time in half of the modulation period. For a 'stable' envelope, the changes of wave number and frequency appear to be small. However, whenever the envelope experiences large deformation, the changes of wave number and frequency are also very large, especially at positions where the envelope changes quickly near zero (see Figure 3.6). These large variations can be understood from the NDR (3.20), i.e. the quotient  $\partial_t^2 a/a$  becomes very large at the point where amplitude  $a$  is vanishing. The large deviations shown in the dispersion trajectory are also characteristic for the comparable case of bi-soliton interaction; see [8].



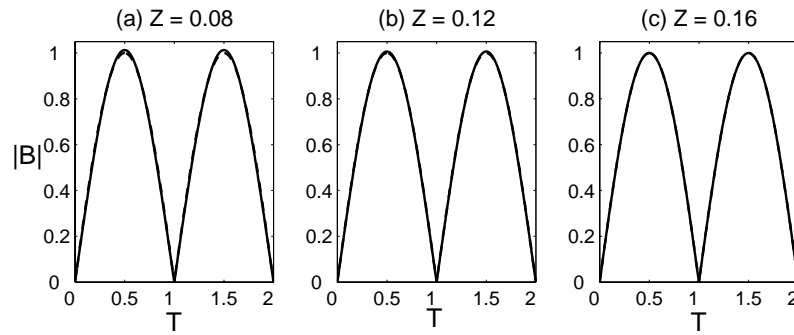


Figure 3.2: Amplitude  $|B|$  for  $q_b = 1$  at different positions. The dashed-line (which in this case almost coincides with the full line) represents the initial value). The first largest deformation is plotted in (a), showing that the change of the envelope is very small. Figure (c) shows the envelope 'back' to the initial envelope. In Figure (b) we plot the envelope after the largest deformation but before it returns to the initial envelope.

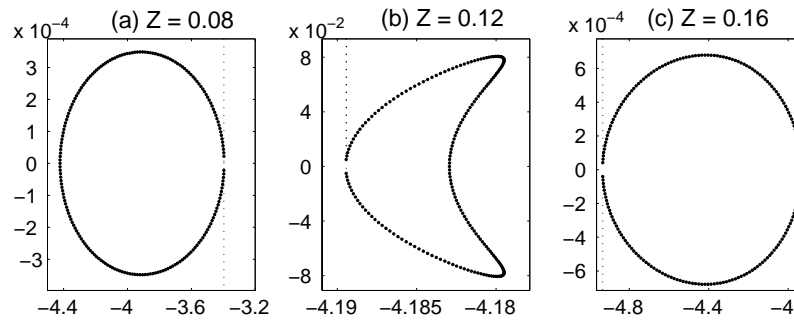


Figure 3.3: The dispersion trajectory that corresponds to Figure 3.2 parameterized by  $T$ ; only half of the modulation period is plotted. The horizontal and vertical axis are respectively the change of wave number ( $\partial\varphi/\partial Z$ ) and the change of frequency ( $-\partial\varphi/\partial T$ ), cf. Equation (3.17) and Equation (3.18). Observe that the changes of wave number and frequency are small.

We notice that the appearance of such large variations in amplitude and phase may conflict with the basic assumption used in the derivation of the NLS equation, i.e. the envelope varies slowly. The large and rapid changes in phase also explain why the phase-amplitude equations cannot be solved numerically in an easy way.

An interesting result is that during the evolution the pulse may deform into a train of soliton-like pulses. To show this, in Figure 3.7 we plot the NLS-solution for  $q_b = 5$

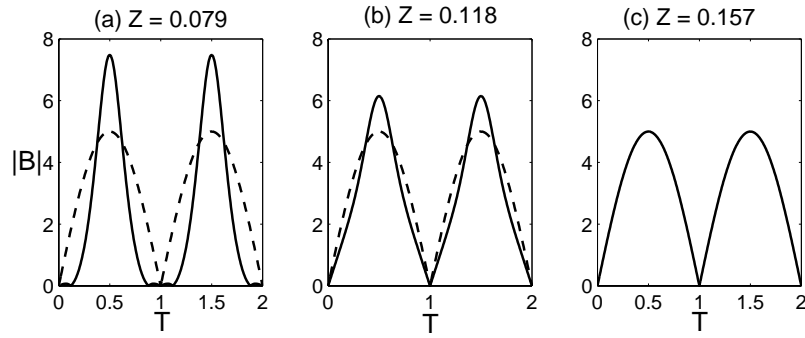


Figure 3.4: Same for Figure 3.2 but for  $q_b = 5$ . Observe that the envelope deformation for this case is larger than that for  $q_b = 1$ . It is clearly seen that during the evolution, the envelope increases in the middle and decrease at the flanks, and then back to the initial envelope.

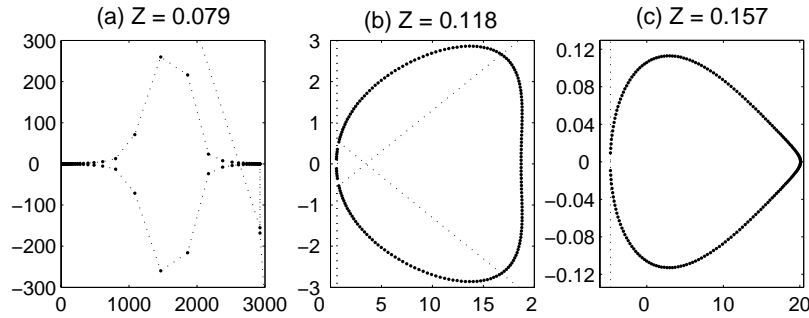


Figure 3.5: Same for Figure 3.3 but for  $q_b = 5$ . Observe that the changes in the wave number and frequency are much larger than for the case  $q_b = 1$ , especially at the position where the largest deformation occurs ( $Z = 0.079$ ).

at position where the envelope of pulse resembles a soliton-like train and compare it with a linear superposition of solitons:

$$S = \left| \sum_{m=1}^4 (-1)^m C \operatorname{sech}(C(T - m + 1.5)) \right|,$$

with  $C$  taken from the maximum amplitude of the calculated solution. It is found that at that position the numerical NLS-solution nearly corresponds to a soliton train. However, unlike a single soliton that propagates on the whole real line, the soliton train that is formed from the bichromatic pulse (beam) deforms because of mutual interaction and periodicity.

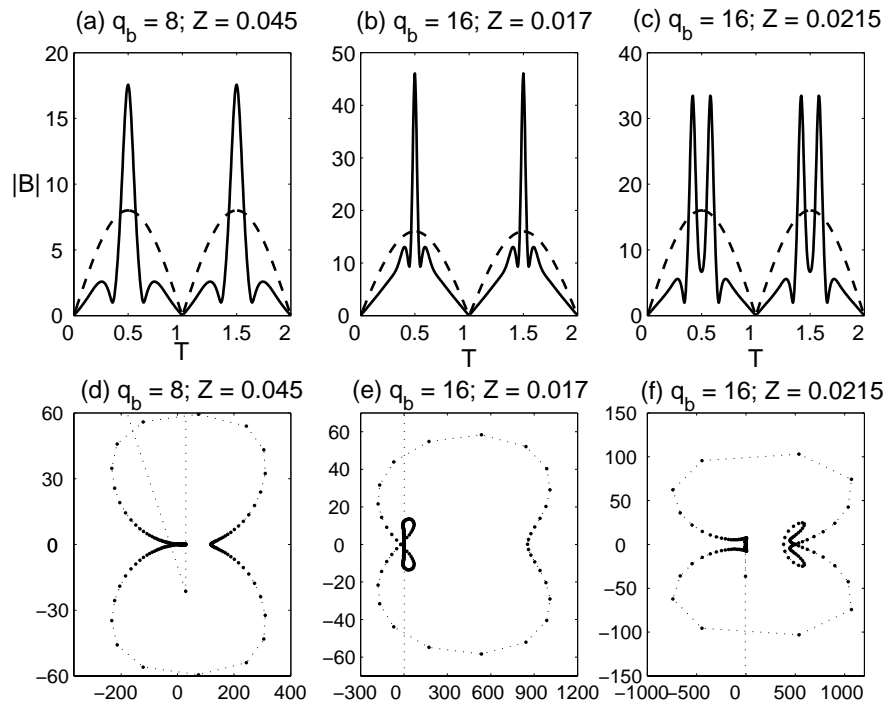


Figure 3.6: The field envelope and the corresponding dispersion trajectory for  $q_b = 8$  and  $q_b = 16$  at positions where the envelope looks like that of higher-order solitons. Observe the very large variations in both envelope and wave number (frequency).

### 3.4 Analytical description of the deformation

From the numerical results we see that for relatively small amplitude ( $q_b$ ) the envelope of the bichromatic wave group hardly changes, but that for larger amplitudes, the variations of the envelope becomes much larger. We will now present two independent arguments that support the statement that large changes, 'instability', appear when a critical value of a characteristic parameter is exceeded. The envelope change during the initial stages of the deformation will also be explained using the phase-amplitude equations.

#### 3.4.1 Instability condition based on NDR

A first argument is found from an investigation of the NDR. We first look at 'steady state solutions' that correspond to solutions for which

$$\nu = k - K(\omega) \equiv \text{constant}.$$

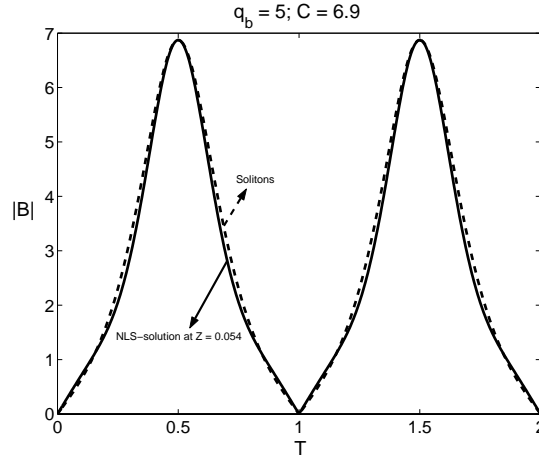


Figure 3.7: Soliton-train formation from bichromatic pulse (beam) with  $q_b = 5$ : shown is the pulse amplitude and the profile of a linear superposition of NLS-solitons.

Then the NDR (3.20) can be considered as Newton's equation of motion for a particle with mass  $-\frac{1}{2}K''$  under the influence of potential energy

$$Pot = \frac{1}{4}\gamma a^4 - \frac{1}{2}\nu a^2. \quad (3.24)$$

Typical plots of this potential function shown in Figure 3.8 show that, for  $\nu \leq 0$ , all solutions are always periodic and symmetric around  $a = 0$ . On the other hand, if  $\nu > 0$  various types of solutions can exist:

- (i) a soliton solution with amplitude  $\sqrt{2\nu/\gamma}$ ;
- (ii) constant solution, i.e.,  $a = \sqrt{\nu/\gamma}$ ;
- (iii) small periodic solution around  $a = \sqrt{\nu/\gamma}$ ;
- (iv) larger periodic solution and symmetric around  $a = 0$ .

In the actual evolution, the value of  $\nu$  is not constant but varies in time and space,  $\nu = \nu(z, t)$ , according to equation (3.20); hence NDR can be viewed as above with a continuously changing potential function. As long as  $\nu$  remains negative, the potential remains convex, and relatively small changes will occur. The envelope changes are stronger when  $\nu$  becomes positive. For the case under consideration, i.e. a wave that is initially bichromatic,  $a(z = 0, t) = \tilde{q} \sin(\Delta\omega t)$ , the initial value of  $\nu$  is given by

$$\nu(z = 0, t) = \gamma\tilde{q}^2 \sin^2(\Delta\omega t) + \frac{1}{2}K''(\Delta\omega)^2.$$

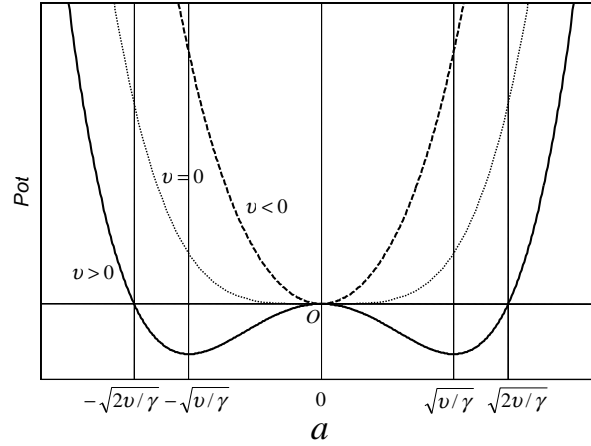


Figure 3.8: Typical plot of the potential energy as a function of  $a$  for different sign of  $\nu$ .

Then, initially, the value of  $\nu$  assumes positive values when the following 'instability condition' is satisfied:

$$\frac{\tilde{q}}{\Delta\omega} > \sqrt{-\frac{1}{2} \frac{K''}{\gamma}}; \quad (3.25)$$

in normalized variables this reads

$$q_b > \sqrt{\pi^2/2}. \quad (3.26)$$

This indicates that instability is determined by the quotient of the amplitude and the frequency difference:  $\tilde{q}/\Delta\omega$ . This means that instability can be expected for large amplitudes or small frequency differences.

### 3.4.2 Instability condition based on energy argument

An alternative derivation of the instability condition is based on the well-known property that for the self-focusing NLS equation, when the transversal coordinate is considered to be infinite, any initial data deforms into solitons and residual radiation. For a soliton to exist, it is found in the previous subsection that  $\nu = k - K(\omega)$  is necessarily positive. However, for the bichromatic case, the profiles are periodic with the modulation period  $T_{mod} = 2\pi/\Delta\omega$ . Since the width of a soliton is inversely proportional to its amplitude, the requirement that a soliton can be formed within half of the modulation period, requires the amplitude to be sufficiently large, leading to a comparable result as above in the following way.

The energy in half of the modulation period is

$$\mathcal{E} = \int_0^{\pi/\Delta\omega} \tilde{q}^2 \sin^2(\Delta\omega t) dt = \frac{1}{2} \tilde{q}^2 \pi / \Delta\omega. \quad (3.27)$$

For a soliton  $S(t)$  with amplitude  $C$ :

$$S(t) = C \operatorname{sech} \left( C \sqrt{-\frac{\gamma}{K''}} t \right), \quad (3.28)$$

the energy of this soliton is

$$\mathcal{E}_{sol} = \int S^2(t) dt = 2C \sqrt{-K''/\gamma}, \quad (3.29)$$

which is inversely proportional to the soliton width. Hence, in order that a soliton can exist within half of the modulation period, the width of the soliton must be 'practically' (neglecting exponential tails) sufficiently smaller than the modulation period, i.e.

$$C \sqrt{\frac{\gamma}{-K''}} > \alpha \Delta \omega \quad (3.30)$$

for some  $\alpha$ . If we compare the generated energy with the soliton energy, and consider the restriction of the soliton width,  $\frac{1}{2} \tilde{q}^2 \pi / \Delta \omega \sim 2C \sqrt{-K''/\gamma} > -2\alpha \Delta \omega K''/\gamma$ , the following condition must be satisfied to obtain at least one soliton within half of the modulation period:

$$\frac{\tilde{q}}{\Delta \omega} > \sqrt{\frac{4\alpha}{\pi}} \sqrt{-\frac{K''}{\gamma}}, \quad (3.31)$$

for  $\alpha = \pi/8$  the same result is obtained as in the previous subsection.

### 3.4.3 Deformation of the initial shape

Using the full set of phase-amplitude equations, it is possible to investigate the tendency of the change of the envelope profile during the initial stages, in the following way. At the initial position where the bichromatic pulse is generated, the amplitude is  $a = \tilde{q} \sin(\Delta \omega t)$  and the frequency of the carrier wave is  $\omega = \omega_0$ . From the NDR we obtain the wave number  $k = k_0 + \gamma \tilde{q}^2 \sin^2(\Delta \omega t)$ . Then the change of frequency for the next position  $\Delta z$  can be determined from the conservation of wave number; with this information, the energy at  $\Delta z$  follows from the energy equation. As a result, the envelope of a pulse (beam) that is initially sinusoidal in each modulation period, increases in the middle and decreases at the flanks. This process is illustrated in Figure 3.9. The change of initial energy (amplitude) in Figure 3.9.(c), indicates that the modulated envelope will deform with a higher peak in the middle and lower values in the flanks. This profile will further deform at longer propagation distances, which can be calculated in a successive way.

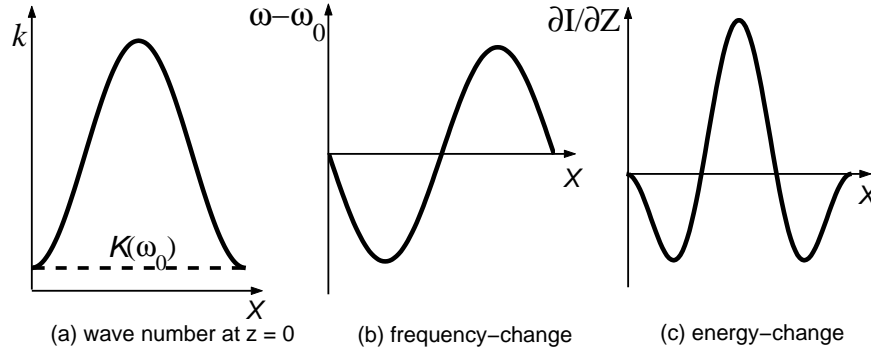


Figure 3.9: Initial deformation

## 3.5 Low dimensional model

### 3.5.1 Model formulation

Apart from studying the bichromatic wave deformation based on the full NLS equation (3.8), we will also derive a low dimensional model to simulate the deformation. To that end, we consider first the functional of the normalized NLS equation (3.8) which is given by

$$\mathcal{L}_0 = \int \int \frac{i}{2} \text{Im} \left( \frac{\partial B}{\partial Z} B^* \right) - \frac{1}{4} \left| \frac{\partial B}{\partial T} \right|^2 + \frac{1}{4} |B|^4 \, dZ \, dT, \quad (3.32)$$

where  $\text{Im}(u)$  and  $u^*$  stand for the imaginary part and the complex conjugate of  $u$ , respectively. It can be checked that the NLS equation (3.8) is the Euler-Lagrange equation for the functional  $\mathcal{L}_0$ , cf.  $\delta_B \mathcal{L}_0 = 0$ . This equation can also be written as a Hamilton's equation

$$i \frac{\partial B}{\partial Z} = \delta_B \mathcal{H}_0, \quad (3.33)$$

with Hamiltonian

$$\mathcal{H}_0 = \int \frac{1}{4} \left| \frac{\partial B}{\partial T} \right|^2 - \frac{1}{4} |B|^4 \, dT. \quad (3.34)$$

As is well known, the NLS equation has an infinite number of conserved quantities. The first conserved quantity is the energy (or power)

$$Q = \int_{-\infty}^{\infty} |B|^2 \, dT. \quad (3.35)$$

Then, motivated by the cubic nonlinearity in the NLS equation and the change in the deformation of the envelope as mentioned in the previous section, we consider

a four-dimensional (4D) manifold  $\mathcal{M}$  of the complex coefficients in front of the two most dominant harmonic temporal modulations:

$$\mathcal{M} = \left\{ B = q(Z) \sin\left(\frac{\pi T}{T_M}\right) + p(Z) \sin\left(\frac{3\pi T}{T_M}\right) \mid q, p \in \mathbb{C} \right\}. \quad (3.36)$$

By applying this manifold, the functional (3.32) leads to

$$\begin{aligned} \mathcal{L}_1 = & \int \frac{i}{2} \text{Im}(q_Z q^* + p_Z p^*) - \frac{1}{4} \frac{\pi^2}{T_M^2} (|q|^2 + 9|p|^2) + \frac{1}{16} [3|q|^4 + 3|p|^4] \\ & + \frac{1}{16} [8|q|^2|p|^2 + 2(q^2(p^*)^2 + p^2(q^*)^2) - 2|q|^2(qp^* + pq^*)] dZ. \end{aligned} \quad (3.37)$$

Then the Euler-Lagrange equation of the functional  $\mathcal{L}_1$  is a Hamilton's equation:

$$iq_Z = \delta_q \mathcal{H}_1(q, p) \quad (3.38)$$

$$ip_Z = \delta_p \mathcal{H}_1(q, p), \quad (3.39)$$

with Hamiltonian

$$\begin{aligned} \mathcal{H}_1(q, p) = & \frac{1}{4} \frac{\pi^2}{T_M^2} (|q|^2 + 9|p|^2) - \frac{1}{16} [3|q|^4 + 3|p|^4] \\ & - \frac{1}{16} [8|q|^2|p|^2 + 2(q^2(p^*)^2 + p^2(q^*)^2) - 2|q|^2(qp^* + pq^*)]. \end{aligned} \quad (3.40)$$

This is a nonlinear system of two ordinary complex differential equations. To reduce the dimensionality of the system, we first introduce the real amplitudes  $\rho_1(Z)$ ,  $\rho_2(Z)$  and phase  $\varphi_1(Z)$  and  $\varphi_2(Z)$  for  $q(Z)$  and  $p(Z)$

$$q = \rho_1 e^{i\varphi_1}, \quad p = \rho_2 e^{i\varphi_2}, \quad (3.41)$$

and define  $\psi = -\varphi_1 + \varphi_2$ . Then, it can be shown that

$$\rho_1^2 + \rho_2^2 \equiv \text{const} = \mathcal{E} \quad (\text{necessarily } > 0), \quad (3.42)$$

which is consistent with energy conservation law (3.35). By introducing  $\rho_1^2 = G \geq 0$  we obtain  $\rho_2^2 = \mathcal{E} - G$  with necessarily  $G \leq \mathcal{E}$ . For a given  $\mathcal{E}$ , the functional  $\mathcal{L}_1$  and the Hamiltonian  $\mathcal{H}_1$  reduce to

$$\mathcal{L}_2 = \int [\psi_Z G - \mathcal{H}_2(G, \psi; \mathcal{E}) dZ], \quad (3.43)$$

$$\begin{aligned} \mathcal{H}_2 = & \frac{1}{2} \frac{\pi^2}{T_M^2} (-8G + 9\mathcal{E}) \\ & - \frac{1}{8} [3\mathcal{E}^2 + 2G(\mathcal{E} - G)(1 + 2\cos(2\psi)) - 4G\sqrt{G(\mathcal{E} - G)}\cos(\psi)], \end{aligned} \quad (3.44)$$

with the Hamilton's equation is given by

$$\psi_Z = \partial_G \mathcal{H}_2(G, \psi; \mathcal{E}) \quad (3.45)$$

$$G_Z = -\partial_\psi \mathcal{H}_2(G, \psi; \mathcal{E}). \quad (3.46)$$

Thus, the class of solutions determined by (3.36) is a two-parameter family of the NLS solutions, and it can be found by solving (3.45) and (3.46). For the rest of this section, without loss of generality, we assume that  $T_M = 1$ .



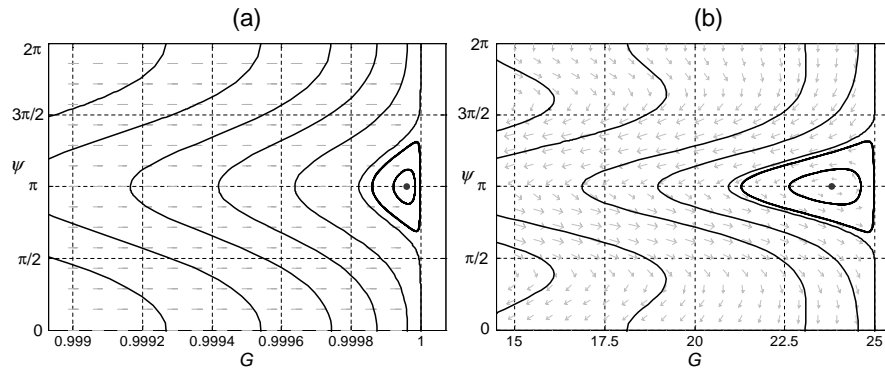


Figure 3.10: Phase-portrait of the reduced Hamiltonian system for (a)  $\mathcal{E} = 1$  and (b)  $\mathcal{E} = 25$ .

### 3.5.2 Dynamics of the model

In this section we present a qualitative analysis of the Hamiltonian system (3.45) and (3.46). The qualitative behavior of the solutions of (3.45) and (3.46) are represented by trajectories in the phase-plane  $(G, \psi)$  as in Figure 3.10.(a) and 3.10.(b), for  $\mathcal{E} = 1$  and  $\mathcal{E} = 25$  respectively. This phase-plane represents the constant level lines of Hamiltonian  $\mathcal{H}_2$  on cylinder  $\mathcal{E}$ . According to Equation (3.41), the phase difference  $\psi$  is  $2\pi$ -periodic and therefore each trajectory in this picture can be considered as a closed orbit.

When considering an initial value problem with initial condition (3.23), the amplitude  $q_b = 1$  and  $q_b = 5$  correspond to respectively  $(G = 1, \psi = 0)$  in Figure 3.10.(a) and  $(G = 25, \psi = 0)$  in Figure 3.10.(b). From Figure 3.10, it is clear that during the evolution, parts of the energy of the first mode is transferred to create the second mode. When the phase difference  $\psi = \pi$ , parts of the energy of the second mode is transferred back to the first mode until the second mode disappear. In other words, there is a periodic energy exchange between the first and the second mode. The energy exchange is larger for the larger  $\mathcal{E}$ . Specifically, when  $q_b = 1$  the energy exchange is very small; meaning that the envelope will experience very small deformation during the evolution.

The dot-point in Figure 3.10.(a) and (b) represents the equilibrium of system (3.45) and (3.46). As can be seen this equilibrium is surrounded by closed orbits, showing that it is a stable equilibrium. Considering (3.41) and (3.42), the equilibrium solution  $(G_{crit}, \psi_{crit})$  is given by  $\psi_{crit} = \pi$  with  $G_{crit}$  is the positive real root of a cubic polynomial

$$52G^3 - (96\mathcal{E} + 192\pi^2)G^2 + (288\pi^2\mathcal{E} + 54\mathcal{E}^2 + 256\pi^4)G - (256\pi^4\mathcal{E} + 96\pi^2\mathcal{E}^2 + 9\mathcal{E}^3) = 0. \quad (3.47)$$

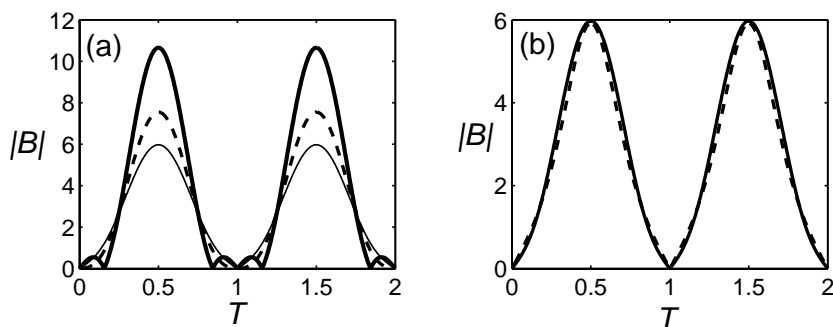


Figure 3.11: (a) Equilibrium solution of the low dimensional model for  $\mathcal{E} = 25$  (thin-solid-line),  $\mathcal{E} = 36$  (dashed-line) and  $\mathcal{E} = 64$  (bold-solid-line). (b) Comparison between the equilibrium solution for  $\mathcal{E} = 25$  (solid-line) and the linear superposition of out of phase solitons (dashed-line).

We plot the equilibrium solution for different values of  $\mathcal{E}$  in Figure 3.11.(a). Those equilibria can be understood as a projection of soliton solution of the NLS equation (3.3) on the manifold  $\mathcal{M}$ . Remark that the soliton solution of the NLS equation in fact is a solution of the constrained critical problem  $Min \{ \mathcal{H}_0(B) | Q(B) = \mathcal{E} \}$ . In the derivation of the Hamiltonian system (3.45) and (3.46), we have included the constrained  $Q(B) = \mathcal{E}$  as we see in (3.42). In Figure 3.11.(b) we also compare the equilibrium solution for  $\mathcal{E} = 25$  with the linear superposition of solitons with phase difference  $\pi$  (out of phase solitons) where the amplitude of the soliton is taken from the maximum amplitude of the equilibrium solution. It is found that they are indeed in a very good agreement.

### 3.5.3 Envelope deformation

In order to verify the qualitative behavior of the reduced Hamiltonian system (3.45) and (3.46), we solve the Hamilton's equation (3.38) and (3.39) using Fehlberg fourth-fifth order Runge-Kutta method. We take a sinusoidal envelope (3.23) with  $\Delta\omega = \pi$  as initial condition for different amplitudes  $q_b$  such that

$$q(0) = q_b; p(0) = 0. \quad (3.48)$$

Typical results of the numerical solution are shown in Figure 3.12. In these pictures, the amplitudes evolution of the first and second modes, i.e.  $q(z)$  and  $p(z)$  are plotted in the complex plane. It can be seen that the amplitudes of these two modes show a periodic behavior while the phase changes regularly. The appearance of the second mode depends very much on the initial amplitude  $q_b$ . For relatively small amplitudes, along the evolution, the amplitude  $q(z)$  is almost the same and the maximum of

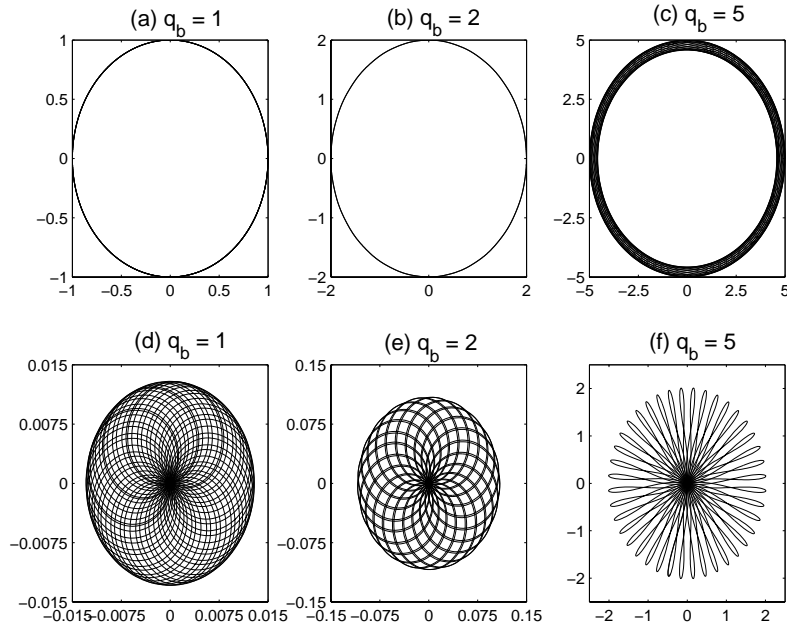


Figure 3.12: Dynamic of  $q(z)$  (Figures (a)-(c)) and  $p(z)$  (Figures (d)-(f)) in the complex plane for different values of  $q_b$ . The  $x$ -axis and  $y$ -axis represent the real and the imaginary part of the plotted function. Observe the (quasi-)periodicity of  $|q(z)|$  and  $|p(z)|$  and the changes in phase.

the amplitude  $p(z)$  is very small. As a result, the envelope of the bichromatic wave will approximately be the same during propagation. On the other hand, for larger values of  $q_b$ ,  $|q(z)|$  will decrease and then increase periodically with  $\max\{|q(z)|\} = q_b$ . This phenomenon corresponds to the large deformation of the envelope of bichromatic waves (see Figure 3.13). For example, the maximum values of  $p(z)$  are approximately 1% and 5% from the initial amplitudes for  $q_b = 1$  and  $q_b = 2$ , respectively; and around 40% for  $q_b = 5$ . Moreover, this phenomenon also explains the spatial instability of the bichromatic wave that was observed in the numerical solution of the NLS equation presented in section 3.3. We remark that these numerical results also agree with the results of the qualitative analysis presented in section 3.5.2.

By obtaining the solution of the Hamilton's equation (3.38) and (3.39), we can calculate the complete solution of the NLS equation on  $\mathcal{M}$  using Equation (3.36). The results for  $q_b = 5$  are presented in Figure 3.13. It is shown that the bichromatic waves envelope experiences large deformation. The results of the low dimensional model is also compared with the numerical solution of the NLS equation. We found that the low dimensional model can describe the qualitative deformation reasonably well. Indeed, the solutions of the low dimensional model are in a good agreement

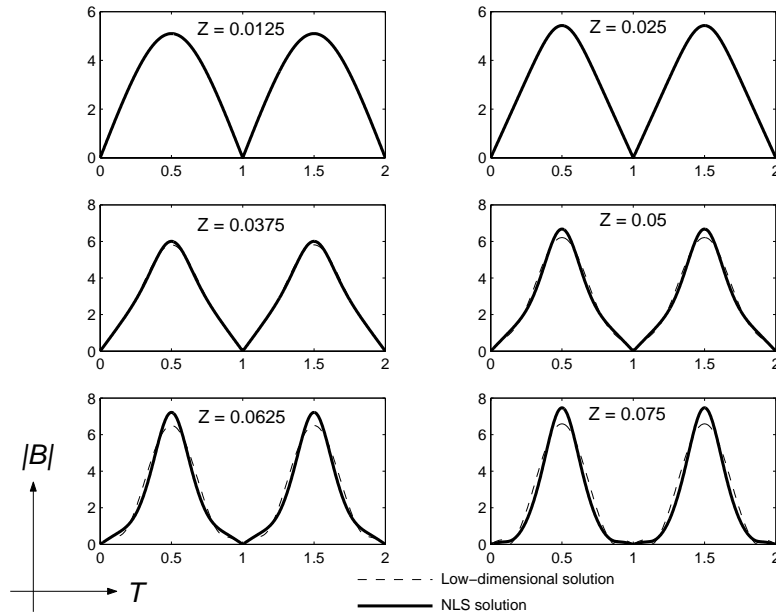


Figure 3.13: Envelope evolution for  $q_b = 5$  at different positions. Observe that the envelope experience relatively large deformation during the evolution. At positions that are relatively not far from the initial position, the low dimensional model gives correct quantitative description.

with solutions of the NLS equation, at least until at position that is not too far from the initial position. At larger distances we can see the deviation between the low dimensional solution and the NLS solution; showing the appearance of higher order modes. Therefore, for an adequate description, the low dimensional model would need improvement, i.e. by taking higher order modes on the manifold  $\mathcal{M}$ , see Equation (3.36).

### 3.6 Concluding remarks

In this chapter, the strong deformation of a modulated wave group in third-order nonlinear media has been investigated numerically and analytically. The numerical simulations of the NLS equation show that an optical pulse that is initially bichromatic can deform substantially with large variation in amplitude and phase. For specific cases, the bichromatic wave can deform into a train of soliton-like waves. Using either the coupled phase-amplitude equation or the energy argument, the appearance of large deformation has been shown to depend on exceeding a critical value of the quotient of

amplitude and frequency difference ( $\tilde{q}/\Delta\omega$ ). We remark that such dependence in the case of a bichromatic pulse in second-order nonlinear media has also been confirmed by van Groesen *et al.* [9]. Although the discussion in this chapter is focused on bichromatic pulses, the results hold equally well for the spatial analog.

To study the bichromatic wave deformation, we have also derived a low dimensional model by considering only the two most dominant harmonic temporal modulations. It is shown that this model describes the correct qualitative deformation. Furthermore, as long as higher frequency modulations are negligible, which is the case for moderate values of the energy, the description of the low dimensional model is also quantitatively correct.

Finally we remark that the appearance of large amplitude variations for relatively large  $\tilde{q}/\Delta\omega$  may conflict with the basic assumption of the NLS equation, namely that the envelope varies slowly. Therefore, the validity of the NLS equation in this case is questionable.

## References

- [1] Agrawal, G.P., *Nonlinear fiber optics*, (Academic Press, Inc., San Diego, CA, 3<sup>rd</sup> ed., 1995).
- [2] N.N. Akhmediev and A. Ankiewicz, *Solitons: Nonlinear pulses and beams*, (Chapman & Hall, London, 1997).
- [3] T.B. Benjamin and J.F. Feir, The disintegration of wave trains on deep water, *J. Fluid Mech.* **27**, p. 417, 1967.
- [4] C. Cambournac, H. Maillotte, E. Lantz, J.M. Dudley and M. Chauvet, Spatiotemporal behavior of periodic arrays of spatial solitons in a planar waveguide with relaxing Kerr nonlinearity, *J. Opt. Soc. Am.* **B19**, p. 574, 2002.
- [5] Q.S. Chang, E.H. Jia and W. Sun, Difference schemes for solving the generalized nonlinear Schrödinger equation, *J. Comput. Phys.* **148**, p. 397, 1999.
- [6] L. Friedrich, G.I. Stegeman, P. Millar and J.S. Aitchison,  $1 \times 4$  optical interconnect using electronically controlled angle steering of spatial solitons, *IEEE Photon. Tech. Lett.* **11**, p. 988, 1999.
- [7] J. Garnier and F.K. Abdullaev, Modulational instability induced by randomly varying coefficients for the nonlinear Schrödinger equation, *Physica* **D145**, p. 65, 2000.
- [8] E. van Groesen, T. Nusantara and E. Soewono, Large variations in NLS bi-soliton wave groups, *Opt. Quant. Electron.* **33**, p. 499, 2001.

- [9] E. van Groesen, E. Cahyono and A. Suryanto, Uni-directional models for narrow- and broad-band pulse propagation in second-order nonlinear media, *Opt. Quant. Electron.* **34**, p. 577, 2002.
- [10] A. Hasegawa, Generation of a train of soliton pulses by induced modulational instability in optical fibers, *Opt. Lett.* **9**, p.288, 1984.
- [11] A. Hasegawa and Y. Kodama, *Solitons in optical communications*, (Clarendon Press, Oxford, 1995).
- [12] A. Hasegawa and M. Matsumoto, *Optical solitons in fibers*, (Springer-Verlag, Berlin, 2003).
- [13] E. Infeld and G. Rowlands, *Nonlinear waves, solitons, and chaos*, (Cambridge Univ. Press, Cambridge, 1990).
- [14] D. Kip, M. Soljacic, M. Segev, E. Eugenieva and D.N. Christodoulides, Modulation instability and pattern formation in spatially incoherent light beams, *Science* **290**, p. 495, 2000.
- [15] A.C. Newell and J.V. Moloney, *Nonlinear optics*, (Addison-Wesley Publishing Company, California, 1992)
- [16] R. Malendevich, L. Jankovic, G.I. Stegeman and Aitchison JS, Spatial modulation instability in a Kerr slab waveguide, *Opt. Lett.* **26**, p. 1879, 2001.
- [17] M.J. Potasek and G.P. Agrawal, Self-amplitude modulation of optical pulses in nonlinear dispersive fibers, *Phys. Rev.* **A36**, p. 3862, 1987.
- [18] K. Tai, A. Hasegawa, and A. Tomita, Observation of modulational instability in optical fibers, *Phys. Rev. Lett.* **56**, p. 1358, 1986.
- [19] K. Tai, A. Tomita, J. L. Jewell, and A. Hasegawa , Generation of subpicosecond solitonlike optical pulses at 0.3 THz repetition rate by induced modulational instability, *Appl. Phys. Lett.* **49**, p. 236, 1986.

## Chapter 4

# Propagation of spatial solitons in inhomogeneous media with Kerr nonlinearity: Paraxial approximation

### 4.1 Introduction

The study of nonlinear effects on propagation of electromagnetic waves in self focusing Kerr media has been of considerable recent interest. One of the widely studied nonlinear phenomena is the propagation of spatial solitons. In a Kerr medium, which possesses a positive intensity-dependent change of refraction index, the index increases with the light intensity. A beam of light can form a dielectric waveguide for itself, in which the refractive index is greater at the center of the beam than at its wings. Since the light beam in this self-formed dielectric waveguide can propagate without spreading, the phenomenon of "self-trapping" of an optical beam was thereby predicted to occur. One may also understand this phenomenon as a dynamic balancing of two opposing tendencies, namely, the tendency for the beam to expand due to diffraction, and the tendency for the beam to contract due to self-focusing; see e.g. [10]. This kind of dynamic balancing in (1+1)-dimensional (here the first "1" stands for the number of dimensions in which a beam spreads, and the second "1" for the propagation coordinate) is stable against all perturbations as was shown by Zakharov and Shabat [26], and therefore forms a genuine spatial soliton. Spatial solitons are not only predicted theoretically [9] but they have also been observed experimentally [3], [4], [5] and [11]. Some possible applications of spatial solitons such as optical

pulse compression [19], all optical switching [2], [23] and [22], logic devices [6], [27] and [18], etc. have been proposed. To explore all possible applications, it is extremely important to understand the generic properties of spatial solitons.

Interesting propagation properties of spatial solitons due to interface between two nonlinear media have been found by Aceves et. al. [1]. They reported that under certain conditions, a spatial soliton propagating at an oblique angle of incidence with respect to an interface between two positive uniform Kerr media can be transmitted, reflected or trapped by the interface, depending on intensity. Using equivalent-particle theory the authors derived an equation of motion for the average location of the soliton. The equivalent-particle theory has also been combined with the results developed in [21] to account for the breakup of an incident optical beam into multiple solitons when it crosses the interface [2]. Recently, Scheuer and Orenstein [22] derived a 2-particle theory to study the interactions of two solitons in the vicinity of the interface of two nonlinear media.

Recently another interesting property of solitons in a waveguide with transverse Gaussian linear refractive index profile is reported in [13]. The numerical results using FD-BPM presented in this reference show that a soliton oscillates inside such a waveguide. In this chapter we propose a model to describe this oscillatory behavior by starting with a small perturbation of the constant linear refractive index. In section 4.2 we derive the beam propagation equation in Kerr media. We obtain the standard Nonlinear Schrödinger (NLS) equation for uniform media and the modified-NLS for non-uniform media. In section 4.3 we show analytically, using an equivalent-particle approach, and numerically that this model produces correct propagation properties: the soliton beam oscillates inside the waveguide. In section 4.4 we extend the theory to study the breakup of a bound  $N$ -soliton, i.e.  $N$  solitons that travels together with the same velocity, into  $N$  independent solitons. Conclusions and remarks will be given in the last section.

## 4.2 Beam propagation in Kerr media

### 4.2.1 NLS equation for uniform media

The propagation of the electric field through two-dimensional, dispersionless and lossless media with Kerr nonlinearity is governed by the wave equation following from the Maxwell's equation

$$\nabla^2 \mathbf{E} - \mu_0 \frac{\partial^2}{\partial t^2} \mathbf{D} = \nabla (\nabla \cdot \mathbf{E}), \quad (4.1)$$

where

$$\begin{aligned} \mathbf{D} &= \varepsilon_0 \left( 1 + \chi^{(1)} + \chi^{(3)} |E|^2 \right) \mathbf{E} \\ &= \varepsilon_0 \left( n_0^2 + \chi^{(3)} |E|^2 \right) \mathbf{E}. \end{aligned} \quad (4.2)$$



is the displacement vector of the dielectric medium,  $n_0$  is the linear refractive index constant and  $\chi^{(3)}$  is the third-order nonlinear susceptibility. If we restrict the analysis to the transverse electric (TE) polarized waves and that the wave is stationary in time, then Equation (4.1) reduces to

$$\nabla^2 \mathbf{E} + \frac{\omega^2}{c^2} \left( n_0^2 + 2n_0 n_2 |E|^2 \right) \mathbf{E} = 0, \quad (4.3)$$

where  $c = 1/\sqrt{\varepsilon_0 \mu_0}$  is the speed of light and  $n_2$  is the coefficient of the nonlinear refractive index which is defined by

$$n_2 = \frac{\chi^{(3)}}{2n_0}. \quad (4.4)$$

Further, we assume that the wave is polarized in the  $y$ -direction, propagates in the  $z$ -direction and is confined in the  $x$ -direction such that  $\mathbf{E}$  is given by the following Ansatz

$$\mathbf{E} = \frac{1}{2} \{ A(z, x) \exp[i(k_0 z - \omega t)] + cc \} \cdot \mathbf{y} \quad (4.5)$$

where wave number  $k_0$  and frequency  $\omega_0$  are required to satisfy the linear dispersion relation  $k_0 = \omega n_0/c$ . Then Equation (4.3) becomes, after dividing by  $2k_0^2$ :

$$\frac{1}{2k_0^2} \frac{\partial^2 A}{\partial z^2} + \frac{i}{k_0} \frac{\partial A}{\partial z} + \frac{1}{2k_0^2} \frac{\partial^2 A}{\partial x^2} + \frac{n_2}{n_0} |A|^2 A = 0. \quad (4.6)$$

When applying the slowly varying envelope approximation (SVEA), one usually neglects the term containing the second derivative with respect to  $z$ , by which Equation (4.6) reduces to the NLS equation:

$$\frac{i}{k_0} \frac{\partial A}{\partial z} + \frac{1}{2k_0^2} \frac{\partial^2 A}{\partial x^2} + \frac{n_2}{n_0} |A|^2 A = 0. \quad (4.7)$$

In order to be more precise, we introduce a (dimensionless) *small parameter*  $\kappa$ ,  $0 < \kappa \ll 1$ . Now we assume that the envelope varies slowly along the propagation direction. To see what happens over very long but still finite distances, we define a 'slow' and a 'very slow' variables:

$$\begin{aligned} X &= \kappa k_0 x, \\ Z &= \kappa^2 k_0 z \end{aligned}$$

and scale the envelope by  $A(x, z) = \kappa \sqrt{n_0/n_2} B(X, Z)$ . It is worth noting that  $X, Z$  and  $B$  are dimensionless quantities. With these substitutions, Equation (4.6) can be written in the normalized form of the NLS equation

$$i \frac{\partial B}{\partial Z} + \frac{1}{2} \frac{\partial^2 B}{\partial X^2} + |B|^2 B = \mathcal{O}(\kappa^2), \quad (4.8)$$

where we have indicated that terms of  $\mathcal{O}(\kappa^2)$  are neglected. It is well known that the NLS equation is integrable which means it has an infinity of conservations laws and it can be solved using inverse scattering method, see e.g. [15]. It is also well known that the homogeneous NLS equation has soliton solutions which are very stable localised solutions and have particle-like properties. As an example, if two solitons collide, they can pass through each other maintaining their shapes and velocities. The effect of the collision is that the center of each soliton is shifted with respect to its original path (without collision).

**Remark 1** *In practice, the parameter  $\kappa$  is often used to measure the value of  $\kappa = 1/(k_0 w_0)$ , where  $w_0$  is the input beam width. Because the input beam width is typically much larger than its wavelength  $\lambda_0 = 2\pi/k_0$ , it follows that  $\kappa = \lambda_0/(2\pi w_0) \ll 1$ ; which is consistent with the definition of  $\kappa$ . We notice that even if the wavelength is comparable to the width, i.e.  $\lambda_0 \approx w_0$ , then  $\kappa^2 = 1/(4\pi^2) \ll 1$ . This is the motivation behind neglecting the second order contribution as done in Equation (4.8).*

## 4.2.2 Modified-NLS equation for non-uniform media

We will now introduce a transverse index variation in the  $x$ -direction as a small perturbation in the constant linear refractive index  $n_0$  in the displacement vector (4.2)

$$\mathbf{D} = \varepsilon_0 \left( n_0^2 (1 + \Delta n(x))^2 + \chi^{(3)} |E|^2 \right) \mathbf{E}. \quad (4.9)$$

where  $0 < \Delta n(x) \ll 1$ , i.e.  $\Delta n(x) = \mathcal{O}(\alpha)$  with  $\alpha$  is a small parameter.

Following the previous procedure, we obtain the following equation

$$\frac{1}{2} \kappa^2 \frac{\partial^2 B}{\partial Z^2} + i \frac{\partial B}{\partial Z} + \frac{1}{2} \frac{\partial^2 B}{\partial X^2} + \frac{1}{\kappa^2} \left( \Delta n(X) + \frac{1}{2} \Delta n(X)^2 \right) B + |B|^2 B = 0. \quad (4.10)$$

By taking  $\alpha \approx \kappa^3$ , the beam propagation equation, which is correct up to  $\mathcal{O}(\kappa^2)$  has the following form:

$$i \frac{\partial B}{\partial Z} + \frac{1}{2} \frac{\partial^2 B}{\partial X^2} + |B|^2 B = V B. \quad (4.11)$$

By rewriting  $\Delta n(X)/\kappa^2 = \widetilde{\Delta n}$ , the perturbation potential in Equation (4.11) is given by

$$V = -\widetilde{\Delta n}.$$

Equation (4.11) is the normalized NLS equation with an additional term in the right hand side. In the absence of perturbation, i.e.  $\widetilde{\Delta n} = 0$ , then Equation (4.11) reduces to the homogeneous NLS equation ( $V = 0$ ), cf. Equation (4.8). We remark that Equation (4.11) holds for arbitrary profiles  $\widetilde{\Delta n}$ . For convenience we will consider in this chapter a case where the transverse index variation  $\widetilde{\Delta n}$  has a triangular profile.

In [13], the beam propagation equation is derived by substituting the perturbation term directly into the NLS equation (4.7):  $n_0 \longrightarrow n_0(1 + \Delta n(x))$ . The resulting equation also takes the form of the inhomogeneous NLS equation (4.11), but now with the perturbation potential:

$$\tilde{V} = \Delta n(X) |B|^2. \quad (4.12)$$

It is worth noticing that the sign of  $\tilde{V}$  is different from that of  $V$ . In addition, the potential  $\tilde{V}$  produces a cubic nonlinearity which is not the case for  $V$ .

In our previous works ([24] and [25]), the propagation model is obtained by assuming that the total refractive index is

$$n^2 = (n_0(1 + \Delta n(x)) + n_2|E|^2)^2. \quad (4.13)$$

However, when deriving the inhomogeneous NLS equation, we follow the procedure as used to get Equation (4.7), i.e.  $\kappa$  is not considered. With this procedure, the perturbation potential is given by

$$\hat{V} = -\Delta n(X) (1 + |B|^2). \quad (4.14)$$

Observe that the potential  $\hat{V}$  has the same sign as  $V$  but includes additional nonlinear term.

**Remark 2** *In the theory of Bose-Einstein condensation, the inhomogeneous NLS equation (4.11) is also called the one-dimensional Gross-Pitaevskii equation which describes the evolution of the condensate wave function in an external potential  $V$  at zero temperature, see e.g. [20], [12] and [7]. In this case  $Z$  is the time variable and the third term in the left hand side characterizes the interaction between Bose particles. A soliton solution is one of eigenstates which represent a condensed assembly of trapped atoms, see [17].*

## 4.3 Propagation of a soliton beam in inhomogeneous media

### 4.3.1 Equivalent-particle approach

In this section we study the soliton propagation under the perturbation  $\tilde{\Delta n}$ . For this purpose, we will implement the equivalent-particle approach [1]. In this approach, the light beam is considered as a particle whose position is given by  $\overline{X}(Z)$  where  $Z$  is treated as the "time" variable. To find an equation of motion for the particle (beam), we begin by defining the center of the beam to be

$$\overline{X}(Z) = \frac{\int_{-\infty}^{\infty} X |B|^2 dX}{p(Z)}, \quad (4.15)$$

where

$$p(Z) = \int_{-\infty}^{\infty} |B|^2 dX \quad (4.16)$$

is the beam energy (or power). It follows from Equation (4.11) that the energy is conserved, i.e.  $dp/dZ = 0$ . Furthermore, we also obtain from Equation (4.11) that the velocity and the acceleration of the beam are respectively given by

$$v(Z) = \frac{d\bar{X}}{dZ} = \frac{1}{2} \frac{\int_{-\infty}^{\infty} (B\partial_X B^* - B^*\partial_X B) dX}{p(Z)}, \quad (4.17a)$$

$$\frac{d^2\bar{X}}{dZ^2} = \frac{dv}{dZ} = -p^{-1} \int_{-\infty}^{\infty} \frac{dV}{dX} |B|^2 dX. \quad (4.17b)$$

Expressions (4.17a)-(4.17b) are exact if  $B$  evolves according to Equation (4.11). We now introduce an approximation that the intensity  $|B|^2$  of the field moves as a single unit and is a function of a single coordinate  $X - \bar{X}(Z)$ . This means that the right-hand side of Equation (4.17b) is a function only of  $\bar{X}$ . Therefore, using the fact that  $p$  is constant, Equation (4.17b) can be written as

$$\frac{d^2\bar{X}}{dZ^2} = -\frac{\partial U(\bar{X})}{\partial \bar{X}}, \quad (4.18)$$

where the equivalent potential  $-U$  is the integral of the right-hand side of Equation (4.17b) w.r.t.  $\bar{X}$ . Equation (4.18) is a Newton's equation for the motion of a particle in the potential  $U(\bar{X})$ . So far we have only assumed that the light beam moves collectively, which means physically that the beam does not break up. Its principal response to the small perturbative potential  $V(X)$  is to change the position and the velocity of the beam. Naturally this assumption is not perfect, but we will verify this approximation by direct numerical experiments of the full governing equation (4.11).

### 4.3.2 A soliton beam in a triangular refractive index profile

Now we assume that the perturbation of the linear refractive index  $\widetilde{\Delta n}(X)$  has a triangular profile, i.e. of the form:

$$\widetilde{\Delta n}(X) = \begin{cases} 0, & X < -b \\ \Delta n_0 \left(1 + \frac{X}{b}\right), & -b \leq X < 0 \\ \Delta n_0 \left(1 - \frac{X}{b}\right), & 0 \leq X < b \\ 0, & X \geq b \end{cases}, \quad (4.19)$$

where  $2b$  is the total normalized width of the waveguide and  $\Delta n_0$  is the maximum index variation. From now on we call it a "triangular waveguide".

Now consider as input a beam of single soliton type:

$$B(X, Z=0) = \eta \operatorname{sech}[\eta(X - \bar{X}_0)] \quad (4.20)$$

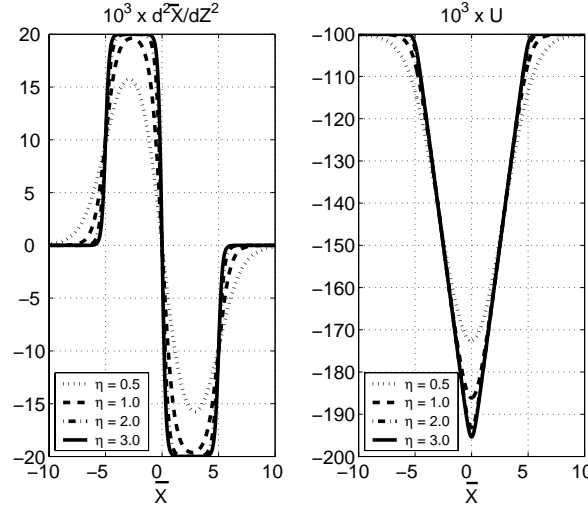


Figure 4.1: (a) Acceleration profile and (b) Newton potential ( $U$ ) versus transverse coordinate for different values of  $\eta$  in a triangular waveguide with  $b = 5$  and  $\Delta n_0 = 0.1$ .

where  $\bar{X}_0$  is the initial average position. In a *uniform* medium, the corresponding soliton solution is given by

$$B(X, Z) = \eta \operatorname{sech} [\eta (X - vZ - \bar{X}_0)] \exp \left[ i \left( vX + \frac{1}{2} (\eta^2 - v^2) Z \right) \right], \quad (4.21)$$

where the velocity  $v$  is constant. In a triangular waveguide we are considering here, we get as a (quasi-homogeneous) approximation for the soliton evolution the expression (in which the velocity  $v$  is now depending on  $Z$ )

$$B(X, Z) = \eta \operatorname{sech} [\eta (X - \bar{X}(Z))] \exp [i (v(Z) X + \sigma(Z))], \quad (4.22)$$

where

$$v(Z) = \frac{d\bar{X}(Z)}{dZ},$$

$$\frac{d\sigma(Z)}{dZ} = (\eta^2 - v(Z)^2) / 2.$$

The explicit formulae of the Newton potential  $U$  and the acceleration  $\frac{d^2\bar{X}}{dZ^2}$  can be found by substituting (4.19) and (4.22) into (4.18), i.e.

$$U = -\frac{\Delta n_0}{2b\eta} \ln \left[ \frac{(e^{2b\eta} + e^{2\eta\bar{X}}) (e^{2\eta(\bar{X}+b)} + 1)}{(e^{2\eta\bar{X}} + 1)^2} \right], \quad (4.23)$$

$$\frac{d^2\bar{X}}{dZ^2} = \frac{\Delta n_0}{b} \frac{e^{2\eta\bar{X}} (e^{2b\eta} - 1) (e^{2b\eta} + e^{2\eta\bar{X}} - e^{2\eta(\bar{X}+b)} - 1)}{(e^{2\eta\bar{X}} + 1) (e^{2\eta(\bar{X}+b)} + 1) (e^{2b\eta} + e^{2\eta\bar{X}})}. \quad (4.24)$$

It can be seen that the transverse acceleration and potential profiles depend linearly on the slope of the waveguide profile, i.e.  $\Delta n_0/b$ . Since the dependence of the acceleration on the soliton amplitude, as written in Equation (4.24), is rather difficult to understand, we show in Figure 4.1 the acceleration and the Newton potential profiles of solitons of different amplitudes  $\eta$  placed in a triangular waveguide with total width  $2b = 10$  and maximum index variation  $\Delta n_0 = 0.1$ . It is clear from this picture that the acceleration is an antisymmetric function of  $\bar{X}$ ; positive on the left side and negative on the other side. If the input is a soliton beam which has initial velocity  $v(0) = 0$  and is initially shifted to the left from the center of the triangular waveguide, the beam experiences a positive acceleration and therefore moves to the positive direction. When it passes the center of the waveguide the velocity decreases due to negative acceleration until it reaches zero velocity. Then the soliton experiences an opposite force, and so on. As a result the soliton oscillates periodically inside the triangular waveguide. This oscillating behavior can also be seen from the Newton potential profile in Figure 4.1.(b). It is also clear from Figure 4.1 that the acceleration depends on the soliton amplitude: the higher amplitude solitons experience higher acceleration and therefore have shorter oscillation periods. However, the acceleration and the potential profiles for higher amplitude solitons are saturated to certain profiles. In Figure 4.1, the acceleration and the potential profiles of a soliton which has amplitude  $\eta = 2$  almost coincides with those of a soliton of amplitude  $\eta = 3$ .

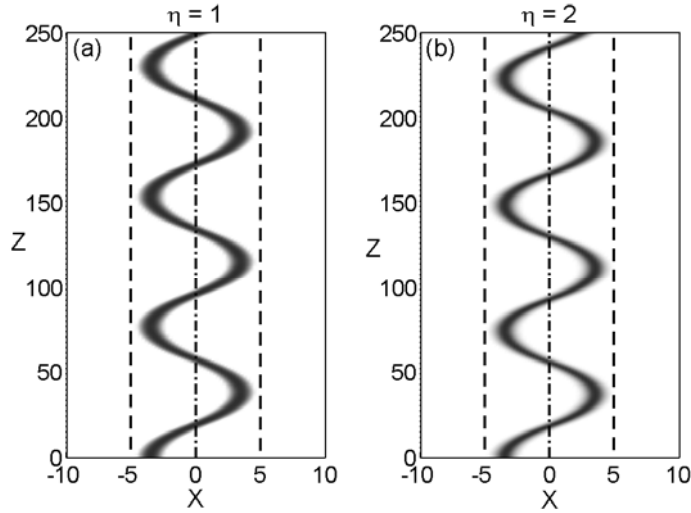


Figure 4.2: Numerical simulations of the propagation of a spatial soliton amplitude  $|B|$  with initial position  $\bar{X}_0 = -3.5$  in a triangular waveguide centered at  $X = 0$  with total width  $2b = 10$  and maximum index variation  $\Delta n_0 = 0.1$ . For (a)  $\eta = 1$ , (b)  $\eta = 2$ , the oscillations are shown, and confirm that the soliton with higher amplitude has a shorter oscillation period.

To confirm the theoretical predictions, we solve the governing modified-NLS equation (4.11) numerically using an implicit Crank-Nicholson scheme with the nonlinear term treated iteratively [8]. A Sommerfeld-type of transparent boundary condition (TBC) is employed on the edges of the computational window [14]. As input beam we take a single soliton of amplitude  $\eta$ :

$$B(X, Z = 0) = \eta \operatorname{sech} [\eta (X - \bar{X}_0)]$$

where  $\bar{X}_0$  is the initial average position. The width of the waveguide  $b$  and the maximum linear refractive index variation are taken as above to be 5 and 0.1, respectively. In Figure 4.2 we show the numerical results using  $\bar{X}_0 = -3.5$  for two different amplitudes. These numerical results perfectly agree with the theory that the soliton beam oscillates inside the waveguide. Due to this oscillatory behavior Garzia *et al.* [13] call this behavior "swing effect".

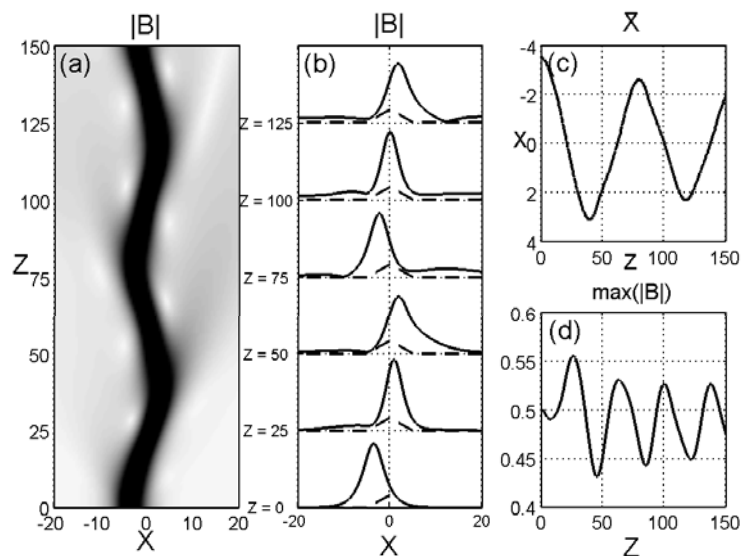


Figure 4.3: Numerical simulation of a soliton propagation with amplitude  $\eta = 0.5$  and initial position  $\bar{X}_0 = -3.5$  in a triangular waveguide with  $b = 5$  and  $\Delta n_0 = 0.1$ . In (a) the amplitude  $|B|$  is plotted. In (b) the beam profile is shown for different values of  $Z$ . Compare the width of the input beam and that of the waveguide (dashed-line represents the waveguide profile). In (c) and (d) the position of the maximum amplitude and the value of the maximum amplitude are plotted versus  $Z$ . Observe that the soliton is radiating when it swings.

Furthermore, in Figure 4.2 we show that a soliton of amplitude  $\eta = 2$  has a shorter oscillation period compared to a soliton with has amplitude  $\eta = 1$ . From other numerical simulations with  $\eta > 2$  which are not shown here, we observe that the difference between their oscillation periods becomes smaller and smaller for larger

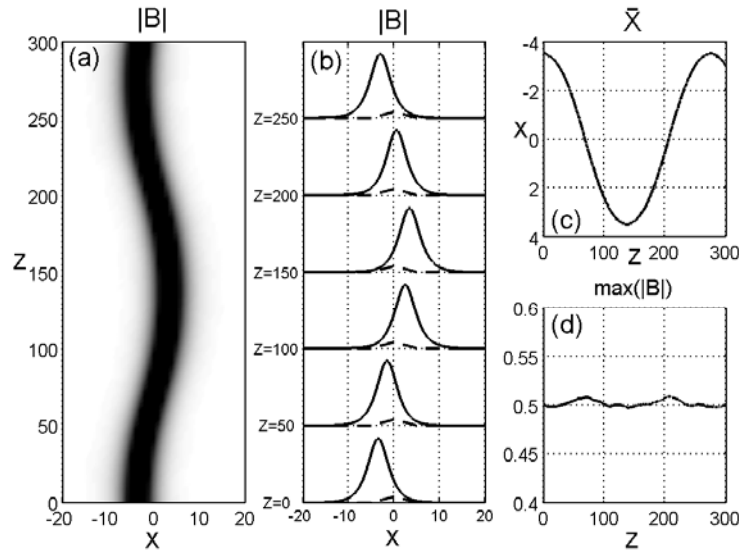


Figure 4.4: Same as Figure 3, but for a smaller maximum index variation  $\Delta n_0 = 0.01$ . During the propagation the soliton remains a single quantity and is oscillating inside the waveguide.

and larger amplitude solitons, as predicted.

In the previous numerical examples, we put the soliton in one side of a triangular waveguide where a half of its width, i.e  $b$ , is larger or comparable to the soliton width. In those cases, even though the soliton is placed in a relatively high index variation, it remains a single entity during its propagation, thus making that the theoretical prediction of the equivalent-particle approach is applicable here. However, if the width of the waveguide which has a relatively high index variation is narrow compared to the beam width, the soliton will be distorted and therefore the particle theory is valid only for a short distance. This kind of behavior is illustrated in Figure 4.3. In this picture, we show the dynamics of a soliton of amplitude  $\eta = 0.5$  in a waveguide which has parameters as above:  $b = 5$  and  $\Delta n_0 = 0.1$ . It is seen in Figure 4.3.(a) and 4.3.(b) that during the propagation the soliton emits some radiation when it swings in the waveguide, but the core part still oscillates around the center of the waveguide. Intuitively, this beam can be considered as a particle where its mass decreases monotonically during the propagation. As a result the oscillation of the core part of the particle is damped instead of periodic. This phenomena can be seen in Figure 4.3.(c). It is also worth noticing that during the oscillation the width of the core part decreases and its maximum amplitude increases when it is closer and closer to the waveguide center. The maximum value of the amplitude during the propagation is plotted in Figure 4.3.(d). In Figure 4.4 we show the result of a similar numerical experiment, but now with a much smaller maximum index variation  $\Delta n_0 = 0.01$ .



Different from the previous case, the soliton is not radiating (or the radiation can be neglected) and it remains oscillating periodically as a single unit.

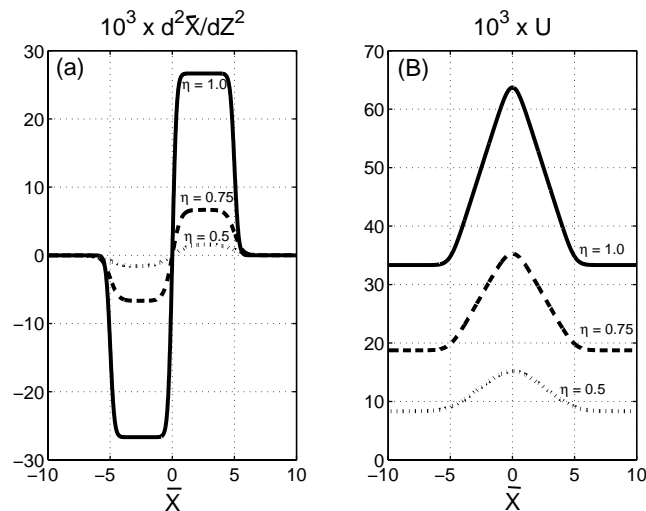


Figure 4.5: (a) Acceleration and (b) Newton potential ( $U$ ) versus transverse coordinate for different values of  $\eta$  with  $b = 5$  and  $\Delta n_0 = 0.1$  obtained from the model in [13]. Note the difference in sign of the acceleration compared to Figure 1.

For comparison, we show in Figure 4.5 the acceleration and the Newton potential profiles based on Equation (4.12) for solitons of different amplitude  $\eta$  in a triangular waveguide characterized by  $b = 5$  and  $\Delta n_0 = 0.1$ . The acceleration profile is also a skew-symmetric function of  $\bar{X}$ , but negative on the left side and positive on the right side. Hence, a soliton that is initially shifted from the center will always be forced outwards and exits the waveguide. Using this equation, this behavior is confirmed numerically as shown in Figure 4.6. However, the numerical results reported in [13] showed that a soliton always oscillates around the center of the waveguide. The conclusion must be that the model presented in [13] does not match with the numerical results reported in the same reference

#### 4.4 Break up of bound N-soliton into multiple independent solitons

It is well known [26] that in a uniform nonlinear dielectric medium, any initial profile will deform into a number of solitons and some radiation. In this section we investigate the behavior of a beam with soliton shape when it is placed in a triangular linear refractive index profile. Specifically we will consider as initial condition

$$B(X, Z = 0) = M\eta_0 \operatorname{sech}(\eta_0 X). \quad (4.25)$$

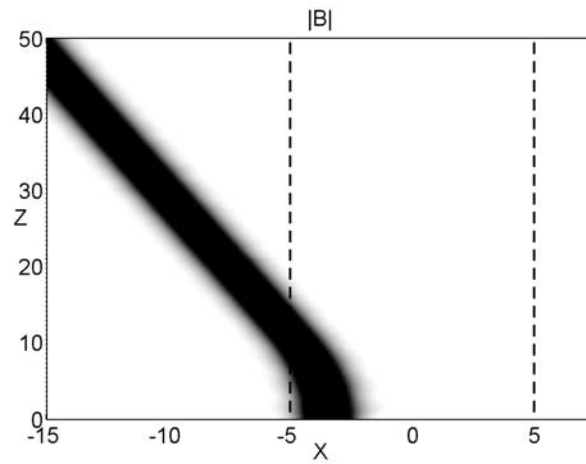


Figure 4.6: Propagation of spatial soliton in triangular waveguide based on the model in Ref. [13]. The soliton is not attracted towards the center of waveguide where the refractive index is maximum. Instead, the soliton is expelled from waveguide and does not show oscillatory behavior.

This initial value problem in a uniform medium was solved analytically by Satsuma and Yajima [21] using inverse scattering transform. Here we apply their results and combine them with equivalent-particle theory to predict the soliton behavior.

In a uniform medium, Satsuma and Yajima [21] showed that the initial condition (4.25) produces  $N$  solitons of amplitudes

$$\eta_n = 2\eta_0 \left( M - n + \frac{1}{2} \right), \quad n = 1, 2, \dots, N \quad (4.26)$$

with  $N$  determined by

$$M - \frac{1}{2} < N \leq M + \frac{1}{2}, \quad (4.27)$$

plus some radiation. If  $M$  is an integer,  $N = M$ , the solution is called an exact  $N$ -soliton since the radiation is absent. In the frame of reference of the spatial 'group velocity', all soliton velocities are zero and the solution  $B(X, Z)$  is called a bound  $N$ -soliton. Examples of bound 2- and 3-solitons in a uniform medium are shown in Figure 4.7.

In the previous section we found that a single soliton propagates as a particle in a potential defined as in Equation (4.18). Inside a triangular waveguide, solitons with different amplitudes oscillate with different periods. However, if the initial data can produce a bound  $N$ -soliton then it is probably not a single-particle problem anymore. Therefore we should consider it as an interacting  $N$ -particle in a composite potential. In this chapter we will not give a complete description of this composite potential and the resulting dynamics. Instead, we show some results of numerical simulations and

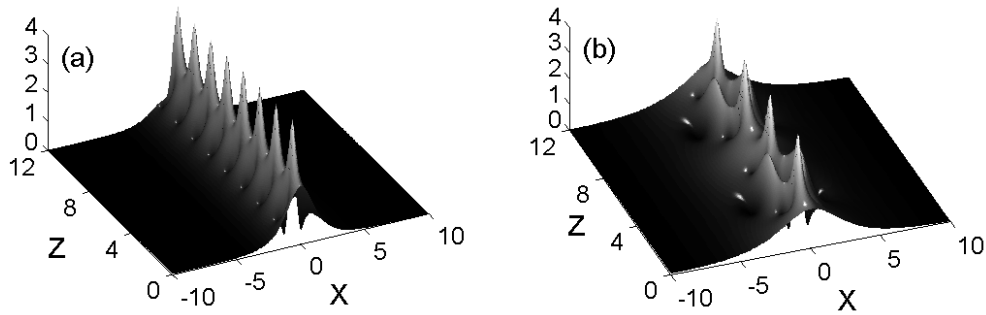


Figure 4.7: Numerical simulations of  $N$ -bound soliton in a uniform medium with (a)  $N = 2; \eta_1 = 1.0, \eta_2 = 3.0$ , (b)  $N = 3; \eta_1 = 0.5, \eta_2 = 1.5$  and  $\eta_3 = 2.5$ , which correspond to the initial profile (a)  $B(X, 0) = 2 \operatorname{sech}(X)$  and (b)  $B(X, 0) = (3/2) \operatorname{sech}(X/2)$ , respectively.

provide an intuitive explanation. According to Satsuma and Yajima [21], the bound- $N$ -soliton consists of  $N$  solitons with different amplitude. Although these  $N$  solitons initially have the same velocity, they will experience different acceleration because they have different amplitudes. As a result the bound- $N$ -soliton will be splitted into  $N$  individual solitons, and outside regions of collision each soliton travels with its own effective potential.

In Figure 4.8 we present numerical simulations with Equation (4.11) of a bound soliton in a triangular waveguide for  $M = 2$  and (a)  $\eta_0 = 0.75$  and (b)  $\eta_0 = 1.0$ . According to Equation (4.26) and (4.27), the initial profile consists of two solitons of amplitudes  $\eta_1 = \eta_0$  and  $\eta_2 = 3\eta_0$ . It is seen in those pictures that each bound soliton initially moves collectively in the positive direction  $Z$  and tends to oscillate. Due to the interaction with the medium, each soliton which is contained in the bound soliton is changing its velocity. When its velocity is changed each soliton can be viewed as a single particle interacting with others. During this interaction process, the path of each soliton is perturbed; the path of each soliton after break up is not the same as if it is initially a single soliton. The effects of this interaction are clearly seen in Figure 4.8 from the interference patterns before the two solitons are splitted. The break up process is more pronounced where the bound soliton start to swing. In Figure 4.8.(a), we see that the lower amplitude soliton is expelled from the waveguide and continues to propagate outside the waveguide with constant velocity (remember that the refractive index outside the waveguide is constant). On the other hand, the higher amplitude soliton remains oscillating as a single soliton with fixed period. Similarly, when simulating with  $\eta_0 = 1.0$ , the lower amplitude soliton is also forced to the outer part of the waveguide when the higher amplitude soliton starts to swing. Different from the previous case, the soliton with smaller amplitude is again attracted to and oscillates inside the waveguide. Because these two solitons have different oscillation

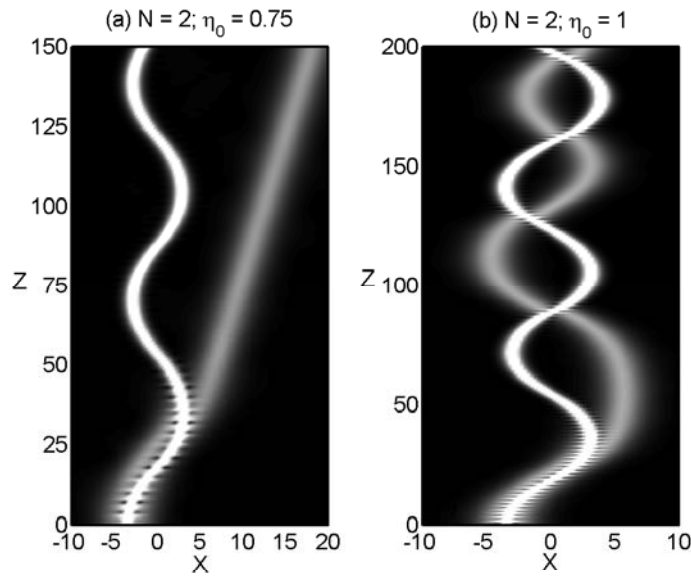


Figure 4.8: Numerical simulations using the modified-NLS equation that show the break up of 2-bound solitons in the triangular waveguide; in (a) for  $\eta_0 = 0.75$ , in (b) for  $\eta_0 = 1.0$ . The collision of two solitons corresponds to a trajectory transition  $AA'$  and the exiting soliton corresponds to a transition  $BB'$  in Figure 4.9 respectively.

period, they experience consecutive collisions. During collision, the "effective index" of a soliton changes due to the presence of other soliton where the smaller amplitude soliton experiences higher increment. As a result they are shifted from their original path, where the shift of the smaller amplitude soliton is bigger than that of the soliton with higher amplitude. This behavior is illustrated in Figure 4.8.(b), i.e. after collision the oscillation of each soliton changes its periodicity. In this case the period of the lower soliton becomes shorter while that of the higher soliton is getting longer. Other collisions may occur during their propagation. Looking at the phase portrait of a single soliton (see Figure 4.9), we can interpret these cases as follows. When two solitons interact with each other (e.g. during the splitting process or in the collision), the effect of the interaction can be represented in the phase plane as a transition from one trajectory to another one. If the interaction corresponds to a transition from  $A$  to  $A'$  (or reversed), the soliton is confined to the waveguide and remains oscillating; but with longer (or shorter) period, as in Figure 4.8.(b). When the interaction leads to a transition from  $B$  to  $B'$ , the soliton leaves the waveguide as happens in Figure 4.8.(a).

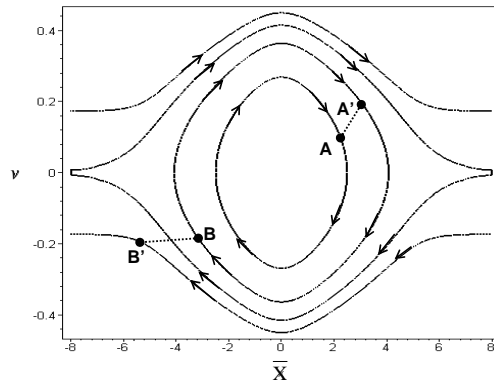


Figure 4.9: Phase portrait of a single soliton propagation in a triangular waveguide; a closed trajectory corresponds to oscillating motion within waveguide. A collision with another soliton is represented by a transition to another trajectory. If the collision causes a transition  $AA'$ , the soliton remains oscillating (with a different period). A transition  $BB'$  represents a case that the soliton exits the waveguide.

## 4.5 Concluding remarks

We have presented a model that describes the oscillatory behavior of a spatial soliton in a triangular waveguide. This model is derived by introducing a small perturbation of the constant linear refractive index in the displacement vector of the Maxwell equation. The perturbation method shows that the leading order of the resulting equation that includes the index variation takes the form of the inhomogeneous NLS equation. Using this propagation equation, it is shown analytically and numerically that a stationary soliton beam that is initially shifted from the center of a triangular waveguide will always oscillate in the waveguide. The oscillation period is found to depend on the soliton amplitude (beam intensity).

Based on the propagation properties of a soliton in a triangular waveguide, we showed that the effect of a triangular linear refractive index on a bound- $N$ -soliton is that it will always split into  $N$  individual solitons of different amplitudes. This behavior is confirmed numerically. Interesting phenomena of soliton break up have been simulated and show the effects of a soliton exiting from the waveguide or a perturbed oscillation path due to collision.

We remark that the propagation equation used in this chapter is based on the SVEA such that the nonparaxial term (the second derivative with respect to the propagation direction) measured by  $\kappa^2$  is completely neglected. That is to say, the initial beam is assumed to have a relatively large width  $w_0$  (i.e., a small  $\kappa$ ). As  $w_0$  becomes smaller,  $\kappa$  gets bigger and therefore the effect of nonparaxiality can no longer be neglected. The effect of weak nonparaxiality will be studied in the next chapter.

## References

- [1] A.B. Aceves, J.V. Moloney, and A.C. Newell, Theory of light-beam propagation at nonlinear interfaces. I. Equivalent-particle theory for a single interface, *Phys. Rev.* **A39**, p. 1809, 1989.
- [2] A.B. Aceves, J.V. Moloney, and A.C. Newell, Theory of light-beam propagation at nonlinear interfaces. II. Multiple-particle and multiple-interface extensions, *Phys. Rev.* **A39**, p. 1828, 1989.
- [3] J.S. Aitchison, A.M. Weiner, Y. Silberberg, M.K. Oliver, J.L. Jackel, D.E. Leaird E.M. Vogel and P.W. Smith, Observation of spatial optical solitons in a nonlinear glass waveguide, *Opt. Lett.* **15**, p. 471, 1990.
- [4] J.S. Aitchison, Y. Silberberg, A.M. Weiner, D.E. Leaird, M.K. Olivier, J.L. Jackel, and P.W.E. Smith, Spatial optical solitons in planar glass waveguides, *J. Opt. Soc. Am.* **B8**, p. 1290, 1991.
- [5] A. Barthelemy, S. Maneuf and C. Froehly, Propagation soliton et auto-confinement de faisceaux laser par non linearit optique de kerr, *Opt. Commun.* **55**, p. 201, 1985.
- [6] G. Cancellieri, F. Chiaraluce, E. Gambi, and P. Pierleoni, Coupled-soliton photonic logic gates - Practical design procedures, *J. Opt. Soc. Am.* **B12**, p. 1300, 1995.
- [7] M.M. Cerimele, M.L. Chiofalo, F. Pistella, S. Succi and M.P. Tosi, Numerical solution of the Gross-Pitaevskii equation using an explicit finite-difference scheme: An application to trapped Bose-Einstein condensates, *Phys. Rev.* **E62**, p. 1382, 2000.
- [8] Q.S. Chang, E.H. Jia and W. Sun, Difference schemes for solving the generalized nonlinear Schrödinger equation, *J. Comput. Phys.* **148**, p. 397, 1999.
- [9] R.Y. Chiao, E. Garmire, and C.H. Townes, Self-Trapping of Optical Beams, *Phys. Rev. Lett.* **13**, p. 479, 1964.
- [10] R.Y. Chiao, Introduction to Spatial Solitons, in *Spatial Solitons*, S. Trillo and W. Torruellas (Eds.), (Springer-Verlag Berlin Heidelberg, Germany, 2001).
- [11] R. De La Fuente, A. Barthelemy, and C. Froehly, Spatial-soliton-induced guided waves in a homogeneous nonlinear Kerr medium, *Opt. Lett.* **16**, p. 793, 1991.
- [12] Y.B. Gaididei, J. Schjødt-Eriksen and P.L. Christiansen, Collapse arresting in an inhomogeneous quintic nonlinear Schrödinger model, *Phys. Rev. E*, **60**, p. 4877, 1999.

- [13] F. Garzia, C. Sibilia, and M. Bertolotti, Swing effect of spatial soliton, *Opt. Commun.* **139**, p. 193, 1997.
- [14] G.R. Hadley, Transparent boundary-condition for beam propagation, *Opt. Lett.* **16**, p. 624, 1991.
- [15] A. Hasegawa and Y. Kodama, *Solitons in optical communications*, (Clarendon Press, Oxford, 1995).
- [16] E. Infeld and G. Rowlands, *Nonlinear waves, solitons, and chaos*, (Cambridge Univ. Press,
- [17] S.A. Morgan, R.J. Ballagh and K. Burnett, Solitary-wave solutions to nonlinear Schrödinger equations, *Phys. Rev.*, **A55**, p. 4338, 1997.
- [18] Y.H. Pramono, M. Geshiro, and T. Kitamura, Optical logic OR-AND-NOT and NOR gates in waveguides consisting of nonlinear material, *IEICE Trans. Elect.* **E83-C**, p. 1755, 2000.
- [19] D.H. Reitze, A.M. Weiner, and D.E. Leaird, High-power femtosecond optical pulse compression by using spatial solitons, *Opt. Lett.* **16**, p. 1409, 1991.
- [20] P.A. Ruprecht, M.J. Holland, K. Brunett and M. Edwards, Time-dependent solution of the nonlinear Schrödinger equation for Bose-condensed trapped neutral atoms, *Phys. Rev.* **A51**, p. 4704, 1995.
- [21] J. Satsuma and N. Yajima, Initial Value Problems of One-dimensional Self-Modulation of Nonlinear Waves in Dispersive Media, *Suppl. Prog. Theor. Phys.* **55**, p. 284, 1974.
- [22] J. Scheuer and M. Orenstein, Interactions and switching of spatial soliton pairs in the vicinity of a nonlinear interface, *Opt. Lett.* **24**, p. 1735, 1999.
- [23] T. Shi and S. Chi, Nonlinear photonic switching by using the spatial soliton collision, *Opt. Lett.* **15**, p. 1123, 1990.
- [24] A. Suryanto and E. van Groesen, On the swing effect of spatial inhomogeneous NLS solitons, *J. Nonlin. Opt. Phys. Mat.* **10**, p. 143, 2001.
- [25] A. Suryanto and E. van Groesen, Break up of bound-N-spatial-soliton in a ramp waveguide, *Opt. Quant. Electron.* **34**, p. 597, 2002.
- [26] V.E. Zakharov and A.B. Shabat, Exact theory of two-dimensional self-focusing and one-dimensional self-modulation of waves in nonlinear media, *Sov. Phys. JETP* **34**, p. 62, 1972.
- [27] M. Zitelli, E. Fazio, and M. Bertolotti, All-optical NOR gate based on the interaction between cosine-shaped input beams of orthogonal polarization, *J. Opt. Soc. Am.* **B16**, p. 214, 1999.





## Chapter 5

# Weakly nonparaxial beam propagation in Kerr nonlinear media

### 5.1 Introduction

So far, we have discussed interesting phenomena in the propagation of an initially bi-plane wave (i.e. a linear superposition two plane waves) which is a spatial analog of a bichromatic pulse in uniform Kerr medium (chapter 3) and soliton propagation under the influence of a transverse linear index variation (chapter 4). However, those studies are based on the (1+1)D nonlinear Schrödinger (NLS) equation where the slowly varying envelope approximation (SVEA) (or paraxial approximation) has been applied. Here  $(m + 1)$ D is meant for  $m$  transverse dimensions and one propagation direction. In this chapter, the effects of the nonparaxiality will be studied in order to check the validity of the (1+1)D NLS equation. This is motivated by the appearance of a large variation in amplitude that may result from the bi-plane wave deformation or from the break up of a bound-N-soliton (e.g. in the splitting process).

The validity of the SVEA is, in fact, already questioned for a long time. It was started by the prediction of [8] in 1965 that the (2+1)D NLS equation may produce a catastrophic collapse of a self-focusing beam, i.e. the beam amplitude blows up to infinity. With the probability for a collapse, a considerable part of studies on the self-focusing phenomenon has been directed towards finding mechanisms that arrest the collapse. It has been shown that a medium with saturable nonlinearity (see e.g. [3] and [7]) and negative contributions to the index of refraction due to avalanche ionization [12] as well as a quintic nonlinearity [9] can arrest the collapse. However,

these are properties specifying the given medium, while, as pointed out by Feit and Fleck [4], the self-focusing occurs in a variety of media without catastrophic collapse. This justifies the necessity of a medium-independent mechanism model which yields beams with nonsingular behavior. In this direction, Feit and Fleck [4] showed that the unphysical collapse is due to the invalidity of the paraxial wave equation during the advanced stages of self-focusing. They showed that if the nonparaxiality is included then the self-focusing is noncatastrophic, i.e. the nonparaxiality replaces the catastrophic focusing with a sequence of focusing-defocusing cycles. This behavior is confirmed both numerically by Akhmediev *et al.* ([1] and [11]), by Sheppard and Haelterman [10] and analytically by Fibich [5].

Up to now, most works on the effects of the nonparaxiality have been restricted to study the phenomenon of the catastrophic self-focusing arrest. Different from (2+1)D case, based on the inverse scattering method, an optical beam propagating in (1+1)D is predicted to be stable against collapse. Therefore the effects of the nonparaxiality in (1+1)D received only little attention. Here we will study the effects of the nonparaxiality on (1+1)D beam propagation in Kerr media. To do so, we derive a beam propagation model which includes the weak nonparaxiality using perturbation theory in section 5.2. In section 5.3 we derive a conserved quantity of the present model and compare with those of the nonlinear Helmholtz (NLH) and nonlinear Schrödinger (NLS) equation. The soliton propagation in uniform media and in a Gaussian waveguide are respectively discussed in section 5.4 and section 5.5. In section 5.6 we study the break up of bound-2-soliton in a Gaussian waveguide. Then we discuss in section 5.7 the deformation of a beam which is initially composed by two linear plane waves. Finally, conclusions and remarks are given in the last section.

## 5.2 Nonparaxial correction to the NLS equation

In chapter 4 we showed that the evolution of the nonparaxial envelope beam in Kerr media with transverse index variation is modeled by the following NLH equation (cf. equation (4.10))

$$i \frac{\partial B}{\partial Z} + \frac{1}{2} \frac{\partial^2 B}{\partial X^2} + |B|^2 B + \widetilde{\Delta n} B + \kappa^2 \left( \frac{1}{2} \frac{\partial^2 B}{\partial Z^2} + \frac{1}{2} \widetilde{\Delta n}^2 B \right) = 0, \quad (5.1)$$

where the scaled transverse index variation  $\widetilde{\Delta n} \equiv \widetilde{\Delta n}(X)$  is small, i.e. of the order  $\kappa$ . In Equation (5.1),  $X, Z$  and  $B$  are dimensionless variables where their corresponding physical quantities are determined by the following transformation

$$\begin{aligned} x &= \frac{X}{\kappa k_0}, \\ z &= \frac{Z}{\kappa^2 k_0}, \\ A(x, z) &= \kappa \sqrt{n_0/n_2} B(X, Z), \end{aligned} \quad (5.2)$$

with  $k_0 = \omega n_0/c$  is the wavenumber of the carrier wave and the small nonparaxiality parameter  $0 < \kappa \ll 1$  can be related to the ratio of the input vacuum wavelength  $\lambda_0$  and the input beam width  $w_0$ :  $\kappa = \lambda_0/(2\pi w_0)$ . The relation between the beam envelope  $A(x, z)$  and the electric field is given by

$$\mathbf{E} = \frac{1}{2} \{A(z, x) \exp[i(k_0 z - \omega t)] + cc.\} \cdot \mathbf{y}. \quad (5.3)$$

Equation (5.1) is an elliptic equation. In order to solve the NLH equation, we have to provide boundary conditions that limit the computational domain. In our case, the required boundary conditions have to be transparent for all outgoing waves and simultaneously model the incident waves; such conditions are called Transparent-Influx Boundary Conditions (TIBC). To the best of our knowledge, a proper TIBC for inhomogeneous nonlinear media is not known. Furthermore, apart from the lack of TIBC, to perform accurate numerical simulations we usually need a very large number of grid points, making the computations too expensive for a standard personal computer. Therefore, the standard approach in solving the NLH equation numerically is to approximate it with an initial value problem. The simplest approximation of Equation (5.1) that is correct up to  $\mathcal{O}(\kappa^2)$  takes the form of the inhomogeneous nonlinear Schrödinger (NLS) equation

$$i \frac{\partial B}{\partial Z} + \frac{1}{2} \frac{\partial^2 B}{\partial X^2} + |B|^2 B + \widetilde{\Delta n} B = 0. \quad (5.4)$$

This equation (discussed in chapter 4, see Equation (4.11)) is derived from Equation (5.1) by neglecting the nonparaxial effects (the first term in brackets) and high order terms. In fact, the size of the nonparaxial effect which arises from the non-slowly varying envelope (non-SVE) is determined by the value of  $\kappa^2$ . If  $\kappa^2$  is large enough then the nonparaxial effect may become important and therefore it can no longer be neglected. To reveal the effect of nonparaxiality we will improve the NLS equation (5.4) by including terms of the order up to  $\kappa^3$ . To this end, we will evaluate the non-SVE term in the NLH equation by noting that

$$\frac{\partial B}{\partial Z} = i \left( \frac{1}{2} \frac{\partial^2 B}{\partial X^2} + |B|^2 B + \widetilde{\Delta n} B \right) \quad (5.5)$$

is accurate up to order  $\kappa$  where the contribution of the order of  $\kappa^2$  and smaller have been neglected. Then the non-SVE contribution can be approximated in order  $\kappa^3$  :

$$\begin{aligned}
\frac{\kappa^2}{2} \frac{\partial^2 B}{\partial Z^2} &\approx \frac{\kappa^2}{2} i \left[ \frac{1}{2} \frac{\partial^2 B}{\partial Z \partial X^2} + \widetilde{\Delta n} \frac{\partial B}{\partial Z} + \frac{\partial (|B|^2 B)}{\partial Z} \right] \\
&= -\frac{\kappa^2}{2} \left[ \frac{1}{4} \frac{\partial^4 B}{\partial X^4} + \left( \frac{1}{2} \frac{d^2 \widetilde{\Delta n}}{dX^2} + \widetilde{\Delta n}^2 \right) B + \frac{d\widetilde{\Delta n}}{dX} \frac{\partial B}{\partial X} \right. \\
&\quad + \left( \widetilde{\Delta n} + |B|^2 \right) \frac{\partial^2 B}{\partial X^2} + 2\widetilde{\Delta n} |B|^2 B + |B|^4 B \\
&\quad \left. + \frac{1}{2} \frac{\partial^2 (|B|^2 B)}{\partial X^2} - \frac{1}{2} B^2 \frac{\partial^2 B^*}{\partial X^2} \right], \tag{5.6}
\end{aligned}$$

where  $B^*$  stands for the complex conjugate of  $B$ . The approximation in (5.6) represents one step beyond the slowly varying envelope approximation (SVEA) applied in the NLS equation, but still assumes a slowly varying envelope such that further nonparaxial terms of the order  $\kappa^4$  and higher order terms can be neglected. In other words, the nonparaxial effect is assumed to be weak but nonvanishing.

By replacing the nonparaxial term in Equation (5.1) with its approximation (5.6), we obtain a higher-order nonlinear beam propagation equation

$$\begin{aligned}
i \frac{\partial B}{\partial Z} + \frac{1}{2} \frac{\partial^2 B}{\partial X^2} + |B|^2 B + \widetilde{\Delta n} B &= \frac{\kappa^2}{2} \left[ \frac{1}{4} \frac{\partial^4 B}{\partial X^4} + \frac{1}{2} \frac{d^2 \widetilde{\Delta n}}{dX^2} B + \frac{d\widetilde{\Delta n}}{dX} \frac{\partial B}{\partial X} \right. \\
&\quad + 2\widetilde{\Delta n} |B|^2 B + \left( \widetilde{\Delta n} + |B|^2 \right) \frac{\partial^2 B}{\partial X^2} + |B|^4 B \\
&\quad \left. + \frac{1}{2} \frac{\partial^2 (|B|^2 B)}{\partial X^2} - \frac{1}{2} B^2 \frac{\partial^2 B^*}{\partial X^2} \right]. \tag{5.7}
\end{aligned}$$

From now on we call this equation the nonparaxial nonlinear Schrödinger (NNLS) equation. Further improvement could be done iteratively but will not be treated here. Equation (5.7) takes the form of our standard inhomogeneous NLS equation (5.4) with perturbations which arise from the nonparaxiality. The perturbations include the linear nonparaxial diffraction, linear refractive index change, the diffraction that depends on the transverse index variation and on the intensity and the quintic nonlinearity. We remark that although Equation (5.7) involves higher-order contributions, it still neglects the coupling between forward-propagating waves and backscattering. However, with this approximation, the problem is greatly simplified when it is solved numerically. Indeed the resulting equation is still a one-way wave equation. The numerical study of a beam propagating in both homogeneous and inhomogeneous media with Kerr nonlinearity under the influence of weak nonparaxiality will be given in the next sections. For this purpose the NNLS equation (5.7) is solved numerically using an implicit Crank-Nicolson scheme [2] and transparent boundary conditions [6].

**Remark 3** *In the normalized (inhomogeneous) NLS equation (5.4), the parameter  $\kappa$  does not appear explicitly. Therefore the simulation results of this equation can be interpreted for any  $\kappa$ . As an example, for given two different values of  $\kappa$ , say  $\kappa_0$  and  $\kappa_1$ , the normalized NLS equation for those  $\kappa$ 's with the same normalized initial conditions will produce exactly the same results. However, according to Equation (5.2), the real physical situations are different. For this reason, from now on, the results of the NLS equation are denoted by  $\kappa = 0$ .*

### 5.3 Power conservation law

Before proceeding the numerical study, we will investigate the power flow conservations of the NLH equation and its approximations. To that end, we multiply Equation (5.1), (5.4) and (5.7) respectively by  $B^*$ , subtracting with the complex conjugate of it, and then integrating the resulting expression over the whole transverse coordinate. With this procedure we obtain the power flow invariant for the NLH equation

$$\frac{d}{dZ} \int_{-\infty}^{\infty} \left[ |B|^2 - i \frac{\kappa^2}{2} \left( B^* \frac{\partial B}{\partial Z} - B \frac{\partial B^*}{\partial Z} \right) \right] dX = 0, \quad (5.8)$$

which means that the value of

$$P_{\text{NLH}} = \int_{-\infty}^{\infty} \left[ |B|^2 - i \frac{\kappa^2}{2} \left( B^* \frac{\partial B}{\partial Z} - B \frac{\partial B^*}{\partial Z} \right) \right] dX \quad (5.9)$$

is a conserved quantity during propagation.  $P_{\text{NLH}}$  represents the component of the Poynting vector  $\mathbf{S} = \frac{1}{2} \text{Re} \{ \mathbf{E} \times \mathbf{H}^* \}$  in the propagation direction integrated over the whole transverse coordinate. This is the result that we would expect physically because in general theory of wave propagation in media without loss or gain, the power flow is a quantity that has to be constant. However, in the NLS equation, this conservation law is incomplete as the nonparaxial effect is completely neglected, i.e. only the first term in Equation (5.9):

$$P_{\text{NLS}} = \int_{-\infty}^{\infty} |B|^2 dX \quad (5.10)$$

is conserved. In the case of weak nonparaxiality such that the beam evolution takes the form of the NNLS equation (5.7), we obtain the approximate power conservation law in the form

$$P_{\text{NNLS}} = \int_{-\infty}^{\infty} \left[ |B|^2 + \frac{\kappa^2}{2} |B|^4 \right] dX + \mathcal{O}(\kappa^4), \quad (5.11)$$

which means that for the same initial input,  $P_{\text{NNLS}} \geq P_{\text{NLS}}$ . We note that Equation (5.11) can also be derived by directly substituting Equation (5.5) into Equation (5.9). We further notice that  $P_{\text{NLH}}$  and  $P_{\text{NNLS}}$  differ only by  $\mathcal{O}(\kappa^4)$  while the difference between  $P_{\text{NLH}}$  and  $P_{\text{NLS}}$  is  $\mathcal{O}(\kappa^2)$ . The conservation laws (5.9) and (5.11) reduce to the paraxial conservation law (5.10) only if  $\kappa^2 \rightarrow 0$ .

## 5.4 Soliton propagation in uniform media

Before studying the propagation of a soliton in inhomogeneous media, we consider first the case of a uniform medium, i.e. the index variation  $\widetilde{\Delta n} = 0$ . For this case, we look for a stationary soliton solution of these three equations (NLH, NLS, NNLS) by assuming that a shape-preserving solution exists and has the form

$$B(X, Z) = f(X) \exp(i\beta Z), \quad (5.12)$$

where both  $f$  and  $df/dX$  vanish as  $|X| \rightarrow \infty$ . Then we substitute this Ansatz into the three equations, respectively, and solve the resulting equations for  $f$  and  $\beta$  by assuming that  $f = \eta$  and  $df/dX = 0$  at the soliton peak (which is assumed to occur at  $X = 0$ ). We find that the three model equations (NLH, NLS, NNLS) have an exact soliton solution with the same profile but with different longitudinal wavenumbers  $\beta$ :

$$B(X, Z) = \eta \operatorname{sech}(\eta X) \exp(i\beta Z). \quad (5.13)$$

The longitudinal wavenumber of the NLH soliton is determined by the quadratic equation:  $(1/2)\kappa^2\beta_{\text{NLH}}^2 + \beta_{\text{NLH}} - (1/2)\eta^2 = 0$ , i.e.

$$\beta_{\text{NLH}} = \left(-1 + \sqrt{1 + \kappa^2\eta^2}\right) / \kappa^2. \quad (5.14)$$

The positive sign in front of the square root in Equation (5.14) is chosen in order to be consistent with the wavenumbers of the NLS and NNLS solitons which are respectively given by

$$\beta_{\text{NLS}} = \frac{1}{2}\eta^2, \quad (5.15)$$

$$\beta_{\text{NNLS}} = \left(\frac{1}{2}\eta^2 - \frac{1}{8}\kappa^2\eta^4\right). \quad (5.16)$$

To see the relation between the solution of the NLH equation and its approximations, we write the Taylor's expansion of  $\beta_{\text{NLH}}$  by assuming that  $\kappa^2\eta^2$  is small:

$$\beta_{\text{NLH}} \approx \frac{1}{2}\eta^2 - \frac{1}{8}\kappa^2\eta^4 + \mathcal{O}(\kappa^4). \quad (5.17)$$

It is evident that the wavenumbers of the stationary solution of both NLS and NNLS equations are the approximations of  $\beta_{\text{NLH}}$  but with different order of accuracy. This fact supports the conclusion that the NNLS equation is the reduction of the NLH equation which includes the lowest order nonparaxial correction under the NLS scaling. We remark that in the case of the exact stationary solution, the value of  $P_{\text{NLS}}$  is also a conserved quantity of the NNLS equation. This can be checked from the fact that the profile of the stationary solution of the NNLS equation is not deformed during propagation. Now we study the effect of nonparaxiality in the case where the

initial profile will distort during the evolution, i.e. by considering the initial value problem (IVP) through Equation (5.7) with an initial condition:

$$B(X, 0) = \eta^\pm \operatorname{sech}(X), \quad (5.18)$$

where  $\eta^\pm = 1 \pm 0.1$ . Notice that the initial condition (5.18) corresponds to a stationary soliton but with a perturbed-amplitude. In the regime of the paraxial approximation, it is well known from the inverse scattering method that the initial condition with (5.18) produces a soliton of unit amplitude plus radiation, see Equation (4.25). However, to the best of our knowledge, there is no exact theory that describes this IVP that includes the nonparaxiality. Therefore we will study this IVP numerically by solving Equation (5.7) with initial data (5.18).

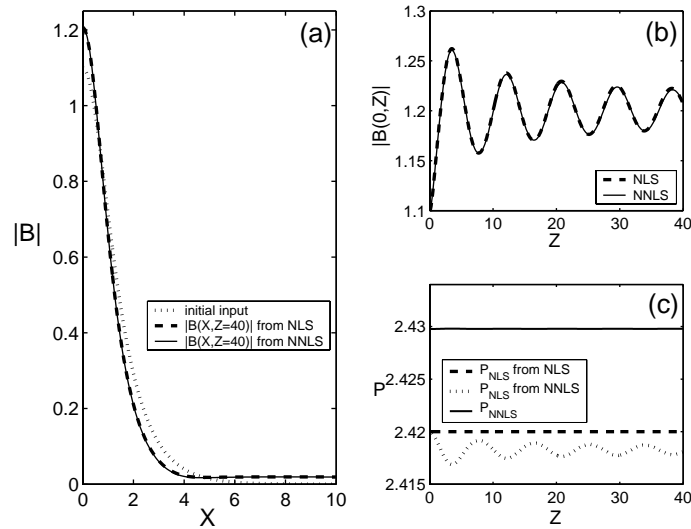


Figure 5.1: Propagation of a soliton with amplitude 10% higher ( $\eta^+ = 1.1$ ) for  $\kappa^2 = 0.01$  over a distance  $Z = 40$ . (a) The beam profiles at the final position obtained from the NLS equation (dashed) and from the NNLS equation (solid). For comparison, the initial profile is also plotted (dotted). (b) Evolution of the on-axis amplitude  $|B(0, Z)|$  showing that both paraxial and nonparaxial beams exhibit decaying focusing-defocusing cycles. (c) Evolution of  $P_{NLS}$  and  $P_{NNLS}$ . When the beam focuses (defocuses) the energy  $P_{NLS}$  obtained from then NNLS equation (dotted) decreases (increases) while that calculated from the NLS equation (dashed) is conserved. The conserved energy of the NNLS ( $P_{NNLS}$ ) is also plotted (solid).

In Figure 5.1 we compare the numerical results of the NLS and the NNLS equations for amplitude  $\eta^+$  and  $\kappa^2 = 0.01$ . We observe that in both paraxial and nonparaxial models, a "soliton" with a small excess amplitude ( $\eta^+$ ) initially experiences self-focusing (the amplitude increases in the middle and the beam width becomes narrower). When it reaches the maximum amplitude, the soliton starts to defocus and emits radiation.

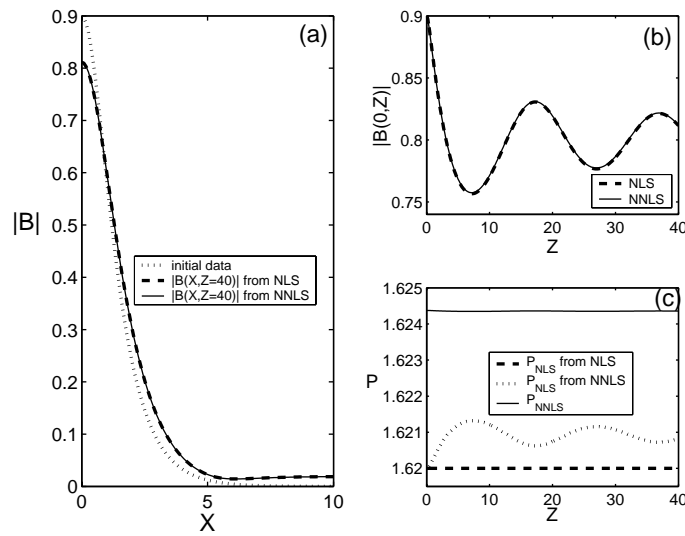


Figure 5.2: Same as for Figure 5.1, but for deficit amplitude  $\eta^- = 0.9$ . The amplitude oscillation shows the soliton stability.

The focusing-defocusing behavior with releasing radiation is repeated almost periodically. The direct observation of the amplitude during propagation shows that the quantitative difference between the paraxial and nonparaxial models is very small, see Figure 5.1.(a) and (b). However, a closer look indicates that the nonparaxiality produces a longer period of the focusing-defocusing cycles (see Figure 5.1.(b)). Furthermore, by monitoring the energy conservation, we conclude that the paraxial and nonparaxial beam propagation include different physical mechanisms. Indeed, in the case of the NLS equation although the beam follows a series of decaying focusing-defocusing oscillations which resembles the effect of diffraction and Kerr nonlinearity,  $P_{NLS}$  remains constant, see Figure 5.1. However, when the nonparaxiality is included in the calculation, the value of  $P_{NLS}$  is oscillating while  $P_{NNLS}$  is conserved. Figure 5.1.(b) and 5.1.(c) shows that when the beam is narrowing the contribution of the nonparaxial term in  $P_{NNLS}$  increases, taking the energy from the paraxial part which therefore decreases the NLS invariant  $P_{NLS}$ . When the beam become wider (diffracts), our numerical results show that  $P_{NLS}$  increases, as expected.

When the initial "soliton" has a small deficit amplitude ( $\eta^-$ ), our numerical calculations based on the paraxial and nonparaxial equations also show that the beam experiences a defocusing-focusing oscillation rather than directly diffracts into radiation, see Figure 5.2. Diffraction broadening for both paraxial and nonparaxial cases occurs only when the "soliton" amplitude is much smaller than 1. The defocusing-focusing behavior of the paraxial "soliton" is expected because the stationary paraxial soliton in (1+1)D is stable against a small change of initial data. This is different from the case of the paraxial soliton in (2+1)D where the soliton beam with initial



energy deficit will experience diffraction broadening. Under the nonparaxial effect, for a small excess or a deficit amplitude,  $P_{\text{NLS}}$  shows an oscillatory behavior; showing that the nonparaxial contributions control the mechanism of self-focusing and defocusing (due to diffraction). In (1+1)D case, this behavior may be considered to be less important. However, this phenomenon becomes essential in (2+1)D in order to stabilize the soliton beam [10].

## 5.5 Soliton propagation in non-uniform media

The propagation of a spatial soliton in an inhomogeneous medium under the paraxial approximation which is modeled by Equation (5.4) has been studied in the previous chapter. When the inhomogeneity  $\widetilde{\Delta n}(X)$  has a triangular profile, called triangular waveguide, it has been shown that a stationary soliton beam placed in one side of a triangular waveguide will oscillate periodically around the center of the waveguide. In this section we will study the effects of nonparaxiality on this behavior. As discussed in section 5.2, the governing equation that includes the nonparaxial contributions takes the form of the NNLS equation (5.7). To avoid the singularity of the derivative of the transverse index variation which may cause a numerical problem, we assume that  $\widetilde{\Delta n}$  has a Gaussian profile

$$\widetilde{\Delta n}(X) = \Delta n_0 \exp(-bX^2) \quad (5.19)$$

rather than a triangular profile. Here,  $\Delta n_0$  is the maximum index variation and  $b$  is a constant that controls the width of the waveguide. To see the effect of nonparaxiality, we first look back to the stationary soliton solution of the homogeneous NLS and NNLS equations, see Equation (5.13), where the longitudinal wavenumbers are respectively given by Equation (5.15) and Equation (5.16). It is clear that for  $\kappa \neq 0$  the longitudinal wavenumber of the nonparaxial soliton is always smaller than that of the paraxial soliton of the same amplitude. We note that  $\kappa = 0$  means the beam has infinite width. Indeed, the difference between  $\beta_{\text{NLS}}$  and  $\beta_{\text{NNLS}}$  is

$$\beta_{\text{NLS}} - \beta_{\text{NNLS}} = \kappa^2 \eta^4 / 8. \quad (5.20)$$

As a result the longitudinal wavelength of the nonparaxial soliton is larger than that of the paraxial one. That is to say, the nonparaxial soliton experiences a larger longitudinal force ( $F_Z$ ). Now we make an assumption (that will be justified later), that if a transverse inhomogeneity  $\widetilde{\Delta n}$  is introduced then both paraxial and nonparaxial solitons will experience the same transversal force ( $F_X$ ) at any  $X$  which in combination with the longitudinal force  $F_Z$  causes an oscillatory behavior as seen in chapter 4. Since the nonparaxial soliton experiences a larger  $F_Z$  than the paraxial one, it will have a longer oscillation period. This situation is illustrated schematically in Figure 5.3. From Equation (5.20) we conclude that the difference between the oscillation

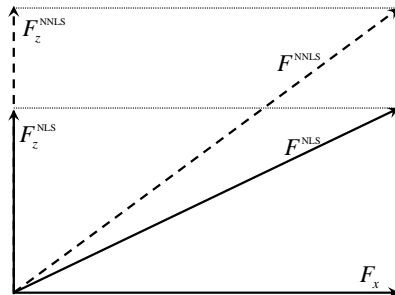


Figure 5.3: In the mechanical analogy, both paraxial and nonparaxial solitons in a Gaussian waveguide experience the same transversal force ( $F_x$ ) but different longitudinal forces ( $F_z$ ). Since the longitudinal force in the nonparaxial case is larger, the oscillation period is longer in that case.

period of the nonparaxial and that of the paraxial case is larger for a larger degree of nonparaxiality  $\kappa$  or for a higher soliton amplitude  $\eta$ .

To confirm these theoretical predictions, we perform numerical simulations based on Equation (5.7) using the initial condition

$$B(X, 0) = \eta \operatorname{sech}[\eta(X - X_0)], \quad (5.21)$$

where  $X_0$  represents the initial position of the soliton. In all calculations presented in this section, we take  $X_0 = -3.5$ ,  $\Delta n_0 = 0.1$  and  $b = 0.1$ . In Figure 5.4 we show the simulation results for  $\kappa^2 = 0.001$  and  $\kappa^2 = 0.01$  with the same amplitude  $\eta = 1$ . For comparison we also plot the result of the NLS equation ( $\kappa = 0$ ). Figure 5.4.(a) shows the oscillatory behavior of the position of the maximum amplitude. It is found that the (normalized) oscillation period for larger  $\kappa^2$  is longer than that for smaller one. This behavior cannot be seen clearly on the scale of Figure 5.4.(a) because the differences between the oscillation period of  $\kappa^2 = 0.001$  and  $0.01$  are very small. To see this behavior more clearly we plot in Figure 5.4.(b) the soliton profiles for different  $\kappa^2$  at the final position of our simulation, i.e. at  $Z = 200$ . It is shown here that the soliton for  $\kappa^2 = 0.01$  arrives later than the others (remember that Figure 5.4.(b) corresponds to the left-going beam). The effect of nonparaxiality is more pronounced when we increase the soliton amplitude as one should expect, e.g. see Figure 5.5 for  $\eta = 2$ .

To verify that the larger oscillation period caused by the nonparaxial effect is mainly due to the smaller longitudinal wavenumber  $\beta$ , we need to improve the NLS equation (5.4) in such a way that the homogeneous version of the resulting equation (i.e. for  $\widetilde{\Delta n} = 0$ ), called the improved-NLS (iNLS) equation, has a stationary soliton solution with  $\beta = \beta_{\text{NNLS}}$ . One can check that this requirement is satisfied by the following equation

$$i \left( 1 + \frac{\kappa^2 \eta^2}{4 - \kappa^2 \eta^2} \right) \frac{\partial B}{\partial Z} + \frac{1}{2} \frac{\partial^2 B}{\partial X^2} + |B|^2 B + \widetilde{\Delta n} B = 0. \quad (5.22)$$

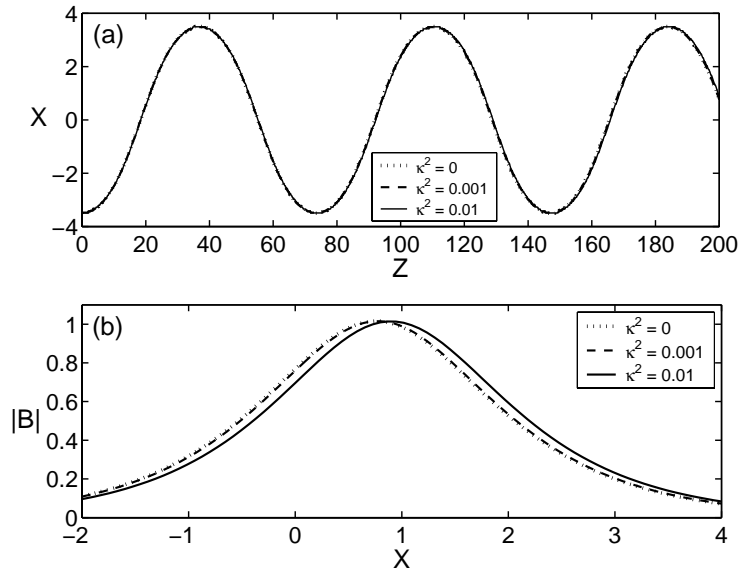


Figure 5.4: Propagation of a single soliton of amplitude  $\eta = 1$  in a Gaussian waveguide for  $\kappa^2 = 0, 0.001$  and  $0.01$ . (a) The position of the maximum amplitude, showing the oscillatory behavior of both paraxial and nonparaxial solitons. The differences between the oscillation periods of  $\kappa^2 = 0, 0.001$  and  $0.01$  are very small such that they cannot be seen on the scale of this plot. (b) The period differences are clearly seen in the plot of the soliton profile at the final propagation distance  $Z = 200$ .

This Figure 5.6 shows the numerical results of Equation (5.22) for  $\eta = 1$  and  $\eta = 2$  using  $\kappa^2 = 0.01$ . It is evident that those results agree quite well to the results of the NNLS equation (5.7), showing that the iNLS equation indeed improves significantly the period of the soliton oscillation. We conclude that the nonparaxiality in a Kerr medium which has a Gaussian refractive index profile increases the oscillation period.

## 5.6 Propagation of bound-N-soliton

We now consider the initial data:

$$B(X, 0) = 2\eta_0 \operatorname{sech}[\eta_0(X - X_0)]. \quad (5.23)$$

It was discussed in chapter 4 that the initial data (5.23), in a uniform medium under the paraxial approximation, generates two solitons of amplitude  $\eta_1 = \eta_0$  and  $\eta_2 = 3\eta_0$ , respectively. These two solitons have the same longitudinal velocity and travel together; and therefore this is also called a bound soliton. During the propagation this bound soliton shows a periodic focusing-defocusing (breathing behavior) without

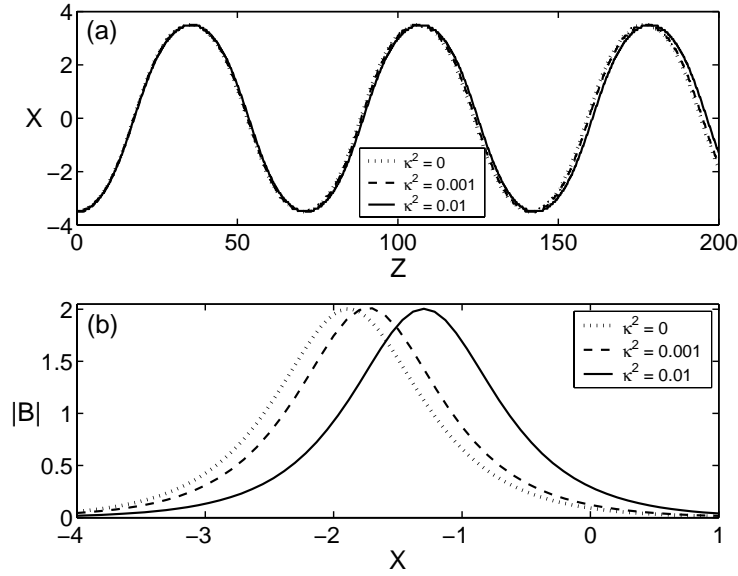


Figure 5.5: Same as for Figure 5.4, but for  $\eta = 2$ . The effect of nonparaxiality is more pronounced compared to that of  $\eta = 1$ .

releasing radiation, see e.g. Figure 5.7.(a). However, if we introduce nonparaxiality, we predict the following phenomena:

- Similar to the case that is presented in section 5.4, the initial field (5.23) gives rise to a breathing behavior (periodic focusing-defocusing). However, because this initial condition may be not the perfect initial data to generate a nonparaxial bound soliton, we may expect that the focusing-defocusing cycles are accompanied by radiation.
- By considering that the initial data produces at least one nonparaxial soliton (and the remainder can form another soliton or a radiating entity), these two entities (soliton and the remainder) will have a smaller longitudinal wavenumber compared to their paraxial version. Therefore the period of the focusing-defocusing cycle in the nonparaxial case is larger than that in paraxial one.
- As discussed earlier, the nonparaxiality influences the mechanism of the focusing-defocusing series which in the (2+1)D case can arrest the collapse. This phenomenon can also cause the peak amplitude due to self-focusing in nonparaxial case to be smaller than in paraxial one.

Indeed, those phenomena are confirmed by our numerical simulations. For example we plot the numerical results for the case of  $\eta_0 = 1$  and  $X_0 = 0$  in Figure 5.7.

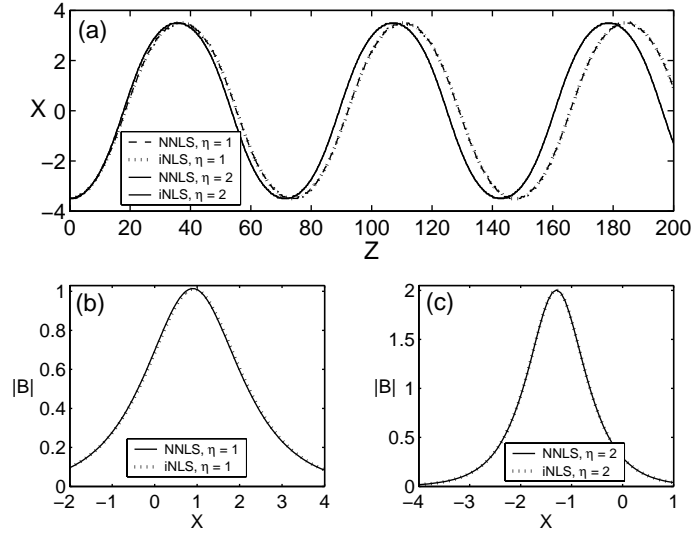


Figure 5.6: Same as for Figure 5.4 and 5.5 but calculated from the iNLS equation for respectively  $\eta = 1$  (dotted-line in (a)) and  $\eta = 2$  (thin-solid-line in (a)) with  $\kappa^2 = 0.01$ . Comparison to the results of the NNLS equation shows that the iNLS improves significantly the NLS equation.

Now we introduce a linear transverse index variation  $\widetilde{\Delta n}(X)$  of the form (5.19). We have shown in the previous chapter that in the paraxial approach the bound-2-soliton produced by initial data (5.23) is splitted into two individual solitons because each soliton, which is contained in the bound soliton and initially has the same velocity, experiences a different transverse acceleration. A higher amplitude soliton experiences a larger transverse acceleration. The final result of the splitting process, i.e. a soliton either exits or still oscillates and collides with others inside the waveguide, depends on the initial amplitude  $\eta_0$ . When the nonparaxial effect is taken into account, the oscillation period of the single soliton becomes longer. Since the period extension of the soliton with the larger amplitude is much larger than the one with the smaller amplitude, the nonparaxiality will change the splitting process which may cause a very different result. In Figure 5.8 and 5.9 we present the simulation results of Equation (5.7) using initial data (5.23) for two different  $\eta_0$ 's and  $\kappa^2 = 0.001, 0.01$ . In these calculations, the Gaussian waveguide is characterized by  $\Delta n_0 = 0.1$  and  $b = 0.1$  while the initial position of the bound soliton is taken to be  $X_0 = -3.5$ . In the nonparaxial simulations, we observe that the field is radiating. However, the radiation is very small compared to the amplitude of the core parts. For simplicity, we call the core parts as two solitons with different amplitude (although one or none of them may be just a radiating entity).

In Figure 5.8, we show the numerical results for  $\eta_0 = 0.75$ . From the NLS simulation (see Figure 5.8.(a)), it is shown that the bound soliton is splitted into two individual

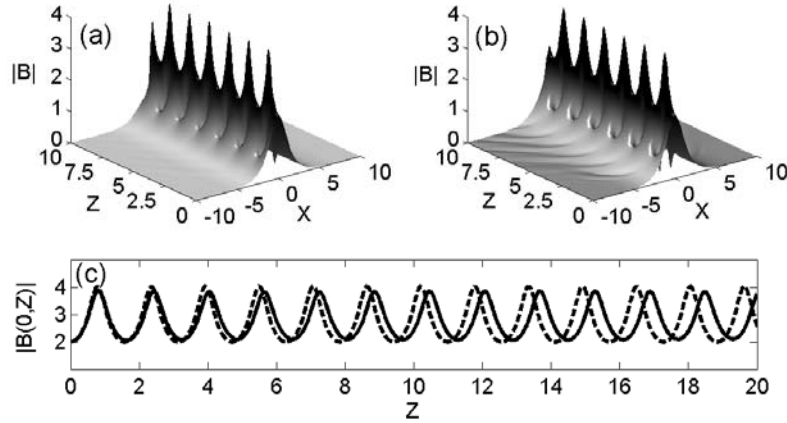


Figure 5.7: Propagation of a paraxial bound-2-soliton in uniform medium (a) using the NLS equation (denoted by  $\kappa^2 = 0$ ) and (b) using the NNLS equation with  $\kappa^2 = 0.01$ . Notice that the paraxial case describes the periodic breathing without any radiation while the nonparaxial approach accounts for the radiated field. In (c) we plot the on-axis amplitude obtained from the NLS equation (dashed) and the NNLS equation (solid). It is clearly seen that the nonparaxial propagation has a smaller peak amplitude and a longer period of the focusing-defocusing cycle compared to the paraxial case.

solitons after some propagation distance where the smaller soliton is expelled to the right of the waveguide while the higher one is oscillating inside the waveguide. The result of the nonparaxial model using  $\kappa^2 = 0.001$ , also shows a similar behavior: the smaller soliton also exits the waveguide after the splitting process, but it is slightly less displaced than the paraxial one with respect to the propagation axis. When we increase the degree of the nonparaxiality to a value  $\kappa^2 = 0.01$ , a very different behavior is observed. The smaller soliton is also oscillating instead of exiting from the waveguide. Since the oscillation period of these solitons are different, they show consecutive collisions during propagation.

Further essentially different behavior of paraxial and nonparaxial models can be observed when we take  $\eta_0 = 1$ , see Figure 5.9. As in the case of  $\eta = 0.75$ , the paraxial bound soliton breaks up into two solitons of different amplitudes. In this case, after break up, the smaller soliton also exits from the waveguide whereas the higher one oscillates inside the waveguide. When we implement the NNLS equation with  $\kappa^2 = 0.001$ , a different behavior is observed. The two solitons resulting from the break up remain oscillating in the waveguide and collide with each other. When the degree of the nonparaxiality is increased to  $\kappa^2 = 0.01$  the nonparaxial model produces another different phenomenon. Here, the higher amplitude soliton has a much bigger transversal acceleration such that the bound soliton "breaks up" before it swings. Af-

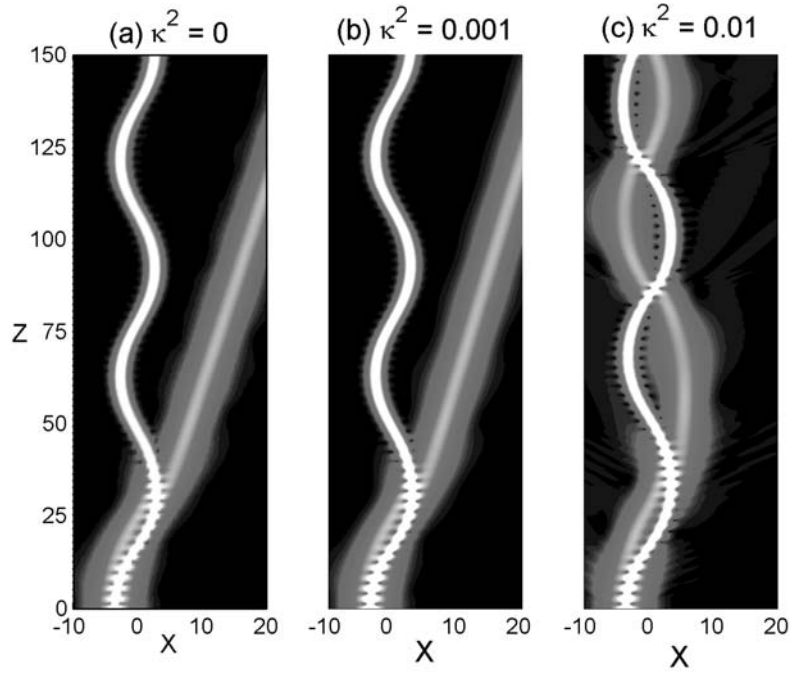


Figure 5.8: Break up of the paraxial bound-2-soliton with  $\eta_0 = 0.75$  in a Gaussian waveguide for  $\kappa^2 = 0, 0.001$  and  $0.01$ .

ter the break up, the two solitons show parallel oscillations but with different periods and trajectories which cause a consecutive collision.

In Figure 5.8 and 5.9, we also observe that in the regions where the beam envelope is changing rapidly, e.g. in the area of the splitting process or in the region of collisions, the beam is radiating. The bigger the amplitude ( $\eta_0$ ) and the degree of the nonparaxiality lead to larger radiations, see Figure 5.8.(c) and Figure 5.9.(c).

## 5.7 Deformation of bi-plane wave

As the last example, we consider the propagation of a modulated beam which is initially composed by two linear plane waves:

$$\begin{aligned} A(x, z) &= q_a \{ \exp(i(k_x x + k_z z - \pi/2)) + \exp(-i(k_x x - k_z z - \pi/2)) \} \\ &= \tilde{q} \sin(k_x x) \exp(ik_z z) \end{aligned} \quad (5.24)$$

where  $\tilde{q} = 2q_a$ , in uniform Kerr media. It was shown in chapter 3 that under the paraxial approximation a bi-plane wave can deform substantially, leading to large vari-

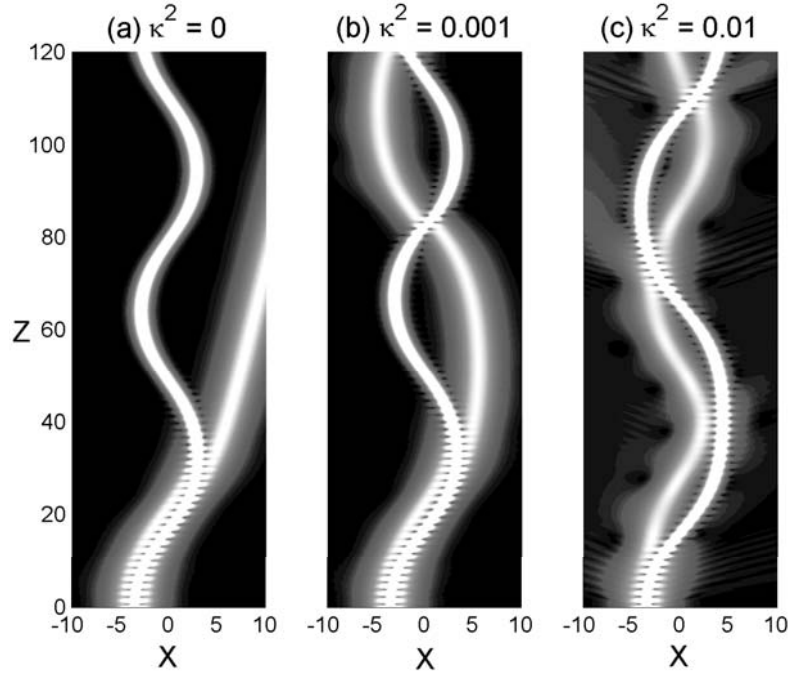


Figure 5.9: Same as for Figure 5.8, but for  $\eta_0 = 1$ .

ations in amplitude and phase. According to Equation(3.26) such variations appear when the following condition is satisfied

$$\frac{\tilde{q}}{k_x} > \sqrt{\frac{n_0}{2k_0^2 n_2}}. \quad (5.25)$$

Notice that we have translated the normalized amplitude  $q_b$  in Equation (3.26) into the physical amplitude  $\tilde{q}$  by defining that the width of the initial beam is the same as half of the modulation period ( $w_0 = \pi/k_x$ ):

$$q_b = (\tilde{q}/k_x) \sqrt{k_0^2 \pi^2 n_2 / n_0}. \quad (5.26)$$

In this section we will study the effect of the nonparaxiality on the deformation of an initially bi-plane wave numerically. To that end we solve the NNLS equation (5.7) using an implicit Crank-Nicolson scheme [2]. As the initial condition, we take a sinusoidal envelope

$$A(x, z = 0) = \tilde{q} \sin(k_x x). \quad (5.27)$$

In the normalized variables, the initial condition (5.27) becomes

$$B(X, Z = 0) = q_b \sin(\pi X). \quad (5.28)$$

Remark that  $q_b$  is proportional to the product of the physical amplitude and the modulation period. Using this initial condition, we perform numerical calculations



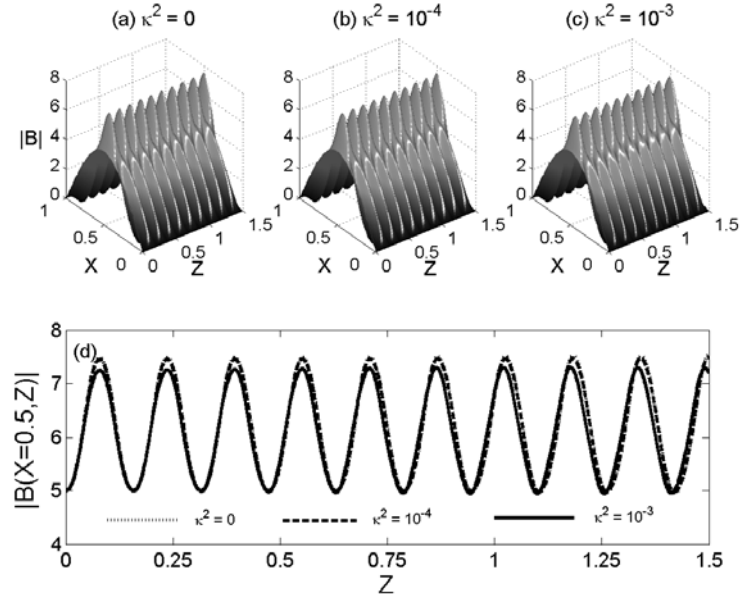


Figure 5.10: Deformation of bi-plane wave of amplitude  $q_b = 5$  obtained from (a) the NLS equation, (b) the NNLS equation with  $\kappa^2 = 10^{-4}$ , and the NNLS equation with  $\kappa^{-3}$ . In these plots we only show the half of the modulation period. Figure (d) depicts the the value of  $|B(X = 0.5, Z)|$ , showing the (quasi-) periodicity of the focusing-defocusing cycles. In the case of  $\kappa^2 = 10^{-4}$ , the NLS equation shows a very good agreement with the NNLS equation.

for various  $q_b$ 's and  $\kappa^2 \in \{10^{-4}, 10^{-3}\}$  with periodic boundary conditions in one modulation period  $X_{mod} = 2\pi/k_x$ . We found that the numerical solutions of the NLS equation agree reasonably well with those of the NNLS equation for  $q_b \lesssim 4$ . In these cases, the bi-plane waves experience small or moderate deformations during the evolution. If we increase the amplitude  $q_b$ , the difference between the solution of the paraxial and the nonparaxial models becomes larger.

In Figure 5.10 we plot the results of numerical calculations for  $q_b = 5$ . Similar to the propagation of a bound soliton in a uniform medium, the paraxial bi-plane wave shows a (quasi-) periodic focusing-defocusing. If nonparaxiality is introduced, the bi-plane wave also shows a series of focusing-defocusing cycle but with a smaller peak amplitude and with a shorter focusing-defocusing period. The larger  $\kappa^2$  leads to a smaller peak amplitude and a shorter period.

When we increase the amplitude to  $q_b = 8$ , we observe also here that the peak amplitude of the nonparaxial bi-plane wave due to self-focusing is smaller than that of the paraxial one; see Figure 5.11. In this case, the period of the focusing-defocusing cycle of the nonparaxial bi-plane wave for  $\kappa^2 = 10^{-4}$  is longer than the result of the

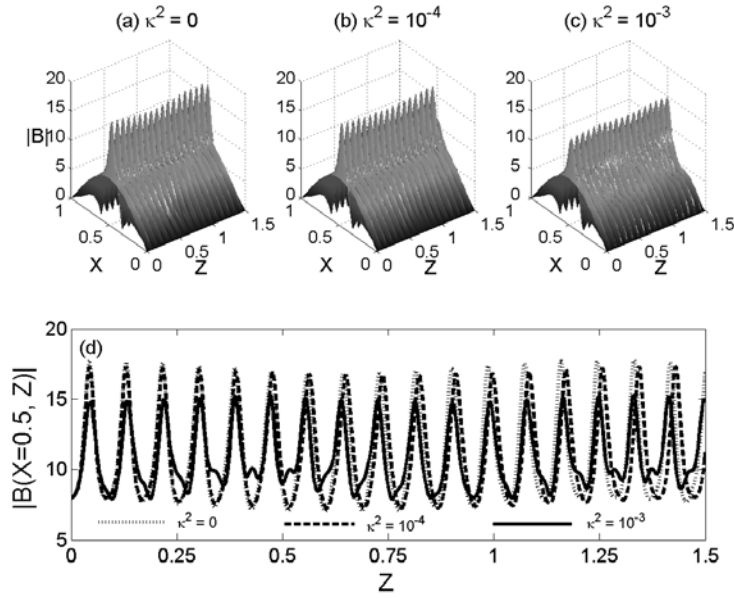


Figure 5.11: Same as for Figure 5.10, but for  $q_b = 8$ . The different behavior between the NLS and the NNLS equations is more pronounced in this case.

NLS equation. Furthermore, it is also found that the periodicity of the focusing-defocusing series is destroyed when we increase the degree of nonparaxiality to  $\kappa^2 = 10^{-3}$ .

## 5.8 Concluding remarks

In this chapter we have derived a unidirectional nonparaxial beam propagation in inhomogeneous Kerr media. By investigating the conservation laws and the fundamental soliton solutions of the NLH equation, of the NLS equation and of the NNLS equation, we show that the NLS and the NNLS equations are approximations of the NLH equation but that the NNLS model has a better accuracy.

Similar to the case of a paraxial soliton, it is found analytically and numerically that when a stationary nonparaxial soliton is placed in a Gaussian waveguide, it also oscillates inside the waveguide but with longer oscillation period compared to the period of the paraxial soliton with the same amplitude. The larger degree of nonparaxiality leads to a longer oscillation period. Based on this propagation property we study numerically the break up of a bound-N-soliton in a Gaussian waveguide. As mentioned in chapter 4 the break up of a paraxial bound-N-soliton depends very much on the oscillation period of each soliton contained in the bound-N-soliton. Because

the oscillation periods of these solitons are altered with the presence of nonparaxiality, the behavior of the bound-soliton break up produced by the NNLS equation may be very different with that resulted by the paraxial equation.

The NNLS equation has also been used to study the deformation of an initially linearly bi-plane wave. Our numerical calculations show that the NLS equation predicts reasonably well for the cases where the bi-plane waves experience small or moderate deformations during their evolutions. However, if the product of the amplitude and the modulation period is large enough such that large deformations exist, the nonparaxiality becomes a very sensitive parameter.

## References

- [1] N. Akhmediev, A. Ankiewicz and J.M. Soto-Crespo, Does the nonlinear Schroedinger equation correctly describe beam propagation?, *Opt. Lett.* **18**, p. 411, 1993.
- [2] Q.S. Chang, E.H. Jia and W. Sun, Difference schemes for solving the generalized nonlinear Schrödinger equation, *J. Comput. Phys.* **148**, p. 397, 1999.
- [3] E.L. Dawes and J.H. Marburger, Computer studies in self-focusing, *Phys. Rev.* **179**, p. 862, 1969.
- [4] M.D. Feit and J.A. Fleck, Beam nonparaxiality, filament formation, and beam breakup in the self-focusing of optical beams, *J. Opt. Soc. Am.* **B5**, p. 633, 1988.
- [5] G. Fibich, Small Beam Nonparaxiality Arrests Self-Focusing of Optical Beams, *Phys. Rev. Lett.* **76**, p. 4356, 1996.
- [6] G.R. Hadley, Transparent boundary-condition for beam propagation, *Opt. Lett.* **16**, p. 624, 1991.
- [7] M. Karlsson, Optical beams in saturable self-focusing media, *Phys. Rev.* **A46**, p. 2726, 1992.
- [8] P. L. Kelley, Self-focusing of optical beams, *Phys. Rev. Lett.* **15**, p. 1005, 1965.
- [9] Kh.I. Pushkarov, D.I. Pushkarov and I.V. Tomov, Self-action of light beams in nonlinear media: soliton solution, *Opt. Quant. Electr.*, **11**, p. 471, 1979.
- [10] A.P. Sheppard and M. Haelterman, Nonparaxiality stabilizes three-dimensional soliton beams in Kerr media, *Opt. Lett.* **23**, p. 1820, 1998.
- [11] J.M. Soto-Crespo and N. Akhmediev, Description of the self-focusing and collapse effects by a modified nonlinear Schrödinger equation, *Opt. Commun.* **101**, p. 223, 1993.

- [12] E. Yablonovitch and N. Bloembergen, Avalanche Ionization and the Limiting Diameter of Filaments Induced by Light Pulses in Transparent Media, *Phys. Rev. Lett.* **29**, p. 907, 1972.

## Chapter 6

# Conclusions and recommendations

We have presented a study on the propagation of optical waves in Kerr nonlinear media, with emphasis on the optical beam propagation beyond the slowly varying envelope approximation (SVEA). Below we conclude this thesis by extracting important findings from the previous chapters and mention some possibilities for directly related future research.

The propagation of a continuous-wave in one-dimensional (1D) nonlinear grating structures has been studied. For this purpose we have developed a numerical scheme based on a variational method. It directly implements the nonlinear Helmholtz (NLH) equation including the transparent-influx boundary conditions (TIBC) without introducing any approximation except the finite element discretization. This is different from the nonlinear transfer matrix formalisms that are based on the SVEA and other approximations. Therefore our method can also be used to study the validity of the nonlinear transfer matrix methods. To illustrate our method, we have studied the optical response of linear and nonlinear quarter-wavelength reflectors and shown that the method performs well, even for large nonlinear effects. The method was also found to be able to handle the optical bistable behavior of periodic structures with and without a defect layer as a function of either the frequency or the intensity of the input light. We have predicted that a relatively low threshold of bistability can be achieved in a defect structure by utilizing the large field enhancement and narrow resonance near frequency of the defect mode. By considering only the linear problem, the standard finite element method has been improved to get a fourth-order accurate scheme. However, this improvement is beneficial only for layer stacks with step-like refractive indices and for uniform grid. A further accuracy improvement that can be applied for more general structures as well as for nonlinear structures, e.g. by

implementing a Richardson's extrapolation as has been done by H.P. Uranus *et. al.*<sup>1</sup> for modal analysis of planar waveguides or using a higher order basis function is suggested for future research. An extension that takes off the theory of nonstationary problem is also highly valuable.

A numerical and analytical investigation of the deformation of bichromatic waves (or equivalently bi-plane waves in a spatial domain) has also been presented. Within the paraxial approximation, it was shown that an optical pulse that is initially linear bichromatic may deform substantially, resulting in large variations in amplitude and phase. Such deformations may lead to a train of soliton-like waves. The appearance of strong deformation of bichromatic pulses has been shown to depend on exceeding a critical value of the quotient of the amplitude and the frequency difference (which is also proportional to the product of the amplitude and the modulation period). This behavior holds equally well for the spatial analog. The deformation of bichromatic waves is similar to the phenomenon of modulation instability (MI) which is also described by the nonlinear Schrödinger (NLS) (or the paraxial) equation. An investigation of the relation between the deformation of a bichromatic wave and the MI is an interesting topic for future research.

Using the SVEA, we have derived a two-dimensional beam propagation model that includes a transverse linear refractive index variation. Based on this model we have found that a stationary spatial soliton placed in a triangular waveguide will always oscillate inside the waveguide. As was shown, if a bound-N-soliton, which consists of N solitons of different amplitudes but with the same velocity, is excited in a triangular waveguide, it will break up into N individual solitons. After break up, the splitting soliton may exit from the waveguide or at least have a perturbed oscillation path. The break up of a bound-N-soliton was more or less expected based on the theory of a single soliton in a triangular waveguide and also on the theory of bound-N-solitons in a uniform medium. A further analytical investigation, by considering a bound-N-soliton as a set of N interacting particles in a composite potential or by using the inverse scattering technique, is suggested.

The aforementioned study on the bi-plane wave distortion and the propagation of spatial solitons was based on the SVEA. To study nonparaxial effects related to these phenomena, we have derived a nonparaxial beam propagation model which is called the nonparaxial nonlinear Schrödinger (NNLS) equation. The accuracy of this model exceeds the standard SVEA. From several numerical experiments, we found that in the cases where the degree of nonparaxiality ( $\kappa$ ) is small, the paraxial equation is in good agreement with the nonparaxial model, as expected. However, in cases where rapid changes of the envelope occur, e.g. in the break up of a bound-N-soliton or in the propagation of bi-plane waves where the product of the amplitude and the modulation period is relatively big, the paraxial model may not describe the correct physical

---

<sup>1</sup>H.P. Uranus, H.J.W.M. Hoekstra, and E. van Groesen, Simple high-order Galerkin finite element scheme for the investigations of both guided and leaky modes in anisotropic planar waveguides, *Opt. and Quant. Electr.*, submitted (2003)

phenomena, especially for relatively large degrees of nonparaxiality. Although the accuracy of the nonparaxial equation presented in this thesis is better than the standard SVEA, this equation still assumes a slowly varying envelope such that further nonparaxial terms of the order  $\kappa^4$  and higher order terms can be neglected. If the degree of nonparaxiality or the beam amplitude is very large, the neglected higher order terms may become very important. Furthermore, the NNLS equation also neglects all back-reflections that may occur during the evolution and may interfere with the formal propagating waves. In these cases, the NNLS equation may also not fully describe the physical phenomena. Therefore a further detailed investigation on the full NLH equation (analytically or numerically) is essential. In particular, implementation of 2D or 3D transparent-influx boundary conditions for numerical simulation tools are very interesting topics for further research.





# Samenvatting

Dit proefschrift houdt zich bezig met de voortplanting van optische golven in Kerr-type niet-lineaire media, waarbij de nadruk ligt op optische bundelpropagatie die verder gaat dan de langzaam variërende omhullende benadering (Slowly Varying Envelope Approximation, SVEA).

Het eerste onderwerp in dit proefschrift is de propagatie van een continue golf in een-dimensionale (1D) niet-lineaire traliestructuren. Voor dit doel ontwikkelen we een numeriek schema gebaseerd op een variationele methode. Dit schema implementeert de niet-lineaire Helmholtz (NLH) vergelijking en haar transparante-influx randvoorwaarden (TIBC) direct zonder enige benadering te introduceren behalve de eindige-elementen discretisatie. Dit is anders dan in niet-lineaire transfer-matrix formalismes die gebaseerd zijn op de SVEA en andere benaderingen. Daarom is onze methode ook geschikt om de validiteit van de niet-lineaire transfer-matrix methodes te bestuderen. Om onze methode te illustreren bestuderen we de optische respons van lineaire en niet-lineaire kwart-golflengte reflectoren en we laten zien dat de methode geen problemen heeft met grote niet-lineaire effecten. Het blijkt ook dat de methode in staat is om het optisch bistabiele gedrag van de ideale structuur en de structuur met een defect te beschrijven als functie van de frequentie of de intensiteit van het inkomende licht. Wij voorspellen dat een relatief lage drempelwaarde voor bistabiliteit kan worden bereikt in een defect-structuur die goede optische kwaliteiten heeft (grote veld-opslingering en een smalle resonantie) door de frequentie van het inkomende licht te selecteren in de buurt van de defect-mode.

Eveneens wordt een numeriek en analytisch onderzoek naar de vervorming van bichromatische golven (of bi-vlakke golven in het ruimtelijke domein) gepresenteerd. Wij laten zien dat, binnen de paraxiale benadering, een optische puls die aanvankelijk linear bichromatisch is aanmerkelijk kan vervormen, wat resulteert in grote variaties in amplitude en fase. Zo'n vervorming kan leiden tot een trein van soliton-achtige golven. Het blijkt dat de verschijning van sterke vervorming van een bichromatische puls optreedt als het quotient van de amplitude en het frequentieverschil, wat ook proportioneel is met het produkt van de amplitude en de modulatie-periode, voldoende groot is. Dit gedrag doet zich evenzeer voor in het ruimtelijk analoge geval.

Gebruik makend van de SVEA ontwikkelen we een bundelpropagatiemethode waarin een transversale lineaire brekingsindexvariatie wordt meegenomen. Gebaseerd op dit model laten we zien dat een stationair ruimtelijk soliton dat op de juiste wijze in een driehoekige golfgeleider wordt geplaatst altijd zal oscilleren in de golfgeleider. De periode van oscillatie hangt af van de amplitude van het soliton. Dit betekent dat wanneer een gebonden N-soliton (bound-N-soliton), dat uit N solitonen van verschillende amplitude maar gelijke snelheid bestaat, zich in een driehoekige golfgeleider bevindt, hij zal opbreken in N individuele solitonen. Na deze opbreking kan het splitsende soliton de golfgeleider verlaten, of op zijn minst zal zijn oscillatie-pad worden verstoord.

Het hiervoor beschreven onderzoek naar de vervorming van bi-vlakke golven en de propagatie van ruimtelijke solitonen is gebaseerd op de SVEA. Om de niet-paraxiale effecten op deze fenomenen te onderzoeken leiden we een niet-paraxiaal bundelpropagatiemodel af, dat de niet-paraxiale niet-lineaire Schrödingervergelijking (NNLS) wordt genoemd. De nauwkeurigheid van dit model gaat verder dan die van de standaard SVEA. Uit verscheidene numerieke experimenten trekken we de conclusie dat de paraxiale vergelijking in gevallen waarin de graad van niet-paraxialiteit ( $\kappa$ ) klein is goede overeenkomsten vertoont met het niet-paraxiale model, zoals verwacht. Echter, in gevallen waarin snelle veranderingen in de omhullende voorkomen, bijvoorbeeld in het opbreken van het gebonden N-soliton of in de propagatie van een bi-vlakke golf waarin het produkt van de amplitude en de modulatieperiode relatief groot is, is het mogelijk dat het paraxiale model niet de correcte fysische fenomenen beschrijft, vooral voor een relatief grote mate van niet-paraxialiteit.

# Ringkasan

Tesis ini memuat hasil-hasil penelitian tentang perambatan gelombang optik di media dengan Kerr nonlinieritas, dengan penekanan pada efek ke-takparaksial-an pada perambatan berkas optik.

Perambatan gelombang kontinyu pada struktur grating nonlinier satu dimensi merupakan topik pertama dalam tesis ini. Untuk itu dikembangkan metode numerik berdasarkan metode variasi. Metode ini secara langsung mengimplementasikan persamaan Helmholtz nonlinear (NLH) dan kondisi batas yang dapat memasukkan semua gelombang datang dan sekaligus transparan untuk semua gelombang pantul (TIBC), tanpa menggunakan pendekatan apapun kecuali diskretisasi elemen hingga. Metode ini berbeda dengan metode transfer matriks nonlinier yang berdasarkan pada aproksimasi paraksial dan pendekatan lainnya. Oleh karena itu, metode yang dikembangkan dalam tesis ini dapat dipakai untuk meneliti validitas metode aproksimasi tersebut. Untuk mengilustrasikan metode yang dirancang, metode tersebut diimplementasikan untuk mempelajari respon optik dari pemantul seperempat-panjang gelombang dengan atau tanpa cacat, baik linier maupun nonlinier. Hasil-hasil simulasi menunjukkan bahwa metode ini mampu bekerja dengan baik meskipun untuk kasus-kasus dengan efek nonlinieritas yang besar. Metode ini juga dapat menunjukkan perilaku kestabilan ganda optik dari struktur periodik yang sempurna ataupun struktur grating dengan satu lapisan cacat sebagai fungsi dari frekuensi atau intensitas dari cahaya yang datang. Diprediksikan bahwa ambang batas dari kestabilan ganda yang relatif rendah dapat direalisasikan pada struktur cacat yang optimal, yaitu dengan menseleksi frekuensi gelombang datang di sekitar frekuensi resonan dari struktur yang cacat.

Dalam tesis ini juga dibahas tentang deformasi gelombang bikromatik, baik secara analitik maupun numerik. Dalam lingkup aproksimasi paraksial yang berasumsi bahwa selubung gelombang berubah secara lambat (SVEA), ditunjukkan bahwa pulsa optik yang awalnya bikromatik dapat mengalami deformasi substansial, yang mengakibatkan perubahan-perubahan besar pada amplitudo dan fase. Perubahan-perubahan besar tersebut dapat menghasilkan suatu deretan dari gelombang seperti soliton. Ditunjukkan bahwa deformasi-deformasi yang kuat pada pulsa bikromatik terjadi jika perbandingan amplitudo dan beda frekuensi melewati batas kritis. Perbandingan amplitudo dan beda frekuensi tersebut sebanding dengan hasil kali amplitudo dan

periode modulasi. Fenomena ini berlaku tidak hanya pada pulsa bikromatik, tetapi juga pada berkas yang awalnya terbentuk dari dua gelombang bidang (bi-plane wave) yang linier.

Dengan menggunakan SVEA, dibuat model perambatan berkas optik yang memuat variasi indeks bias linier secara transversal. Berdasarkan model yang berbentuk persamaan Schrödinger nonlinier (NLS) ini, ditemukan bahwa berkas soliton stasioner yang ditempatkan pada pandu-gelombang segitiga akan berosilasi di dalam pandu-gelombang. Periode dari osilasi tersebut sangat tergantung pada amplitudo soliton. Dengan demikian, jika suatu berkas bound-N-soliton, yaitu berkas yang terdiri dari N soliton dengan amplitudo berbeda tetapi mempunyai kecepatan yang sama sehingga merambat secara bersama-sama, ditempatkan pada pandu-gelombang segitiga maka bound-N-soliton tersebut akan terdekomposisi menjadi N soliton bebas. Setelah proses pemisahan, soliton-soliton yang dihasilkan dapat keluar dari pandu-gelombang atau setidaknya jalur osilasinya terganggu.

Penelitian tentang deformasi bi-plane wave dan perambatan berkas soliton yang telah disebutkan di atas hanya berdasarkan pada SVEA. Untuk mempelajari pengaruh ke-takparaksial-an pada fenomena-fenomena tersebut, dikembangkan model untuk perambatan berkas yang takparaksial (NNLS). Model ini lebih akurat dibandingkan dengan model paraksial standar (persamaan NLS). Hasil-hasil perhitungan secara numerik menunjukkan bahwa persamaan NLS memberikan hasil yang sesuai dengan yang diperoleh dari persamaan NNLS untuk kasus-kasus yang tingkat ke-takparaksial-annya kecil. Tetapi dalam kasus-kasus di mana perubahan selubung gelombang secara cepat dapat terjadi, misalnya pada proses pemisahan bound-N-soliton atau pada perambatan berkas yang awalnya dua gelombang bidang di mana hasil kali amplitudo dan periode modulasinya relatif besar, model paraksial tidak sepenuhnya mampu menjelaskan fenomena fisika dengan benar.

# List of publications

1. D. Chandra, H.J.J. Gramberg, T. Ivashkova, W.R. Smith, **A. Suryanto**, et al., Modelling of moisture induced warp in panels containing wood fibres, *EUT Report 00-WSK-01*, p. 25 (2000), ISSN 0167-9708.
2. **A. Suryanto**, E. van Groesen and H.J.W.M. Hoekstra, Deformation of modulated wave groups in third order nonlinear media, *Optical and Quantum Electronics* **33**, p. 313 (2001), ISSN 0306-8919.
3. **A. Suryanto**, E. van Groesen and H.J.W.M. Hoekstra, A low-dimensional model for deformation of bichromatic waves in third order nonlinear media, abstract in *Proceedings of the third annual meeting of the COST action P2: Nonlinear Optics for the Information Society*, p. 147 (2001), ISBN 1-4020-0132-0.
4. **A. Suryanto** and E. van Groesen, On the swing effect of spatial inhomogeneous NLS solitons, *J. Nonlinear Optical Physics and Materials* **10**, p. 143 (2001), ISSN 0218-8635.
5. **A. Suryanto**, Oscillating and interacting optical solitons, *Technical Digest of the 37<sup>e</sup> Nederlands Mathematisch Congres*, (2001), Amsterdam, The Netherlands.
6. E. van Groesen, E. Cahyono and **A. Suryanto**, Uni-directional models for narrow and broad pulse propagation in second order nonlinear media, *Optical and Quantum Electronics* **34**, p. 577 (2002), ISSN 0306-8919.
7. **A. Suryanto** and E. van Groesen, Break up of bound-N-spatial-soliton in a ramp waveguide, *Optical and Quantum Electronics* **34**, p. 597 (2002), ISSN 0306-8919.
8. **A. Suryanto** (editor), *J. of Indonesian Mathematical Society (MIHMI)* **8(20)**, (2002), ISSN 0854-1380.

9. **A. Suryanto**, E. van Groesen, M. Hammer and H.J.W.M. Hoekstra, A finite element scheme to study the nonlinear optical response of a finite grating without and with defect, *Optical and Quantum Electronics* **35**, p. 313 (2003), ISSN 0306-8919.
10. **A. Suryanto**, E. van Groesen and M. Hammer, Finite element analysis of optical bistability in one-dimensional nonlinear photonic band gap structures with a defect, *J. Nonlinear Optical Physics and Materials*, accepted (2003), ISSN 0218-8635.
11. **A. Suryanto**, E. van Groesen, M. Hammer and H.J.W.M. Hoekstra, Nonparaxial effects on the propagation of (1+1)D spatial solitons in inhomogeneous Kerr media, in preparation.

# Curriculum vitae

Agus Suryanto was born in Malang, Indonesia, on August 7, 1969. After completed secondary school education at the Sekolah Menengah Atas Negeri 7 (SMAN 7) Malang in 1988, he studied at the Brawijaya University, Indonesia, from which he obtained his bachelor's degree in Mathematics in 1992. In the period January 1993 - March 1995, he worked at the Technology Center of PT Barata Indonesia in Surabaya. Started from December 1994, he is a staff member of the Department of Mathematics, Faculty of Mathematics and Natural Sciences, Brawijaya University. In August 1997 he started to study at the Department of Applied Mathematics, University of Twente, The Netherlands. After finishing his master's thesis on "Model for Reflection Properties of Hydrodynamic Beaches" which was executed at Maritime Research Institute Netherlands (MARIN) under supervision of Prof. E. van Groesen, he received his Master's degree in Engineering Mathematics from the University of Twente in June 1999. Afterwards, he started his PhD research in September 1999 at the Department of Applied Mathematics, Faculty of Electrical Engineering, Mathematics and Computer Science, University of Twente, supervised by his promotor Prof. E. van Groesen and co-promotor Dr. H.J.W.M. Hoekstra. The results of this research are presented in this thesis. After his PhD graduation he will return to the Department of Mathematics, Brawijaya University.